3-9-2009

The Effective Potential Energy Surfaces of the Nonadiabatic Collision $B(^2P_{ja}) + H_2(^1\Sigma^+_g,\nu,j) \leftrightarrow B(^2P_{j'a}) + H_2(^1\Sigma^+_g,\nu',j')$

Matthew B. Garvin

THE EFFECTIVE POTENTIAL ENERGY SURFACES OF THE NONADIABATIC COLLISION

$$B\left(^2P_{j_a}\right) + H_2\left(^1\Sigma_g^+, v, j\right) \leftrightarrow B\left(^2P_{j_a'}\right) + H_2\left(^1\Sigma_g^+, v', j'\right)$$

DISSERTATION

Matthew B. Garvin, Captain, USAF

AFIT/DS/ENP/09-J01

DEPARTMENT OF THE AIR FORCE
AIR UNIVERSITY

AIR FORCE INSTITUTE OF TECHNOLOGY

Wright-Patterson Air Force Base, Ohio

The views expressed in this dissertation are those of the author and do not reflect the official policy or position of the United States Air Force, Department of Defense, or the United States Government.

AFIT/DS/ENP/09-J01

THE EFFECTIVE POTENTIAL ENERGY SURFACES OF THE NONADIABATIC COLLISION

$$B\left(^2P_{j_a}\right) + H_2\left(^1\Sigma_g^+, v, j\right) \leftrightarrow B\left(^2P_{j'_a}\right) + H_2\left(^1\Sigma_g^+, v', j'\right)$$

DISSERTATION

Presented to the Faculty

Graduate School of Engineering and Management

Air Force Institute of Technology

Air University

Air Education and Training Command

In Partial Fulfillment of the Requirements for the

Degree of Doctor of Philosophy

Matthew B. Garvin, BS, MS

Captain, USAF

March 2009

APPROVED FOR PUBLIC RELEASE; DISTRIBUTION UNLIMITED

AFIT/DS/ENP/09-J01

THE EFFECTIVE POTENTIAL ENERGY SURFACES
OF THE NONADIABATIC COLLISION
$B\left(^2P_{j_a}\right) + H_2\left(^1\Sigma_g^+, v, j\right) \leftrightarrow B\left(^2P_{j'_a}\right) + H_2\left(^1\Sigma_g^+, v', j'\right)$

Matthew B. Garvin, BS, MS
Captain, USAF

Approved:

David E. Weeks (Chairman)	Date
William F. Bailey (Member)	Date
Aihua W. Wood (Member)	Date

Accepted:

M. U. Thomas Dean, Graduate School of Engineering and Management	Date

Abstract

Effective potential energy surfaces (PESs) are calculated for the nonadiabatic collision $B\left(^2P_{j_a}\right) + H_2\left(^1\Sigma_g^+, v, j\right) \leftrightarrow B\left(^2P_{j'_a}\right) + H_2\left(^1\Sigma_g^+, v', j'\right)$. This calculation employed 1 $^2A'$, 2 $^2A'$, and 1 $^2A''$ adiabatic PESs numerically calculated at the state-averaged multiconfigurational self-consistent field (SA-MCSCF)/configuration interaction (CI) level for several values of the H_2 bond length, H_2 orientation angle, and boron distance. The associated nonadiabatic coupling terms (NACTs) were calculated from the SA-MCSCF/CI wave functions using analytic gradient techniques. A line integral through the NACTs was then used to determine the adiabatic-to-diabatic mixing angle required to transform from the 1 $^2A'$ and 2 $^2A'$ adiabatic basis to a corresponding diabatic basis. When all nonadiabatic coupling terms between all electronic states are considered, the line integral is path independent. However, only NACTs between the 1 $^2A'$ and 2 $^2A'$ states were considered in these calculations, and the line integral was therefore path dependent. The path dependence of the line integral was used to characterize the error introduced by employing a truncated set of adiabatic states. A method for reducing the effect of this error through the use of symmetry derived boundary conditions was developed. The resulting diabatic PESs were combined with the total B + H_2 rotational kinetic energy and boron spin-orbit coupling to yield diabatic effective PESs. The diabatic effective PESs were diagonalized to yield adiabatic effective PESs. Diabatic effective PESs data was extracted for the equilibrium H_2 bond length and used to calculate inelastic scattering matrix elements using the time dependent

channel packet method. These matrix elements were compared previous results [D. E. Weeks *et al.*, J. Chem. Phys. **125**, 164301 (2006)] to observe the sensitivity of this calculation to the input electronic structure data.

To my family

Acknowledgements

Special thanks go to my faculty advisor Dr. David Weeks for his guidance throughout this entire effort. I am very grateful not only for the time he devoted each week to discussing the status of the work, but also his infectious love of learning that is communicated through his teaching. I also wish to thank Dr. William Bailey and Dr. Aihua Wood for their service on my committee.

Matthew B. Garvin

Table of Contents

List of Figures

Figure Page

Figure Page

Figure Page

Figure Page

List of Tables

THE EFFECTIVE POTENTIAL ENERGY SURFACES

OF THE NONADIABATIC COLLISION

$$B\left(^2P_{j_a}\right) + H_2\left(^1\Sigma_g^+, v, j\right) \leftrightarrow B\left(^2P_{j_a'}\right) + H_2\left(^1\Sigma_g^+, v', j'\right)$$

I. Introduction

Motivation

In 1926 Erwin Schrödinger published his landmark paper introducing the wave equation which would later bear his name.[1] Schrödinger's equation elegantly reproduced the results achieved by Neils Bohr and others for the hydrogen-like atom and was quickly applied to other atomic/molecular systems. However, progress on solving Schrödinger's equation for systems more complex than the hydrogen-like atom stalled. Like the many-body problem in classical mechanics the resulting equations for an atomic/molecular system could not be solved analytically.

One year after the Schrödinger equation was introduced, Born and Oppenheimer proposed that the dynamics of electrons could be treated separately from the dynamics of the nuclei in atoms and molecules.[2, 3] This approximation was motivated by the fact that electrons move much faster than the more massive nuclei. This approach to solving the Schrödinger equation is known as the Born-Oppenheimer approximation (BOA).

Despite the utility of the BOA, in 1929, Dirac summarized the difficulties encountered early on when solving the Schrödinger equation for atomic and molecular

systems stating the following: "*The underlying physical laws necessary for the mathematical theory of a large part of physics and the whole of chemistry are thus completely known, and the difficulty lies only in the fact that the exact application of these laws leads to equations much too complicated to be soluble*." However, since the advent of computers, the BOA has become a standard tool for numerically solving the Schrödinger equation for atomic and molecular systems.

In the BOA the positions of the nuclei are fixed by setting their kinetic energy operators to zero in the Hamiltonian. The electron kinetic energy operators are retained. The resulting electronic Schrödinger equation is solved numerically yielding a complete Hilbert space of electronic eigenfunctions, and corresponding electronic energy eigenvalues. The positions of the nuclei are then changed and a new electronic problem is solved. This process is repeated for a variety of nuclear configurations using nuclear coordinates as parameters in the electronic Hamiltonian. The resulting collection of ground state electronic energy eigenvalues as a function of nuclear coordinates is called the ground state potential energy surface (PES). The numerical approaches to solving for these energies and wave functions include Hartree-Fock self-consistent field (HFSCF), configuration interaction (CI), and multiconfigurational self-consistent field methods. In general all of these techniques are referred to as *ab initio* methods.

After the electronic PESs and wave functions are calculated, the nuclear kinetic energy operators are re-introduced to the Hamiltonian. The resulting nuclear/electronic Schrödinger equation is solved by first expanding the complete nuclear/electronic wave functions in terms of the electronic wave functions. The coefficients of this expansion are solved by representing the nuclear/electronic Schrödinger equation in the electronic

basis. This is called the adiabatic representation. In this representation the Schrödinger equation has terms which couple electronic eigenstates. The coupling terms are referred to as nonadiabatic coupling terms (NACTs). The BOA ignores the NACTs creating a set of uncoupled equations equal to the number of electronic wave functions used to expand the nuclear/electronic wave functions.[4] Under these conditions the nuclear dynamics for a given electronic eigenstate are influenced by a single PES and the system is said to behave adiabatically.

The BOA ignores the NACTs whether they are significant or not.[4] The NACTs can be large when the electronic eigenstates have a strong dependence on nuclear coordinates. When these terms are significant the adiabatic representation produces a set of coupled equations. Under these conditions the nuclear dynamics for a given electronic eigenstate depend on multiple PESs and the system is said to behave nonadiabatically.

Nonadiabatic systems are common, especially for polyatomic systems.[5] Over the past several decades, a great deal of research has been done to understand nonadiabatic systems.[6] Nonadiabatic effects play an important role in the radiationless relaxation of excited electronic states and the photodissociation of molecules.[7] These effects are recognized to play a critical role photobiochemical processed such as in photosynthesis in plants, vision, and the photochemistry of DNA.[4] The ability to accurately model nonadiabatic molecular dynamics is applicable to many areas of active Air Force research. These areas include the modeling of collisional transitions between atoms and molecules in diode-pumped alkali lasers (DPALs)[8-10], and the modeling high energy density materials (HEDM) for explosives and fuel.[11]

Statement of Objectives

Progress in modeling nonadiabatic systems has been slow due to the computational requirements they impose. Using quantum mechanical formulations [12-18], current state-of-the-art calculations can only treat the nonadiabatic dynamics of systems with three to four atoms. Beyond this, classical and semi-classical approximations[19-25] are employed to achieve results.

This research uses a quantum mechanical treatment to explore the nonadiabatic effects encountered during the inelastic collision between a boron atom and a hydrogen molecule. The equation for this scattering event is given by

$$B\left(^2P_{j_a}\right) + H_2\left(^1\Sigma_g^+, v, j\right) \leftrightarrow B\left(^2P_{j'_a}\right) + H_2\left(^1\Sigma_g^+, v', j'\right) \qquad (1)$$

In this interaction the boron starts in a ^2P electronic state and is free to transition to a different ^2P state. The hydrogen molecule is restricted to its ground electronic state; however, it is free to make rotational and vibrational transitions.

The interaction of atomic boron and molecular hydrogen has been the subject of many studies.[11, 26-38] As stated in Weeks (2006)[37], general interest in the interaction of atomic boron with molecular hydrogen stems in part from the high degree of collisional quenching that is observed when excited metal atoms, including boron, react with molecular hydrogen.[39] Collisional studies of excited B($4p\ ^2P$) with H_2 and D_2 have also identified a significant isotope effect on reaction rates and indicate that nonadiabatic mechanisms may influence the experimentally observed distribution of molecular products.[32, 33] Additional interest in the B+H_2 system is derived from the B+H_2 van der Waals complex observed in molecular beam experiments[28, 34, 35] and in boron doped matrices of frozen H_2.[11, 31] Recent interest in the B + H_2 system stems from efforts to

model the nonadiabatic molecular dynamics of the inelastic collision $B\left(^2P_{1/2}\right) + H_2\left(^1\Sigma_g^+, j\right) \leftrightarrow B\left(^2P_{3/2}\right) + H_2\left(^1\Sigma_g^+, j'\right)$ which this work most directly extends.[36, 37] The ^2P manifold of the B + H_2 system also serves as a proxy for the excited states of DPALs.

The research presented in this dissertation has five main aims. First, all of the theory required to treat the interaction given by Eq. (1) is presented. In this section the theory behind the BOA is presented and applied to the B + H_2 system. The method for solving the Schrödinger equation when the BOA breaks down is presented. The specific case of an atom with a single valence electron in a *p* orbital interacting with a homonuclear diatomic molecule is treated. This leads to the method for calculating effective potential energy surfaces for the B + H_2 system. Finally the scattering theory required for the calculation of scattering matrix elements using the Channel Packet Method (CPM)[40-44] is presented.

Second, *ab initio* calculations of the three adiabatic PESs corresponding to the boron ^2P electronic states and associated NACTs are presented. The adiabatic PESs for this work were calculated at the state-averaged multiconfigurational self-consistent field (SA-MCSCF)/configuration interaction (CI) level by Dr. David Yarkony at Johns Hopkins University.[29, 45, 46] The NACTs were calculated from the SA-MCSCF/CI wave functions using analytic gradient techniques.[29, 47] Adiabatic PESs and NACTs were calculated on a three dimensional grid which included several values of the molecular hydrogen bond length. Previous *ab initio* calculations of the adiabatic PESs for the B + H_2 system fixed the molecular hydrogen bond length at the equilibrium value of 1.402 a.u. [26, 27, 36, 37] This restriction forces the hydrogen molecule to remain in its ground vibrational state. The data presented in this dissertation are a prerequisite for future work

in which vibrational transitions of the hydrogen molecule are included in the calculation. Furthermore, previous work did not directly calculate the NACTs.[26, 27] The nonadiabatic effects were modeled using other methods. In the past the direct calculation of NACTs was avoided primarily because NACTs can become singular for some systems. These singularities make it very difficult to solve the Schrödinger equation numerically.[48] However, methods which use the NACTs are able to make an estimate of overall accuracy of the results that other methods cannot make.[48]

Third, the adiabatic representation is transformed via a unitary transformation to form the diabatic representation. When this transformation is chosen properly the NACTs are negligible in the diabatic representation, eliminating any singularities in the NACTs. The form of the Schrödinger equation is also greatly simplified in the diabatic representation. This work employs a line integral through the vector field defined by the NACTs to arrive at the adiabatic-to-diabatic mixing angle used in the unitary transformation.[49, 50] The symmetry of the $B + H_2$ system allows the value of this mixing angle to be predicted for certain configurations.[26, 27] This allows the accuracy of the diabatic PESs to be estimated. This work also presents a new method for reducing the source of error introduced by restricting the electronic basis to include only the boron ^2P electronic states.

Fourth, the diabatic PESs are cast into a form best suited for wave packet propagation. This is done by fitting the diabatic PESs to reduced Wigner rotational matrix elements and employing an interpolation scheme to yield fit coefficients at any desired nuclear coordinate.[26, 37] The fit coefficients are used to construct effective PESs

which include the effects of spin-orbit coupling and rotational dynamics. This work presents both diabatic and adiabatic forms of these effective PESs.

Finally, the data corresponding to the equilibrium bond length of the hydrogen molecule is extracted from these effective PESs and the CPM is used to compute scattering matrix elements. These scattering matrix elements are compared with previous one dimensional scattering results.[26, 27, 37]

II. Theory

The Hamiltonian

In the framework of quantum mechanics, the Hamiltonian operator is used to determine the time-evolution of the state of a system as part of the time-dependent Schrödinger equation (TDSE). The general form of the TDSE is given by

$$i\hbar \frac{\partial |\Psi\rangle}{\partial t} = \hat{H}|\Psi\rangle \qquad (2)$$

where $|\Psi\rangle$ is a wave function. While the wave function $|\Psi\rangle$ can be chosen arbitrarily it is often chosen as a superposition of eigenstates of the Hamiltonian determined by the time-independent Schrödinger equation (TISE). The general form of the TISE is given by

$$\hat{H}|\Phi\rangle = E|\Phi\rangle \qquad (3)$$

where $|\Phi\rangle$ is an eigenstate of the Hamiltonian operator $\hat{H}$. E is the energy eigenvalue associated with the eigenstate $|\Phi\rangle$. The set of all eigenstates of the Hamiltonian form a complete set of orthogonal states which can be used to express other states.

The Hamiltonian of a system of interacting atomic nuclei and electrons is given by

$$\hat{H} = \hat{T}_N + \hat{T}_e + \hat{V}_{NN} + \hat{V}_{eN} + \hat{V}_{ee} \qquad (4)$$

The operator $\hat{T}_N$ is the sum of all the kinetic energy operators for the nuclei.

$$\hat{T}_N = \sum_{\alpha=1}^{n_n} \frac{\hat{p}_\alpha^2}{2m_\alpha} \qquad (5)$$

In Eq. (5) the sum is carried out over the index α up to n_n, the total number of nuclei in the system. The mass of each nuclei is given by m_α. The momentum operator for each nuclei is given by $\hat{p}_\alpha$.

The second operator in Eq. (4), $\hat{T}_e$, is the sum of all the kinetic energy operators for the electrons.

$$\hat{T}_e = \sum_{i=1}^{n_e} \frac{\hat{p}_i^2}{2m_e} \qquad (6)$$

In Eq. (6) the sum is carried out over the index *i* up to the number of electrons in the system given by n_e. The mass of each electron is the same and is given by m_e. Like the nuclei, each electron has its own momentum operator which is given by $\hat{p}_i$.

The third operator in Eq. (4), $\hat{V}_{NN}$, is the sum of the Coulomb potential interaction operators between nuclei.

$$\hat{V}_{NN} = \sum_{\alpha=1}^{n_n} \sum_{\beta>\alpha}^{n_n} \frac{Z_\alpha Z_\beta e^2}{|\hat{\boldsymbol{q}}_\alpha - \hat{\boldsymbol{q}}_\beta|} \qquad (7)$$

In Eq. (7) the sum is over all unique parings of nuclei in the system. The charge of an electron is *e* and the charge numbers of each nuclei are given by Z_α and Z_β. The position operators of each nuclei are given by $\hat{\boldsymbol{q}}_\alpha$ and $\hat{\boldsymbol{q}}_{\boldsymbol{\beta}}$. The operator $\hat{\boldsymbol{q}}$ represents the set of position operators $\{\hat{q}_1, \hat{q}_2, \ldots\}$, one for each coordinate used.

The fourth operator in Eq. (4), $\hat{V}_{eN}$, is the sum of the Coulomb potential interaction operators between nuclei and electrons.

$$\hat{V}_{eN} = \sum_{i=1}^{n_e} \sum_{\alpha=1}^{n_n} \frac{Z_\alpha e^2}{|\hat{\boldsymbol{q}}_i - \hat{\boldsymbol{q}}_\alpha|} \qquad (8)$$

In Eq. (8) the sum is carried out over each nuclei and electron pair, where α is used to index nuclei and *i* is used to index electrons.

The last operator in Eq. (4), $\hat{V}_{ee}$, is the sum of the Coulomb potential interaction operators between electrons.

$$\hat{V}_{ee} = \sum_{i=1}^{n_e} \sum_{j>i}^{n_e} \frac{Z_j e^2}{|\hat{\boldsymbol{q}}_i - \hat{\boldsymbol{q}}_j|} \qquad (9)$$

In Eq. (9) the sum is carried out over all unique pairings of electrons in the system. The operators in Eqs. (5) through (9) are given in abstract form. The specific form of the operators will depend on the representation chosen. When these equations are combined, the Hamiltonian $\hat{H}$ for a system of n_n nuclei and n_e electrons can be written (in atomic units) as[51]

$$\hat{H} = \sum_{\alpha=1}^{n_n} \frac{\hat{p}_\alpha^2}{2m_\alpha} + \sum_{i=1}^{n_e} \frac{\hat{p}_i^2}{2} + \sum_{\alpha=1}^{n_n} \sum_{\beta>\alpha}^{n_n} \frac{Z_\alpha Z_\beta}{|\hat{\boldsymbol{q}}_\alpha - \hat{\boldsymbol{q}}_\beta|} + \sum_{i=1}^{n_e} \sum_{\alpha=1}^{n_n} \frac{Z_\alpha}{|\hat{\boldsymbol{q}}_i - \hat{\boldsymbol{q}}_\alpha|} + \sum_{i=1}^{n_e} \sum_{j>i}^{n_e} \frac{1}{|\hat{\boldsymbol{q}}_i - \hat{\boldsymbol{q}}_j|} \qquad (10)$$

In atomic units the mass and charge of an electron are $e = 1$ and $m_e = 1$. The Plank constant $\hbar$ is also unity in atomic units. The number of terms in Eq. (10) increases rapidly as electrons and nuclei are added to the system. The B + H_2 system has three nuclei and seven electrons. The Hamiltonian describing this system will have 55 terms. The TISE for the B + H_2 system cannot be solved analytically. Numerical methods for solving the TISE in this form for systems more complex than a single hydrogen atom are still being developed.[17]

The Born-Oppenheimer Approximation

In 1927, Born and Oppenheimer published their approach for solving the TISE for a molecule.[3] Their approach was motivated by comparing the relative masses of electrons and protons. Electrons, being roughly 1800 times less massive than a proton,

typically move much faster than the atomic nuclei. Thus, the electrons can be thought of as moving through the electric field produced by stationary nuclei. The nuclei, in turn, can then be thought of as moving through the average electric field produced by the quickly moving electrons. This observation motivated Born and Oppenheimer to treat the dynamics of the electrons separately from the nuclear dynamics.

Under the assumption that the nuclei are stationary, the nuclear kinetic energy operators are eliminated from Eq. (10) defining a new Hamiltonian:

$$\widehat{H}_{elec} = \sum_{i=1}^{n_e} \frac{\hat{p}_i^2}{2} + \sum_{\alpha=1}^{n_n} \sum_{\beta>\alpha}^{n_n} \frac{Z_\alpha Z_\beta}{|\boldsymbol{q}_\alpha - \boldsymbol{q}_\beta|} + \sum_{i=1}^{n_e} \sum_{\alpha=1}^{n_n} \frac{Z_\alpha}{|\widehat{\boldsymbol{q}}_i - \boldsymbol{q}_\alpha|} + \sum_{i=1}^{n_e} \sum_{j>i}^{n_e} \frac{1}{|\widehat{\boldsymbol{q}}_i - \widehat{\boldsymbol{q}}_j|} \qquad (11)$$

Eq. (11) is the electronic Hamiltonian. As in Eq. (10) α and β index nuclei while i and j index electrons. The nuclear positions are now parameters in $\widehat{H}_{elec}$ rather than operators. The symbol $\boldsymbol{q}$ represents the set of coordinates $\{q_1, q_2, \ldots\}$. The set of nuclear and electronic coordinates are represented by $\boldsymbol{q}_n$ and $\boldsymbol{q}_e$ respectively. The solutions to the electronic TISE have a parametric dependence on nuclear positions. The electronic TISE is given by

$$\widehat{H}_{elec}|j(\boldsymbol{q}_n)\rangle = E_{elec}^{j}(\boldsymbol{q}_n)\,|j(\boldsymbol{q}_n)\rangle \qquad (12)$$

where $|j(\boldsymbol{q}_n)\rangle$ refers to the j^{th} eigenstate of the electronic Hamiltonian with the nuclear positions for a given configurations of nuclei given by the set of nuclear coordinates q. The eigenstate $|j(\boldsymbol{q}_n)\rangle$ is expressed in the electronic coordinate representation as

$$\langle \boldsymbol{q}_e|j(\boldsymbol{q}_n)\rangle = \Phi_j(\boldsymbol{q}_n, \boldsymbol{q}_e) \qquad (13)$$

In Eq. (13) the dependence of $\Phi_j(\boldsymbol{q}_n, \boldsymbol{q}_e)$ on nuclear and electronic coordinates is shown explicity.

In Eq. (12) $E_{elec}^{j}(\boldsymbol{q}_{\mathrm{n}})$ refers to the j^{th} energy eigenvalue of the corresponding eigenstate. In the electronic Hamiltonian the nuclear repulsion term $\hat{V}_{NN}$ becomes a constant for a given nuclear configuration and is added to the energy eigenvalue $E_{elec}^{j}(\boldsymbol{q}_{\mathrm{n}})$ to yield the j^{th} PES. The PES for a given eigenstate is a function of nuclear coordinates. The dimensionality of the PES increases as the number nuclear degrees-of-freedom (DOF) increases.

For each nuclear configuration there are an infinite number of electronic eigenstates. These states form a set of orthonormal functions which is complete, as shown in Eq. (14).

$$\begin{aligned}\langle i(\boldsymbol{q}_{\mathrm{n}})|j(\boldsymbol{q}_{\mathrm{n}})\rangle &= \int d\boldsymbol{q}_e \langle i(\boldsymbol{q}_{\mathrm{n}})|\boldsymbol{q}_e\rangle\langle \boldsymbol{q}_e|j(\boldsymbol{q}_{\mathrm{n}})\rangle \\ &= \int d\boldsymbol{q}_e \Phi_i^*(\boldsymbol{q}_{\mathrm{n}},\boldsymbol{q}_e)\Phi_j(\boldsymbol{q}_{\mathrm{n}},\boldsymbol{q}_e) = \delta_{ij}\end{aligned} \qquad (14)$$

The eigenstates for different nuclear configurations are not orthogonal to one another in general.

Even after formulating the electronic Hamiltonian $\hat{H}_{elec}$, the corresponding electronic TISE must be calculated numerically using methods such as the Hartree-Fock (H-F) approximation, configuration interaction (CI), and multi-configuration self-consistent field (MCSCF) methods. These methods are referred to as *ab initio* techniques (Latin: from the beginning[52]). There are many software packages available that perform these calculations. Commonly used programs include GUASSIAN, GAMESS, MOLPRO, and COLUMBUS. These programs numerically solve the electronic TISE by creating wave functions for each electron (spatial orbitals) and combining them in linear combinations to form molecular orbitals. The linear combination of spatial orbitals is

optimized using variational methods.[51] The resulting wave functions are the eigenstates of $\hat{H}_{elec}$.

Using Eq. (11) the full nuclear and electronic TISE, Eq. (3), can be rewritten as

$$\hat{H}|\Psi\rangle = \left(\hat{T}_N + \hat{H}_{elec}\right)|\Psi\rangle = E|\Psi\rangle \qquad (15)$$

The set of all electronic eigenstates form a complete set and can be used as a basis to represent other functions. The solutions to the full TISE can be represented as

$$|\Psi(\boldsymbol{q}_\mathrm{n})\rangle = \sum_j F_j(\boldsymbol{q}_\mathrm{n})\,|j(\boldsymbol{q}_\mathrm{n})\rangle \qquad (16)$$

In Eq. (16) the full nuclear/electronic wave function is expanded using electronic eigenstates where $F_j(\boldsymbol{q}_\mathrm{n})$ is the expansion coefficient and is a function of nuclear coordinates. The coefficients $F_j(\boldsymbol{q}_\mathrm{n})$ can be solved by substituting Eq. (16) into Eq. (15), multiplying from the left by $\langle i(\boldsymbol{q}_\mathrm{n})|$, and integrating over electronic coordinates.

$$\langle i(\boldsymbol{q}_\mathrm{n})|\left(\hat{T}_N + \hat{H}_{elec} - E\right)\left\{\sum_j F_j(\boldsymbol{q}_\mathrm{n})\,|j(\boldsymbol{q}_\mathrm{n})\rangle\right\} = 0 \qquad (17)$$

This representation is called the adiabatic representation. When electronic eigenstates are used to represent the solutions of the full TISE they are referred to as adiabatic states and their corresponding PESs are called adiabatic PESs.

Since the total energy eigenvalue E is a constant, Eq. (17) can be further simplified by using the orthonormal property of the electronic eigenstates (Eq. (14)).

$$\langle i(\boldsymbol{q}_\mathrm{n})|(-E)\left\{\sum_j F_j(\boldsymbol{q}_\mathrm{n})\,|j(\boldsymbol{q}_\mathrm{n})\rangle\right\} = -E\sum_j F_j(\boldsymbol{q}_\mathrm{n})\delta_{ij} = -EF_i(\boldsymbol{q}_\mathrm{n}) \qquad (18)$$

The electronic Hamiltonian $\hat{H}_{elec}$ does not contain derivatives with respect to nuclear coordinates, thus it has no effect on $F_j(\boldsymbol{q}_\mathrm{n})$. This results in the term derived in Eq. (19).

$$\langle i(\boldsymbol{q}_\mathrm{n})|\left(\hat{H}_{elec}\right)\left\{\sum_j F_j(\boldsymbol{q}_\mathrm{n})\,|j(\boldsymbol{q}_\mathrm{n})\rangle\right\} = E^j_{elec}(\boldsymbol{q}_\mathrm{n})\sum_j F_j(\boldsymbol{q}_\mathrm{n})\delta_{ij} = E^i_{elec}(\boldsymbol{q}_\mathrm{n})F_i(\boldsymbol{q}_\mathrm{n}) \tag{19}$$

The operator $\hat{T}_N$ involves derivatives with respect to nuclear coordinates, and since both the coefficient $F_j(\boldsymbol{q}_\mathrm{n})$ and the eigenstate $|j(\boldsymbol{q}_\mathrm{n})\rangle$ depend on nuclear coordinates, the product rule must be used when evaluating this term. For clarity, the coordinate representation is used to express this inner product.

$$\begin{aligned}
&\langle i(\boldsymbol{q}_\mathrm{n})|\left(\hat{T}_N\right)\left\{\sum_j F_j(\boldsymbol{q}_\mathrm{n})\,|j(\boldsymbol{q}_\mathrm{n})\rangle\right\} = \sum_{j,\alpha}\left\langle i(\boldsymbol{q}_\mathrm{n})\left|-\frac{\nabla^2_{q_n}}{2m_\alpha}F_j(\boldsymbol{q}_\mathrm{n})\right|j(\boldsymbol{q}_\mathrm{n})\right\rangle \\
&= -\frac{1}{2}\sum_{j,\alpha}\frac{1}{m_\alpha}\int d\boldsymbol{q}_\mathrm{e}\Phi_i^{A*}(\boldsymbol{q}_\mathrm{n},\boldsymbol{q}_\mathrm{e})\nabla^2_{q_n}\left\{F_j(\boldsymbol{q}_\mathrm{n})\Phi_j^A(\boldsymbol{q}_\mathrm{n},\boldsymbol{q}_\mathrm{e})\right\} \\
&= -\frac{1}{2}\sum_{j,\alpha}\frac{1}{m_\alpha}\int d\boldsymbol{q}_\mathrm{e}\Phi_i^{A*}(\boldsymbol{q}_\mathrm{n},\boldsymbol{q}_\mathrm{e})\left\{F_j(\boldsymbol{q}_\mathrm{n})\nabla^2_{q_n}\Phi_j^A(\boldsymbol{q}_\mathrm{n},\boldsymbol{q}_\mathrm{e}) + 2\left(\vec{\nabla}_{q_n}F_j(\boldsymbol{q}_\mathrm{n})\right)\right. \\
&\left.\cdot\left(\vec{\nabla}_{q_n}\Phi_j^A(\boldsymbol{q}_\mathrm{n},\boldsymbol{q}_\mathrm{e})\right) + \Phi_j^A(\boldsymbol{q}_\mathrm{n},\boldsymbol{q}_\mathrm{e})\nabla^2_{q_n}F_j(\boldsymbol{q}_\mathrm{n})\right\}
\end{aligned} \tag{20}$$

The superscript A has been added to the coordinate representation of the eigenstates $\Phi_j^A(\boldsymbol{q}_\mathrm{n},\boldsymbol{q}_\mathrm{e})$ to clearly identify them as adiabatic states. The nuclear coordinate dependence of the del and Laplacian operators $\vec{\nabla}_{q_n}$ and $\nabla^2_{q_n}$ are indicated by the subscript q_n. The form of Eq. (20) can be simplified by defining the following terms:

$$\vec{\tau}^A_{ij} = \int d\boldsymbol{q}_\mathrm{e}\Phi_i^{A*}(\boldsymbol{q}_\mathrm{n},\boldsymbol{q}_\mathrm{e})\vec{\nabla}_{q_n}\Phi_j^A(\boldsymbol{q}_\mathrm{n},\boldsymbol{q}_\mathrm{e}) \tag{21}$$

$$\kappa^A_{ij} = \frac{1}{2}\int d\boldsymbol{q}_\mathrm{e}\Phi_i^{A*}(\boldsymbol{q}_\mathrm{n},\boldsymbol{q}_\mathrm{e})\nabla^2_{q_n}\Phi_j^A(\boldsymbol{q}_\mathrm{n},\boldsymbol{q}_\mathrm{e}) \tag{22}$$

The terms $\vec{\tau}_{ij}^{A}$ and κ_{ij}^{A} couple electronic eigenstates via their dependence on nuclear coordinates and are called derivative and kinetic coupling terms, respectively. They are referred to as nonadiabatic coupling terms (NACTs). The derivative coupling terms (DCTs) are vector quantities while the kinetic coupling terms are scalar values. The DCTs have a vector component for each nuclear coordinate used to describe the system. When referring to a specific component of the vector field defined by the DCTs the notation $\tau_{q,ij}^{A}$ is used, where q denotes the specific nuclear coordinate. In the literature the following shorthand notation for DCTs is frequently encountered:

$$\tau_{q,ij}^{A} = \left\langle \phi_i^A \middle| \frac{\partial}{\partial q} \phi_j^A \right\rangle \tag{23}$$

The DCTs are antihermitian as expressed in Eq. (24) (see Appendix A).

$$\vec{\tau}_{ij}^{A} = -\vec{\tau}_{ji}^{A*} \tag{24}$$

Combining the results of Eqs. (18) – (20) and using the definitions in Eqs. (21) and (22), Eq. (17) can be expressed as

$$-\frac{1}{2}\sum_{j,\alpha}\frac{1}{m_\alpha}\{\delta_{ij}\nabla_{q_n}^2 + 2\vec{\tau}_{ij}^{A}\cdot\vec{\nabla}_{q_n} + 2\kappa_{ij}^{A}\}F_j(\boldsymbol{q}_\mathrm{n}) + \left(E_{elec}^{i} - E\right)F_i(\boldsymbol{q}_\mathrm{n}) = 0 \tag{25}$$

Eq. (25) now represents the TISE in the adiabatic representation. Aside from treating the electronic problem separately from the complete nuclear/electronic problem, no other approximations have been made. However, expanding the TISE using Eq. (16) has created a system of coupled differential equations. When the NACTs are either small enough to be negligible or simply neglected the TISE becomes uncoupled and can be written as

$$\left(-\tfrac{1}{2}\textstyle\sum_\alpha \frac{\nabla_{q_n}^2}{m_\alpha} + E_{elec}^{i}(\boldsymbol{q}_\mathrm{n})\right)F_i(\boldsymbol{q}_\mathrm{n}) = EF_i(\boldsymbol{q}_\mathrm{n}) \tag{26}$$

This is referred to as the adiabatic Born-Oppenheimer approximation.[6] In Eq. (26) the expansion coefficient $F_i(\boldsymbol{q}_\mathrm{n})$ is interpreted as the nuclear wave function whose dynamics are governed by a single PES $E^i_{elec}(\boldsymbol{q}_\mathrm{n})$. The term $E^i_{elec}(\boldsymbol{q}_\mathrm{n})$ is called an adiabatic PES. In later calculations $V_i^A(\boldsymbol{q}_\mathrm{n}) = E^i_{elec}(\boldsymbol{q}_\mathrm{n})$ will be used as an alternate notation for the adiabatic PES associated with the i^{th} electronic eigenstate $|i(\boldsymbol{q}_\mathrm{n})\rangle$.

If a system is accurately modeled by Eq. (26) the system is said to behave adiabatically. However, not all systems can be modeled accurately by the adiabatic BOA. When the NACTs are too large to be neglected the adiabatic BOA is invalid. The generalized Hellmann-Feynman theorem, Eq. (27) , gives the clearest indication of when a system will behave nonadiabatically.

$$\vec{\tau}_{ij}^{A} = \frac{\langle i(\boldsymbol{q}_\mathrm{n})|\vec{\nabla}_{q_\mathrm{n}}\widehat{H}_{elec}|j(\boldsymbol{q}_\mathrm{n})\rangle}{V_j^A(\boldsymbol{q}_\mathrm{n}) - V_i^A(\boldsymbol{q}_\mathrm{n})} \qquad (27)$$

This theorem is derived in Appendix B. When $\langle i(\boldsymbol{q}_\mathrm{n})|\vec{\nabla}_{q_\mathrm{n}}\widehat{H}_{elec}|j(\boldsymbol{q}_\mathrm{n})\rangle$ is non-zero and the difference between $V_j^A(\boldsymbol{q}_\mathrm{n})$ and $V_i^A(\boldsymbol{q}_\mathrm{n})$ is small $\vec{\tau}_{ij}^{A}$ will be large. In the case where $V_j^A(\boldsymbol{q}_\mathrm{n}) = V_i^A(\boldsymbol{q}_\mathrm{n})$, the derivative coupling $\vec{\tau}_{ij}^{A}$ will be singular. Points where two PESs intersect and $\vec{\tau}_{ij}^{A}$ is singular are called conical intersections.[5] Systems that have conical intersections, like the B + H_2 system, cannot be modeled using Eq. (26).

The most common approach to solving Eq. (25) with non-negligible coupling terms involves transforming from the adiabatic basis to a new basis, the diabatic basis, in which the coupling terms are negligible.[49, 50] However, practical computational limitations restrict the number of electronic eigenstates that can be considered. To reduce the computational overhead, *ab initio* data is calculated only for a restricted subspace of the full electronic Hilbert space consisting of the electronic states most strongly coupled

to one another.[53] Restricting the subspace neglects any weak coupling between states within the subspace and external states and can limit the effectiveness of the adiabatic-to-diabatic transformation (ADT). [54-56] These considerations can be best illustrated by examining the B + H_2 system.

The B + H_2 System

In its ground state, boron has a $1s^2 2s^2 2p$ electronic state. The unpaired $2p$ electron gives rise to a ^2P spectroscopic term consisting of three degenerate atomic orbitals energetically separated from other boron orbitals. As the boron atom approaches the hydrogen molecule the degeneracy is lifted, however, they remain energetically close to one another. By Eq. (27) it is assumed that these orbitals will be strongly coupled to one another while only weakly coupled to states outside the ^2P manifold. Consequently, the electronic basis is truncated to include only the three states within the ^2P manifold.

In general, the B + H_2 system has $C_s = \{1, \sigma\}$ symmetry where 1 is the unit operator and σ corresponds to reflection though the B, H_2 plane. The symmetry of the orbitals is defined as follows:

$$\begin{aligned} A' &\Rightarrow \sigma|\Phi\rangle = 1|\Phi\rangle \\ A'' &\Rightarrow \sigma|\Phi\rangle = -1|\Phi\rangle \end{aligned} \qquad (28)$$

According to Eq. (28) orbitals that are unaffected by a reflection about the B, H_2 plane have A' C_S symmetry. Figure 1 shows an example of this type of orbital.

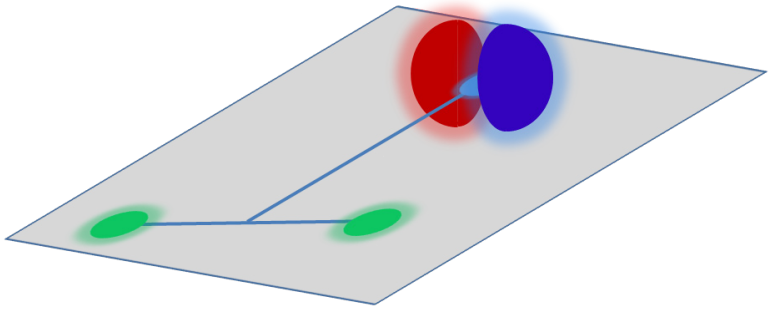

Figure 1. An example of a boron *p* orbital with A' C_S symmetry

In Figure 1, the green circles represent the hydrogen atoms, the blue circle represents the boron atom, the blue lobe represents the portion of the *p* orbital with positive phase, and the red lobe represents the portion of the *p* orbital with negative phase.

If a reflection about the B, H_2 plane flips the orientation of the orbital then the orbital has A'' C_S symmetry. An example of this type of orbital is shown in Figure 2.

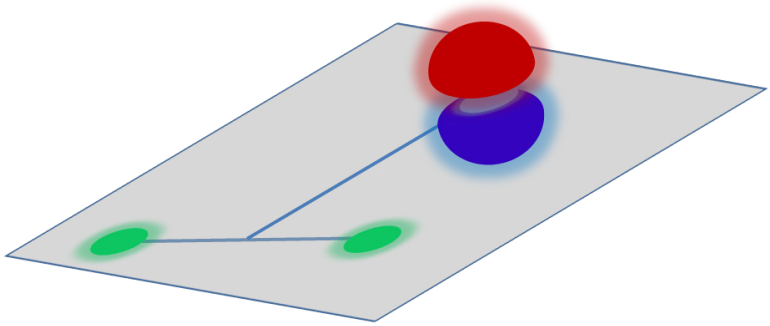

Figure 2. An example of a boron *p* orbital with A'' C_S symmetry

In Figure 2 a reflection about the B, H_2 plane would cause the lobes of positive and negative phase of a *p* orbital to change positions. The two boron 2*p* orbitals with A' C_S symmetry are labeled as $1\ ^2A'$ and $2\ ^2A'$ with $1\ ^2A''$ labeling the orbital with A'' C_S

symmetry. These orbitals have corresponding adiabatic PESs $V_{1\,^2A'}$, $V_{2\,^2A'}$, and $V_{A''}$. Here the superscript A has been omitted to avoid confusion with the symmetry label. Given that the B + H_2 involves a single atom interacting with a homonuclear diatomic molecule the adiabatic PESs satisfy the symmetry relation $V(r,\pi-\theta,R)=V(r,\theta,R)$.

The TISE, Eq. (25), for the B + H_2 system with a truncated electronic basis can be written as

$$\left\{\begin{pmatrix} -\frac{1}{2}\sum_\alpha \frac{\nabla^2_{q_n}}{m_\alpha} & 0 & 0 \\ 0 & -\frac{1}{2}\sum_\alpha \frac{\nabla^2_{q_n}}{m_\alpha} & 0 \\ 0 & 0 & -\frac{1}{2}\sum_\alpha \frac{\nabla^2_{q_n}}{m_\alpha} \end{pmatrix} + \begin{pmatrix} 0 & -\sum_\alpha \frac{1}{m_\alpha}\left[\vec{\tau}^A_{12}\cdot\vec{\nabla}_{q_n}+\kappa^A_{12}\right] & 0 \\ -\sum_\alpha \frac{1}{m_\alpha}\left[\vec{\tau}^A_{21}\cdot\vec{\nabla}_{q_n}+\kappa^A_{21}\right] & 0 & 0 \\ 0 & 0 & 0 \end{pmatrix} + \begin{pmatrix} V_{1^2A'} & 0 & 0 \\ 0 & V_{2^2A'} & 0 \\ 0 & 0 & V_{A''} \end{pmatrix}\right\}\begin{pmatrix} F_{1^2A'} \\ F_{2^2A'} \\ F_{A''} \end{pmatrix} = \begin{pmatrix} E & 0 & 0 \\ 0 & E & 0 \\ 0 & 0 & E \end{pmatrix}\begin{pmatrix} F_{1^2A'} \\ F_{2^2A'} \\ F_{A''} \end{pmatrix} \quad (29)$$

In Eq. (29) the NACTs have been separated from the kinetic energy operators and PESs. Orbitals with different C_S symmetry will not couple giving rise to the off-diagonal zeros in the NACT matrix. This is discussed in Appendix C. Although the eigenstate with A'' C_S symmetry does not couple with the other eigenstates it is still included in the calculation. All three functions span the boron 2p subspace and are required when transforming from a basis labeled by the angular momentum quantum numbers to one labeled by Cartesian coordinates. As a result of C_S symmetry, the matrix containing the coupling terms is block diagonal with a 2-by-2 block and a 1-by-1 block.

The coupling matrix can be simplified further by choosing real valued eigenstates. Given the antihermitian property of the DCTs, real valued functions forces the diagonal

coupling terms to be zero. This in turn forces the diagonal kinetic coupling terms to be zero due to the following relationship between derivative and kinetic coupling terms.

$$\begin{aligned} \vec{\nabla}_{q_n} \cdot \vec{\tau}_{ij}^{A} &= \kappa_{ij}^{A} - \vec{\tau}_{ij}^{A} \cdot \vec{\tau}_{ij}^{A} \\ \kappa_{ij}^{A} &= \vec{\nabla}_{q_n} \cdot \vec{\tau}_{ij}^{A} + \vec{\tau}_{ij}^{A} \cdot \vec{\tau}_{ij}^{A} \end{aligned} \qquad (30)$$

According to Eq. (30), if the derivative coupling term for a given pair of eigenstates is exactly equal to zero everywhere the corresponding kinetic coupling term will also be equal to zero.

The B + H_2 Coordinate System

The PESs as well as the NACTs depend on the nuclear coordinates used to describe the system. The internal DOF of the B + H_2 system are described by Jacobi coordinates *R*, the distance between the boron atom and the center-of-mass (CM) of the hydrogen molecule; *r*, the bond length of the hydrogen molecule; and θ, the polar angle formed by the axis containing the boron atom and the axis containing the hydrogen molecule which intersect at the CM of the hydrogen molecule. Figure 3 illustrates the same body fixed (BF) and space fixed (SF) coordinate system used by Weeks et al.[37] A body fixed (BF) coordinate system is chosen in which the boron atom and the H_2 CM are fixed on the BF *z* axis. The orientation of the hydrogen molecule is determined by the angle θ and the projection of the H_2 molecular axis on the BF *xy* plane. The azimuthal angle ϕ is formed between the BF *x* axis and this projection. This angle is not shown in Figure 3.

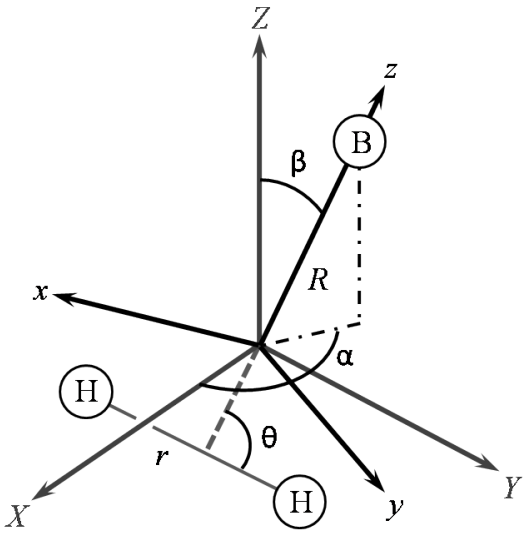

Figure 3. Body fixed and space fixed coordinate system used to describe the B + H_2 system[37]

The BF axis is oriented in the SF coordinate axes by using Euler angles α and β and constraining the BF y axis to lie in the SF XY plane. The Euler angle α is formed by the projection of the BF z axis onto the SF XY plane and the SF X axis. The Euler angle β is the polar angle formed between the BF z axis and the SF Z axis. The origin of both the BF and SF axes coincide at the B, H_2 CM. In Figure 3 the CM is displaced away from the boron atom for clarity. In this coordinate system the $1\,^2A'$ and $2\,^2A'$ orbitals are chosen to correspond to the p_z and p_x orbital of the boron atom respectively, while the A'' orbital corresponds to the p_y.[26, 37]

The Adiabatic-to-Diabatic Transformation

The TISE for the B + H_2 system in the adiabatic representation is given by Eq. (29). The NACTs make it difficult to solve Eq. (29) directly. As mentioned earlier, it is desirable to transform from the adiabatic representation to the diabatic representation in

which the NACTs are negligible. Many methods for calculating diabatic states have been described in the literature.[57] These methods can be divided into two groups: those that calculate the adiabatic-to-diabatic transformation (ADT) using the NACTs, and those that determine the diabatic states using the matrix elements of various Hermitian operators.[58] The methods in the latter group avoid the computational overhead of calculating the NACTs over a grid in nuclear configuration space dense enough to capture the strong variation NACTs can experience as a function of nuclear coordinates.[59-63] This variation is especially severe near conical intersections, where the DCTs become singular.[5] However, it is generally accepted that methods using NACTs are more accurate in calculating diabatic states.[48, 54]

With the truncated B + H_2 basis used in Eq. (29) the ADT is defined as

$$\begin{pmatrix} \Phi_{zz} \\ \Phi_{xx} \\ \Phi_{yy} \end{pmatrix} = \begin{pmatrix} \cos\gamma(\boldsymbol{q}_n) & -\sin\gamma(\boldsymbol{q}_n) & 0 \\ \sin\gamma(\boldsymbol{q}_n) & \cos\gamma(\boldsymbol{q}_n) & 0 \\ 0 & 0 & 1 \end{pmatrix} \begin{pmatrix} \Phi_{1^2A'} \\ \Phi_{2^2A'} \\ \Phi_{A''} \end{pmatrix} \qquad (31)$$

where the angle $\gamma(\boldsymbol{q}_n)$ is the ADT mixing angle.[57] The adiabatic states are labeled according to their symmetry. The diabatic states are given the labels *xx*, *yy*, and *zz*. In matrix form Eq. (31) is given by $\boldsymbol{\Phi}^{\mathrm{D}} = \mathbb{U}^{\dagger}\boldsymbol{\Phi}^{\mathrm{A}}$. The matrix $\mathbb{U}$ represents the diabatic-to-adiabatic transformation. The ADT transformation is unitary, thus $\mathbb{U}^{\dagger}\mathbb{U} = \mathbf{1}$. As discussed in Appendix C, only states with A' C_S symmetry will mix; hence, the transformation matrix $\mathbb{U}^{\dagger}$ has the same block diagonal form as the coupling matrix in Eq. (29). The ADT mixing angle $\gamma(\boldsymbol{q}_n)$ is calculated for each nuclear configuration.

The derivative coupling term between 1 $^2A'$ and 2 $^2A'$ states in the adiabatic representation can be transformed into the diabatic representation by using Eq. (31) to make the following substitutions into Eq. (21).

$$\Phi_{1^2A'}(\boldsymbol{q}_n, \boldsymbol{q}_e) = \Phi_{zz}(\boldsymbol{q}_n, \boldsymbol{q}_e)\cos\gamma(\boldsymbol{q}_n) + \Phi_{xx}(\boldsymbol{q}_n, \boldsymbol{q}_e)\sin\gamma(\boldsymbol{q}_n)$$
$$\Phi_{2^2A'}(\boldsymbol{q}_n, \boldsymbol{q}_e) = \Phi_{zz}(\boldsymbol{q}_n, \boldsymbol{q}_e)\sin\gamma(\boldsymbol{q}_n) + \Phi_{xx}(\boldsymbol{q}_n, \boldsymbol{q}_e)\cos\gamma(\boldsymbol{q}_n) \quad (32)$$

After simplifying the resulting expression Eq. (33) is obtained. The details of this derivation are given in Appendix D.

$$\vec{\tau}_{12}^{D} = \vec{\nabla}_{q_n}\gamma(\boldsymbol{q}_n) + \vec{\tau}_{12}^{A} \quad (33)$$

Under the assumption that the DCTs in the diabatic representation are equal to zero Eq. (33) simplifies to

$$\vec{\nabla}_{q_n}\gamma(\boldsymbol{q}_n) = -\vec{\tau}_{12}^{A} \quad (34)$$

For systems with a single nuclear coordinate this equation can be integrated directly to yield the ADT mixing angle. For systems with more than one nuclear coordinate the single integral becomes a path integral through the vector field defined by each component of the DCTs.[50, 64-66] For the case of B + H_2 the integral takes the following form:

$$\gamma(R,\theta,r) = \int_{R_0}^{R} \tau_{R,12}^{A}\big|_{r_0\theta_0} dR + \int_{\theta_0}^{\theta} \tau_{\theta,12}^{A}\big|_{Rr_0} d\theta + \int_{r_0}^{r} \tau_{r,12}^{A}\big|_{R\theta} dr + \gamma_0 \quad (35)$$

Eq. (35) assumes a specific order of integration for the Jacobi coordinates. Eq. (35) gives the ADT mixing angle γ to an overall constant γ_0. A reference point (r_0, θ_0, R_0) in the Jacobi coordinate space is chosen to start the line integral for all determinations of the ADT mixing angle. The ADT mixing angle for this reference point is set to zero or some arbitrary constant.

Under the assumption that $\vec{\tau}_{12}^{D} = 0$ the value of the mixing angle should be path independent as indicated by Eq. (36).

$$\vec{\nabla}_{q_n} \times \vec{\tau}_{12}^{A} = 0 \quad (36)$$

Eq. (36) follows directly from the vector calculus theorem that states that the curl of the divergence of a vector field must be zero: $\vec{\nabla}_{q_n} \times \left(\vec{\nabla}_{q_n} \gamma(\boldsymbol{q}_n)\right) = 0$. When this condition is met the ADT completely eliminates the NACTs and the resulting diabatic surfaces are called strictly diabatic surfaces.[48, 64, 67]

Under the assumption that the ADT successfully eliminates the NACTs, the TISE given by Eq. (29), becomes

$$\left\{\begin{pmatrix} -\frac{1}{2}\sum_{\alpha}\frac{\hat{p}_\alpha^2}{m_\alpha} & 0 & 0 \\ 0 & -\frac{1}{2}\sum_{\alpha}\frac{\hat{p}_\alpha^2}{m_\alpha} & 0 \\ 0 & 0 & -\frac{1}{2}\sum_{\alpha}\frac{\hat{p}_\alpha^2}{m_\alpha} \end{pmatrix} + \begin{pmatrix} V_{xx} & V_{xz} & 0 \\ V_{zx} & V_{zz} & 0 \\ 0 & 0 & V_{yy} \end{pmatrix}\right\}\begin{pmatrix} F_{zz} \\ F_{xx} \\ F_{yy} \end{pmatrix} = \begin{bmatrix} E & 0 & 0 \\ 0 & E & 0 \\ 0 & 0 & E \end{bmatrix}\begin{pmatrix} F_{zz} \\ F_{xx} \\ F_{yy} \end{pmatrix} \quad (37)$$

The resulting diabatic PESs are given by the following equations.

$$\begin{aligned} V_{xx}(r,\theta,R) &= V_{1^2A'}(r,\theta,R)\cos^2\gamma(r,\theta,R) + V_{2^2A'}(r,\theta,R)\sin^2\gamma(r,\theta,R) \\ V_{zz}(r,\theta,R) &= V_{1^2A'}(r,\theta,R)\sin^2\gamma(r,\theta,R) + V_{2^2A'}(r,\theta,R)\cos^2\gamma(r,\theta,R) \\ V_{xz}(r,\theta,R) &= \sin\gamma(r,\theta,R)\cos\gamma(r,\theta,R)\left(V_{1^2A'}(r,\theta,R) - V_{2^2A'}(r,\theta,R)\right) \\ V_{yy}(r,\theta,R) &= V_{A''}(r,\theta,R) \end{aligned} \quad (38)$$

However, as a consequence of truncating the electronic basis set and keeping only those terms in the ^2P manifold, DCTs involving states outside the basis have been neglected. This introduces error into the ADT mixing angle. This is best understood by decomposing the derivative coupling vector field into a transverse and longitudinal component.[68]

$$\vec{\tau}_{12}^{A} = \vec{\tau}_{12}^{A,t} + \vec{\tau}_{12}^{A,l} \quad (39)$$

The transverse and longitudinal component have the following properties.

$$\vec{\nabla}_{q_n} \cdot \vec{\tau}_{12}^{A,t} = 0 \quad (40)$$

$$\vec{\nabla}_{q_n} \times \vec{\tau}_{12}^{A,l} = 0$$

With these definitions, Eq. (33) becomes

$$\vec{\nabla}_{q_n} \times \vec{\tau}_{12}^{A} = \vec{\nabla}_{q_n} \times \vec{\tau}_{12}^{A,t} \qquad (41)$$

The error associated with the neglected coupling terms gives rise to a transverse component of the derivative coupling vector field which introduces path dependence in the line integral used to calculate the ADT mixing angle.[53, 56] This error cannot be removed and is often referred to as nonremovable component of the derivative coupling field.[57] While Eq. (34) can still be solved for the ADT mixing angle, the error will accumulate through each path. Diabatic surfaces affected by this error are termed quasi-diabatic surfaces. The accuracy of the resulting quasidiabatic states is determined the magnitude of the residual coupling. In the cases where this residual coupling is small the truncated basis is expected to adequately capture the nonadiabatic effects in the dynamics.[69]

Near a conical intersection the nonremovable coupling is small relative to the removable coupling, making a smaller overall contribution to the line integral.[70] As the distance from the conical intersection increases the removable and nonremovable couplings approach the same magnitude.[71] Consequently, the path used for the line integral has typically been restricted to regions of nuclear configuration space near a conical intersection to minimize the relative contribution of nonremovable error to the path integral.[72-76] The restricted range of nuclear coordinates also minimizes the errors introduced by finite grid spacing, thus allowing the location of the conical intersection to be determined with a high degree of accuracy.[73] Xu and coworkers have extended the line integral technique to search for conical intersections throughout all nuclear

configuration space for H_3. However, their method for calculating the NACTs relies on a semiempirical determination of the ADT matrix in conjunction with Hellmann-Feynman theorem and ensures a curl-free vector field.[77] Thus their line integral is constrained to be path independent.

Another approach for solving for the ADT mixing angle involves taking the divergence of Eq. (33) to obtain

$$\vec{\nabla}_{q_n} \cdot \vec{\tau}_{12}^{D} = \nabla_{q_n}^2 \gamma(\boldsymbol{q}_n) + \vec{\nabla}_{q_n} \cdot \vec{\tau}_{12}^{A} \qquad (42)$$

Using the definitions in Eq. (40) and assuming that the resulting diabatic NACTs are negligible Eq. (42) simplifies to

$$\nabla_{q_n}^2 \gamma(\boldsymbol{q}_n) = -\vec{\nabla}_{q_n} \cdot \vec{\tau}_{12}^{A,l} \qquad (43)$$

Eq. (43) is a Poisson's equation which allows the ADT mixing angle to be solved without performing a line integral. Work has been done to solve Eq. (43); however, the boundary conditions are unknown and must be approximated.[55, 78] Furthermore there are numerical restrictions on the regions where Eq. (43) can be solved.

The Asymptotic Basis

The calculation of scattering matrix elements is not conveniently done by solving the TISE in the diabatic electronic representation (Eq. (37)). The time-dependent CPM is one approach for calculating these scattering matrix elements.[43, 44] In this method the Hamiltonian for the B + H_2 system is represented using states defined in the asymptotic limit of the system.

In the asymptotic limit is reached as the distance *R* between B and H_2 becomes large. In the asymptotic limit the B + H_2 system consists of two non-interacting systems:

the boron atom and the H_2 molecule. The boron atom has a nucleus and five electrons and the H_2 molecule has two nuclei and two electrons. The terms in the full Hamiltonian can be classified according to the system they belong to. The full Hamiltonian for the B + H_2 system, excluding spin-orbit coupling, can be written as

$$\hat{H} = \hat{T}_N^B + \hat{T}_N^{H_2} + \hat{T}_e^B + \hat{V}_{el}^B + \hat{T}_e^{H_2} + \hat{V}_{el}^{H_2} + \hat{V}_{el} + E_{off} \quad (44)$$

The terms $\hat{T}_N^B$ and $\hat{T}_e^B$ represent the kinetic energy operators for the nucleus and electrons, respectively, of the boron system. The terms $\hat{T}_N^{H_2}$ and $\hat{T}_e^{H_2}$ represent the same for the H_2 system. The term $\hat{V}_{el}^B$ represents the Coulomb interaction potential between particles in the boron system only. The term $\hat{V}_{el}^{H_2}$ represents the same for the H_2 system. The term $\hat{V}_{el}$ represents the Coulomb interaction potential between the boron system and the H_2 system. This term has the form (in atomic units)

$$\hat{V}_{el} = \sum_{i,j} \frac{Z_{ai} Z_{mj}}{|\hat{\boldsymbol{q}}_{ai} - \hat{\boldsymbol{q}}_{mj}|} \quad (45)$$

In Eq. (45), the subscript *a* refers to particles associated with the atom, while the subscript *m* refers to particles associated with the molecule. The atomic number of a particle is given by *Z*. The set of position operators for each charged particle is given by $\hat{\boldsymbol{q}}$. Finally, the last term E_{off} represents a constant energy offset which has no effect on the eigenstates.

In the asymptotic limit of large *R* the contribution of the electrostatic interaction potential $\hat{V}_{el}$ to the total energy goes to zero, and the asymptotic Hamiltonian becomes

$$\hat{H}_0 = \hat{T}_N^B + \hat{T}_N^{H_2} + \hat{H}_{el}^B + \hat{H}_{el}^{H_2} + E_{off} \quad (46)$$

The eigenbasis of the asymptotic Hamiltonian $\hat{H}_0$ is a direct product of the states associated with each term of Eq. (46). The term $\hat{H}_{el}^B$ is the electronic Hamiltonian of

the boron system. This operator is the sum of all the Coulomb interaction terms between charged particles in the boron system as well as all the electron kinetic energy operators for the boron system. It can be expressed as

$$\hat{H}_{el}^{B} = \hat{T}_{e}^{B} + \hat{V}_{el}^{B} = \sum_{i} \frac{\hat{p}_{a,i}^{2}}{2m_e} + \sum_{i<j} \frac{Z_{ai} Z_{aj}}{|\hat{\boldsymbol{q}}_{ai} - \hat{\boldsymbol{q}}_{aj}|} \qquad (47)$$

$\hat{H}_{el}^{H_2}$ represents the same for the H_2 system and is expressed as

$$\hat{H}_{el}^{H_2} = \hat{T}_{e}^{H_2} + \hat{V}_{el}^{H_2} = \sum_{i} \frac{\hat{p}_{m,i}^{2}}{2m_e} + \sum_{i<j} \frac{Z_{mi} Z_{mj}}{|\hat{\boldsymbol{q}}_{mi} - \hat{\boldsymbol{q}}_{mj}|} \qquad (48)$$

As discussed earlier, the basis of electronic eigenfunctions was truncated to include only the 2*p* orbitals associated with the unpaired boron electron. These orbitals are also eigenfunctions of the term $\hat{H}_{el}^{B}$. The electronic eigenstates of the boron atom are represented by $|\ell, \Lambda\rangle$. When spin-orbit coupling is ignored the states $|\ell = 1, \Lambda = 0, \pm 1\rangle$ are degenerate with an energy of $E_B^{^2P}$ corresponding to the boron ^2P term. As the other sources of angular momentum of the B + H_2 system are coupled the electronic eigenstates for the boron atom will be indexed by spin-orbit coupling labels.

The asymptotic basis of the electronic hydrogen molecule Hamiltonian includes only the ground electronic state represented by $\left|{}^1\Sigma_g^+\right\rangle$. In the asymptotic limit, its energy eigenvalue is given by the vibrational potential energy curve $V_{H_2}(r)$ which depends on the hydrogen bond length *r*. These eigenstates form the asymptotic electronic basis which is represented by $|\Sigma, \Lambda\rangle = \left|{}^1\Sigma_g^+\right\rangle \otimes |\ell = 1, \Lambda = 0, \pm 1\rangle$.

Representing Eqs. (47) and (48) in this basis yield the asymptotic energy of the system, as shown by

$$\langle \Sigma', \Lambda' | \{ \hat{H}_{el}^{B} + \hat{H}_{el}^{H_2} \} | \Sigma, \Lambda \rangle = E_B^{^2P} \delta_{\Sigma'\Sigma} \delta_{\Lambda'\Lambda} + V_{H_2}(r) \delta_{\Sigma'\Sigma} \delta_{\Lambda'\Lambda} \quad (49)$$

The operators $\hat{H}_{el}^{B}$ and $\hat{H}_{el}^{H_2}$ are diagonal in this representation. The potential $V_{H_2}(r)$ represents the vibrational potential energy of H_2 in its ground electronic state $|^1\Sigma_g^+\rangle$.

In previous work [26, 37], the hydrogen bond length was restricted to its equilibrium value $r = r_{eq}$. When r is held at a fixed value the asymptotic energy for the hydrogen molecule becomes a constant and can be eliminated along with the asymptotic energy of the boron atom by choosing E_{off} appropriately. In this work the requirement that $r = r_{eq}$ is relaxed. By relaxing the restriction on r, the asymptotic energy of H_2 is no longer a constant with respect to r. Consequently the r dependence of $V_{H_2}(r)$ cannot be eliminated and the constant energy offset $E_{off} = -E_B^{^2P}$ is used to eliminate $E_B^{^2P}$ only.

In anticipation of representing the full Hamiltonian in the asymptotic electronic basis $|\Sigma, \Lambda\rangle$, Eq. (46) can be written as

$$\hat{H}_0 = \hat{T}_N^B + \hat{T}_N^{H_2} + \hat{H}_{el}^{H_2} \quad (50)$$

Using the BF and SF coordinates developed earlier, the nuclear kinetic energy operators can be expressed in a CM frame as [79, 80]

$$\hat{T}_N^B + \hat{T}_N^{H_2} = \frac{\hat{p}_R^2}{2\mu_{B,H_2}} + \frac{\hat{p}_r^2}{2\mu_{H_2}} + \frac{\hat{j}^2}{2\mu_{H_2} r^2} + \frac{\hat{L}^2}{2\mu_{B,H_2} R^2} \quad (51)$$

In Eq. (51) the reduced masses are given by $\mu_{B,H_2} = 2m_B m_{H_2}/(m_B + 2m_{H_2})$ and $\mu_{H_2} = m_H/2$. The terms $\hat{p}_R$ and $\hat{p}_r$ are momentum operators conjugate to the coordinates R and r. The angular momentum operator $\hat{j}$ corresponds to the rigid rotor comprised of the H_2 molecule. The angular momentum operator $\hat{L}$ corresponds to the rigid rotor comprised of the boron atom and the CM of the H_2 molecule.

The asymptotic Hamiltonian $\hat{H}_0$ can now be expressed as

$$\hat{H}_0 = \frac{\hat{p}_R^2}{2\mu_{B,H_2}} + \frac{\hat{p}_r^2}{2\mu_{H_2}} + \frac{\hat{j}^2}{2\mu_{H_2} r^2} + \frac{\hat{L}^2}{2\mu_{B,H_2} R^2} + \hat{H}_{el}^{H_2} \qquad (52)$$

The operators in Eq. (52) can be grouped into a vibrational, translational, and rotational piece.

$$\hat{H}_0^{\text{vib}} = \frac{\hat{p}_r^2}{2\mu_{H_2}} + \hat{H}_{el}^{H_2} \qquad (53)$$

Eq. (53) describes the vibration of H_2 in its ground electronic state. This piece will be expressed in the coordinate representation using the Jacobi coordinate *r*.

Eq. (54) describes the translation of the boron atom with respect to the CM of H_2.

$$\hat{H}_0^{trns} = \frac{\hat{p}_R^2}{2\mu_{B,H_2}} \qquad (54)$$

The eigenfunctions of this translation operator are plane waves. Each plane wave is labeled by its corresponding momentum (in atomic units) given by $|\kappa\rangle$.

Eq. (55) describes the rotation of the H_2 molecule and the tumbling motion of the boron atom around the H_2 molecule.

$$\hat{H}_0^{\text{rot}} = \frac{\hat{j}^2}{2\mu_{H_2} r^2} + \frac{\hat{L}^2}{2\mu_{B,H_2} R^2} \qquad (55)$$

There are four contributions to the total angular momentum *J* for the B + H_2 system: *j, L,* ℓ*,* and *s*. These angular momentum must be coupled to produce a set of quantum numbers to index the rotational eigenfunctions. Dubernet and Hutson examine five different coupling schemes.[79] This work uses the coupling scheme labeled “case 1A” in their paper. This same scheme is described by Jouvet and Beswick.[81] This coupling scheme is illustrated in Figure 4.

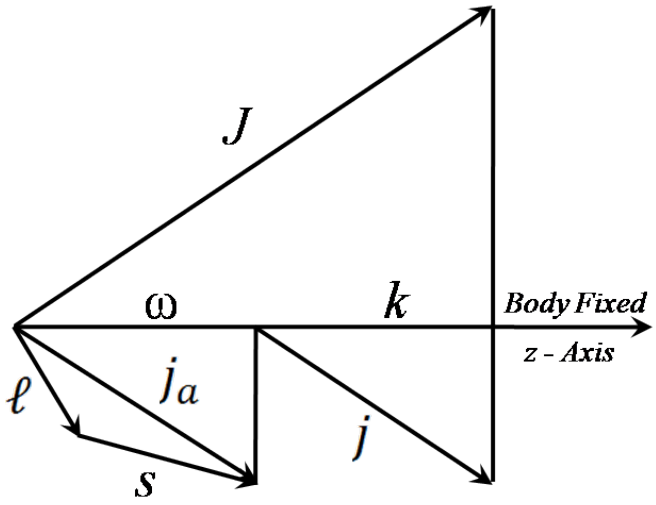

Figure 4. Angular momentum coupling scheme "case 1A" described by Dubernet and Hudson[79]

In this scheme the angular momenta ℓ and s associated with the orbital angular moment and spin of the unpaired boron electron couple to give j_a, which has a projection ω on the BF z axis. Earlier in this section the electronic eigenstates of boron, neglecting spin, were indexed by their orbital angular momentum Λ. In the coupled angular momentum scheme they are indexed by the spin-orbit indices j_a and ω. The angular moment of the H_2 rotor j has a projection k onto the BF z axis, and is not coupled with j_a. The total angular moment is given by

$$J = L + j + j_a \qquad (56)$$

The total angular momentum is chosen to have a projection on the BF z axis given by $P = k + \omega$ and a projection M onto the SF z axis. In the centrifugal sudden (CS) approximation $P = k + \omega$ is held constant. The angular momentum L of the tumbling motion of the boron atom with the CM of the hydrogen molecule has no projection along

the BF z axis since the boron atom and the CM of the hydrogen molecule lie along the BF z axis.

Using these labels, the basis functions of the spin-orbit coupled BF basis are labeled as follows:

$$|\zeta\rangle = \left|\begin{matrix} J & j & j_a \\ MP & k\ell_S & \omega \end{matrix}\right\rangle \qquad (57)$$

The label ζ is defined to correspond to properly chosen values for the quantum numbers in Eq (57). Spin-orbit coupling of the unpaired boron atom leads to $1/2$ and $3/2$ as the possible values of j_a, allowing ω to have values ranging from $-3/2$ to $3/2$ in integer steps. There are an infinite number of rotation energy states for the H_2 rotor, allowing j to range from zero on up in integer steps. The projection k ranges from $-j$ to j in integer steps. There is no quantum number associated with the tumbling motion of the boron atom and the CM of the hydrogen molecule in this coupling scheme. The possible values of the total angular momentum J range from $1/2$ on up in integer steps.

The complete basis of the asymptotic Hamiltonian is given by the direct product of the eigenfunctions for each of the terms in Eq. (52).

$$\begin{aligned} |\zeta, r, R\rangle &= |\zeta\rangle \otimes |r\rangle \otimes |R\rangle \otimes \left|{}^1\Sigma_g^+\right\rangle \\ &= \left|\begin{matrix} J & j & j_a \\ MP & k\ell_S & \omega \end{matrix}, r, R, \Sigma\right\rangle \end{aligned} \qquad (58)$$

The eigenfunctions form an orthonormal set as shown by

$$\langle \zeta', r', R' | \zeta, r, R\rangle = \delta_{\zeta',\zeta}\delta(r' - r)\delta(R' - R) \qquad (59)$$

Since the hydrogen molecule is restricted to the ground state it will be eliminated from the notation. These functions are now used to represent the full Hamiltonian.

The Asymptotic Representation

The full Hamiltonian, this time with a spin-orbit coupling term included, will be represented in the asymptotic given by Eq. (58).

$$\hat{H} = \frac{\hat{p}_R^2}{2\mu_{B,H_2}} + \frac{\hat{p}_r^2}{2\mu_{H_2}} + \frac{\hat{j}^2}{2\mu_{H_2} r^2} + \frac{\hat{L}^2}{2\mu_{B,H_2} R^2} + \hat{H}_{el}^{H_2} + \hat{V}_{el} + \hat{H}_{so} \qquad (60)$$

In Eq. (60), $\hat{H}_{so}$ is the spin-orbit term and the constant energy offset E_{off} has been used to eliminate the contribution of the electronic boron Hamiltonian $\hat{H}_{el}^{B}$. Since the asymptotic basis functions are not eigenfunctions of the full Hamiltonian, the form of the TISE in this representation will not be diagonal.

There are an infinite number of states in the asymptotic basis. For practical computational reasons this basis must also be truncated. For this work, only the states where $J = 1/2$, $M = +1/2$, and $P = +1/2$ are included. By truncating the electronic basis functions to include only the ^2P states of the boron atom $\ell = 1$, $s = 1/2$, and $j_a = 1/2, 3/2$. The hydrogen molecule is restricted to the ground electronic state. As shown in Eq. (61), the basis indices (Eq. (58)) can be simplified by eliminating the labels that remain constant.

$$|\zeta, r, R\rangle = \left| \begin{matrix} j & j_a \\ k & \omega \end{matrix}, r, R \right\rangle \qquad (61)$$

The matrix elements of the first term of the Hamiltonian (Eq.(60)), the radial kinetic energy term, are given by (in atomic units)

$$\left\langle \begin{matrix} j' & j_a' \\ k' & \omega' \end{matrix}, r', R' \middle| \frac{\hat{p}_R^2}{2\mu_{B,H_2}} \middle| \begin{matrix} j & j_a \\ k & \omega \end{matrix}, r, R \right\rangle = \frac{-1}{2\mu_{B,H_2} R} \frac{\partial^2}{\partial R^2} R \delta_{x'x} \qquad (62)$$

where $\delta_{x'x}$ is given by

$$\delta_{x'x} = \delta_{M'M}^{J'J} \delta_{P'P} \delta_{k'k}^{j'j} \delta_{\omega'\omega}^{j_a' j_a} \delta(r - r') \delta(R - R') \qquad (63)$$

The matrix elements of the vibrational kinetic energy term are given by Eq. (64).

$$\left\langle \begin{matrix} j' & j_a' \\ k' & \omega'' \end{matrix}, r', R' \middle| \frac{\hat{p}_r^2}{2\mu_{H_2}} \middle| \begin{matrix} j & j_a \\ k & \omega' \end{matrix}, r, R \right\rangle = \frac{-1}{2\mu_{H_2} r} \frac{\partial^2}{\partial r^2} r \delta_{x'x} \qquad (64)$$

The matrix elements of the H_2 rotational energy are given by Eq. (65).

$$\left\langle \begin{matrix} j' & j_a' \\ k' & \omega'' \end{matrix}, r', R' \middle| \frac{\hat{J}^2}{2\mu_{H_2} r^2} \middle| \begin{matrix} j & j_a \\ k & \omega' \end{matrix}, r, R \right\rangle = \frac{j(j+1)}{2\mu_{H_2} r^2} \delta_{x'x} \qquad (65)$$

Eqs. (62), (64), and (65) represent terms of the Hamiltonian that are diagonal in this basis.

The matrix elements of the angular momentum associated with the tumbling motion of the boron atom and the hydrogen molecule CM is not diagonal in this representation. The matrix elements are obtained by using Eq. (56) to express $\hat{L}^2$ as

$$\begin{aligned} \hat{L}^2 &= \hat{J}^2 + \hat{j}^2 + \hat{j}_a^2 - 2\hat{J}\cdot\hat{j} - 2\hat{J}\cdot\hat{j}_a + 2\hat{j}\cdot\hat{j}_a \\ &= \hat{J}^2 + \hat{j}^2 + \hat{j}_a^2 - \hat{J}^+\hat{j}_- - \hat{J}^-\hat{j}_+ - 2\hat{J}_z\hat{j}_z - \hat{J}^+\hat{j}_{a^-} - \hat{J}^-\hat{j}_{a^+} - 2\hat{J}_z\hat{j}_{a_z} + \hat{j}_+\hat{j}_{a^-} \\ &\quad + \hat{j}_-\hat{j}_{a^+} + 2\hat{j}_z\hat{j}_{a_z} \end{aligned} \qquad (66)$$

In Eq. (66) $\hat{J}^+$ and $\hat{J}^-$ are the raising and lowering operators of the total angular momentum operator. Likewise, $\hat{j}_+$, $\hat{j}_-$, $\hat{j}_{a^+}$ and $\hat{j}_{a^-}$ are the raising and lowing operators of the angular momentum operators $\hat{j}$ and $\hat{j}_a$ respectively. The matrix elements can then be calculated using the established properties of raising and lowering operators with one exception. The operation of $\hat{J}^{\pm}$ are reversed as a consequence of the BF angular momentum calculus.[82, 83] The terms in Eq. (66) can be classified as either diagonal or off-diagonal terms. The terms diagonal in this representation are those that do not include raising and lowering operators. These terms operate on the basis functions in the following way

$$\{\hat{J}^2+\hat{j}^2+\hat{j}_a^2-2\hat{J}_z\hat{j}_z-2\hat{J}_z\hat{j}_{a_z}+2\hat{j}_z\hat{j}_{a_z}\}\left|{}^{j\ j_a}_{k\ \omega},r,R\right\rangle$$
$$=\{J(J+1)+j(j+1)+j_a(j_a+1)-2(k+\omega)^2+2k\omega\}\left|{}^{j\ j_a}_{k\ \omega},r,R\right\rangle \quad (67)$$

The off-diagonal terms are given by Eqs. (68), (69), and (70).

$$\hat{J}^{\pm}\hat{j}_{\mp}\left|{}^{j\ j_a}_{k\ \omega},r,R\right\rangle$$
$$=\{(J(J+1)-P(P\mp1))(j(j+1)-k(k\mp1))\}^{1/2}\left|{}^{j\ \ j_a}_{k\mp1\ \omega},r,R\right\rangle \quad (68)$$

$$\hat{J}^{\pm}\hat{j}_{a^{\mp}}\left|{}^{j\ j_a}_{k\ \omega},r,R\right\rangle$$
$$=\{(J(J+1)-P(P\mp1))(j_a(j_a+1)-\omega(\omega\mp1))\}^{1/2}\left|{}^{j\ \ j_a}_{k\ \omega\mp1},r,R\right\rangle \quad (69)$$

$$\hat{J}_{\pm}\hat{j}_{a^{\mp}}\left|{}^{j\ j_a}_{k\ \omega},r,R\right\rangle=$$
$$\{(j(j+1)-k(k\pm1))(j_a(j_a+1)-\omega(\omega\mp1))\}^{1/2}\left|{}^{j\ \ j_a}_{k\pm1\ \omega\mp1},r,R\right\rangle \quad (70)$$

The matrix elements of the tumbling kinetic energy terms are then given by

$$\left\langle{}^{j'\ j'_a}_{k'\ \omega'},r',R'\right|\frac{\hat{L}^2}{2\mu_{B,H_2}R^2}\left|{}^{j\ j_a}_{k\ \omega},r,R\right\rangle=\left\langle{}^{j'\ j'_a}_{k'\ \omega'},r',R'\right|\frac{(\hat{J}-\hat{j}-\hat{j}_a)^2}{2\mu_{B,H_2}R^2}\left|{}^{j\ j_a}_{k\ \omega},r,R\right\rangle$$
$$=\frac{1}{2\mu_{B,H_2}R^2}\Big[\{J(J+1)+j(j+1)+j_a(j_a+1)-2(k+\omega)^2+2k\omega\}\delta_{x'x}$$
$$+\{(J(J+1)-P(P\mp1))(j(j+1)-k(k\mp1))\}^{1/2}\times\delta^{J'J}_{M'M}\delta^{j'j}_{k'k\mp1}\delta^{j'_aj_a}_{\omega'\omega}\delta(r-r')\delta(R-R') \quad (71)$$
$$+\{(J(J+1)-P(P\mp1))(j_a(j_a+1)-k(k\mp1))\}^{1/2}\times\delta^{J'J}_{M'M}\delta^{j'j}_{k'k}\delta^{j'_aj_a}_{\omega'\omega\mp1}\delta(r-r')\delta(R-R')$$
$$+\{(j(j+1)-k(k\pm1))(j_a(j_a+1)-\omega(\omega\mp1))\}^{1/2}$$
$$\times\delta^{J'J}_{M'M}\delta_{P'P}\delta^{j'j}_{k'k\pm1}\delta^{j'_aj_a}_{\omega'\omega\mp1}\delta(r-r')\delta(R-R')\Big]$$

Eq. (71) is grouped into four terms, each of which couples states for which $\Delta j=0$ and $\Delta j_a=0$. The second and third terms couple states for which $\Delta P\neq0$. It is common to neglect these terms by invoking the CS approximation.[84-89] This approximation assumes that the interaction takes place rapidly enough that the projection P of the total angular momentum is conserved. This work uses the CS approximation.

The spin-orbit coupling operator is given by $\hat{H}_{so} = \xi\hat{\ell}\cdot\hat{s}$ where $\hat{\ell}$ and $\hat{s}$ are the orbital and spin angular momentum operators of the unpaired $2p^1$ boron electron. The matrix elements of this operator in the asymptotic basis are given by Eq. (72).

$$\left\langle \begin{matrix} j' & j'_a \\ k' & \omega' \end{matrix}, r', R' \middle| \hat{H}_{so} \middle| \begin{matrix} j & j_a \\ k & \omega \end{matrix}, r, R \right\rangle = \frac{\xi}{2}\{j_a(j_a+1) - \ell(\ell+1) - s(s+1)\}\delta_{x'x} \qquad (72)$$

In this expression, the atomic boron value of ξ is 4.876×10^{-5} atomic units. For this calculation the spin-orbit coefficient ξ is assumed to be constant and is set to the atomic boron value. This is called the "pure precession" approximation.[26] In general, ξ changes as a function of the nuclear coordinates due to the perturbation of the boron atomic orbital.

The electrostatic interaction potential $\hat{V}_{el}$ has a straightforward representation in the coupled angular momentum asymptotic basis when first expanded using a standard multipole expansion.[90] The multipole expansion has the form (in atomic units)

$$\begin{aligned} \hat{V}_{el} &= \sum_{i,j} \frac{Z_{ai}Z_{mj}}{|\hat{q}_{ai} - \hat{q}_{mj}|} \\ &= \sum_{\lambda_r\lambda_a\mu} V_{\lambda_r\lambda_a\mu}(R,r) C_{\mu}^{\lambda_r}(\theta,\phi) C_{-\mu}^{\lambda_r}(\theta_a,\phi_a) \end{aligned} \qquad (73)$$

In Eq. (73) the electrostatic interaction potential is expanded in terms of renormalized spherical harmonics, $C_{\mu}^{\lambda_r}(\theta,\phi)$. The coordinates θ_a and ϕ_a are the polar and azimuthal angles corresponding to the unpaired B($2p^1$) electron. All of the other electronic and nuclear coordinates have been integrated over. The form of this expansion assumes that mixing of states outside the ^2P manifold will be weak.[79] Eq. (73) has the following form when represented in the coupled angular momentum basis:

$$\left\langle \begin{matrix} j' & j_a' \\ k' & \omega' \end{matrix}, r', R' \middle| \hat{V}_{el} \middle| \begin{matrix} j & j_a \\ k & \omega \end{matrix}, r, R \right\rangle$$
$$= \sum_{\lambda_r \lambda_a \mu} V_{\lambda_r \lambda_a \mu}(r, R) \left\langle \begin{matrix} j' \\ k' \end{matrix} \middle| C_{\mu}^{\lambda_r}(\theta, \phi) \middle| \begin{matrix} j \\ k \end{matrix} \right\rangle \left\langle \begin{matrix} j_a' \\ \omega' \end{matrix} \middle| C_{-\mu}^{\lambda_r}(\theta_a, \phi_a) \middle| \begin{matrix} j_a \\ \omega \end{matrix} \right\rangle \delta_{M'M}^{J'J} \delta_{P'P} \delta_{\nu'\nu} \delta(\kappa^{\gamma'} - \kappa^{\gamma}) \quad (74)$$

The inner products in Eq. (74) are evaluated using the Wigner-Eckhart Theorem yielding Eqs. (75) and (76).

$$\left\langle \begin{matrix} j' \\ k' \end{matrix} \middle| C_{\mu}^{\lambda_r}(\theta, \phi) \middle| \begin{matrix} j \\ k \end{matrix} \right\rangle = (-1)^k [(2j+1)(2j'+1)]^{1/2} \begin{pmatrix} j' & \lambda_r & j \\ -k' & \mu & k \end{pmatrix} \begin{pmatrix} j' & \lambda_r & j \\ 0 & 0 & 0 \end{pmatrix} \quad (75)$$

$$\left\langle \begin{matrix} j_a' \\ \omega' \end{matrix} \middle| C_{-\mu}^{\lambda_r}(\hat{\theta}_a, \hat{\phi}_a) \middle| \begin{matrix} j_a \\ \omega \end{matrix} \right\rangle = (-1)^{\omega - s} (2\ell + 1)[(2j_a + 1)(2j_a' + 1)]^{1/2} \times \begin{Bmatrix} j_a' & \lambda_a & j_a \\ \ell & s & \ell \end{Bmatrix} \begin{pmatrix} j_a' & \lambda_a & j_a \\ \omega & -\mu & -\omega' \end{pmatrix} \begin{pmatrix} \ell & \lambda_a & \ell \\ 0 & 0 & 0 \end{pmatrix} \quad (76)$$

In Eqs. (75) and (76) 3-*j* symbols are represented as $(:::)$ and 6-*j* symbols are represented as $\{:::\}$.[37, 82, 83, 91] In Appendix E the symmetry of the electrostatic interaction potential is explored. The expansion coefficients $V_{\lambda_r \lambda_a \mu}(r, R)$ are found by expanding the numerical diabatic PESs V_{xx}, V_{zz}, V_{yy}, and V_{xz} (Eq. (37)) in terms of renormalized spherical harmonics and performing a term-by-term comparison with the analytic expansion of the electrostatic interaction potential.[26, 27, 79]

Comparing the full Hamiltonian as expressed in Eq. (44) with the electronic Hamiltonian, Eq. (11), the following connection is established:

$$\begin{aligned} \hat{H}_{elec} &= \hat{T}_e^B + \hat{V}_{el}^B + \hat{T}_e^{H_2} + \hat{V}_{el}^{H_2} + \hat{V}_{el} + E_{off} \\ &= \hat{H}_{el}^{H_2} + \hat{V}_{el} \end{aligned} \quad (77)$$

As explained earlier, Eq. (77) was solved using *ab initio* techniques resulting in adiabatic PESs. The ADT mixed these surfaces to form diabatic PESs. As shown in Eq. (37), when the electronic Hamiltonian is represented in the diabatic basis is has the block diagonal form shown below.

$$V^D(r,\theta,R) = \begin{array}{c|ccc} & |z\rangle & |x\rangle & |y\rangle \\ \hline \langle z| & V_{zz} & V_{zx} & 0 \\ \langle x| & V_{xz} & V_{xx} & 0 \\ \langle y| & 0 & 0 & V_{yy} \end{array} \qquad (78)$$

In order to make a comparison to the numerical PESs, the analytic expansion of Eq. (77) in the asymptotic basis must include the contributions of both $\hat{V}_{el}$ and $\hat{H}_{el}^{H_2}$. This is done by representing the electronic Hamiltonian using the asymptotic electronic basis $|\Sigma,\Lambda\rangle = \left|{}^1\Sigma_g^+\right\rangle \otimes |\ell = 1, \Lambda = 0, \pm 1\rangle$ as opposed to the coupled angular momentum basis used in Eqs. (74), (75), and (76).

$$V^D_{\Lambda'\Lambda}(r,\theta,R) = \langle\Sigma',\Lambda'|\hat{V}_{el} + \hat{H}_{el}^{H_2}|\Sigma,\Lambda\rangle$$

$$= \langle\Sigma',\Lambda'|\sum_{i,j}\frac{Z_{ai}Z_{mj}}{|\hat{q}_{ai} - \hat{q}_{mj}|}|\Sigma,\Lambda\rangle + \langle\Sigma',\Lambda'|\hat{H}_{el}^{H_2}|\Sigma,\Lambda\rangle$$

$$= \sum_{\lambda_r\lambda_a\mu} V_{\lambda_r\lambda_a\mu}(r,R)C_\mu^{\lambda_r}(\theta,\phi)\left\langle\Lambda'\middle|C_{-\mu}^{\lambda_r}(\theta_a,\phi_a)\middle|\Lambda\right\rangle\delta_{\Sigma'\Sigma} + V_{H_2}(r)\delta_{\Sigma'\Sigma}\delta_{\Lambda'\Lambda} \qquad (79)$$

$$= 3\sum_{\lambda_r\lambda_a\mu} V_{\lambda_r\lambda_a\mu}(r,R)C_\mu^{\lambda_r}(\theta,\phi)\left[(-1)^{2-\Lambda'}\begin{pmatrix}1 & \lambda_a & 1\\ -\Lambda' & -\mu & \Lambda\end{pmatrix}\begin{pmatrix}1 & \lambda_a & 1\\ 0 & 0 & 0\end{pmatrix}\right]\delta_{\Sigma'\Sigma}$$
$$+ V_{H_2}(r)\delta_{\Sigma'\Sigma}\delta_{\Lambda'\Lambda}$$

In Eq. (79) the results of Eq. (49) have been applied. The electronic Hamiltonian of the hydrogen molecule becomes the ground state vibrational potential $V_{H_2}(r)$. The electronic part of the electrostatic interaction potential has been expanded in terms of 3-*j* symbols using the Wigner-Eckhart Theorem.

The potential $V_{H_2}(r)$ only depends on the hydrogen bond length coordinate r. Only the constant renormalized spherical harmonic term $C_0^0(\theta,\phi)$ is required to fit this potential. Eq. (79) can be written as

$$V^{D}_{\Lambda'\Lambda}(r,\theta,R)$$
$$= 3\sum_{\lambda_r\lambda_a\mu} V_{\lambda_r\lambda_a\mu}(r,R)C^{\lambda_r}_{\mu}(\theta,\phi)\left[(-1)^{2-\Lambda'}\begin{pmatrix}1 & \lambda_a & 1\\ -\Lambda' & -\mu & \Lambda\end{pmatrix}\begin{pmatrix}1 & \lambda_a & 1\\ 0 & 0 & 0\end{pmatrix}\right]\delta_{\Sigma'\Sigma} \qquad (80)$$
$$+ V_{H_2}(r)C^{0}_{0}(\theta,\phi)\delta_{\Sigma'\Sigma}\delta_{\Lambda'\Lambda}$$

The $\delta_{\Sigma'\Sigma}$ terms will always evaluate to unity since H_2 is restricted to its ground electronic state.

The properties of the 3-*j* symbols lead to further simplifications to Eq. (80). The triangle inequality $|1-\lambda_a| \le 1 \le |1+\lambda_a|$ restricts the values of λ_a to 0, 1, and 2. 3-*j* symbols also have the property

$$\begin{pmatrix}a & b & c\\ 0 & 0 & 0\end{pmatrix} = 0 \qquad (81)$$

when the sum $(a+b+c)$ is odd. These properties lead to

$$V^{D}_{\Lambda'\Lambda}(r,\theta,R) = \sum_{\lambda_r\mu} C^{\lambda_r}_{\mu}(\theta,\phi)\left[V_{\lambda_r 00}(r,R)(-1)^{3-\Lambda'}(3)^{1/2}\begin{pmatrix}1 & 0 & 1\\ -\Lambda' & 0 & \Lambda\end{pmatrix}\delta_{\mu,0}\delta_{\Lambda'\Lambda}\right.$$
$$+ V_{\lambda_r 2\mu}(r,R)(-1)^{2-\Lambda'}\left(\frac{6}{5}\right)^{1/2}\begin{pmatrix}1 & 2 & 1\\ -\Lambda' & -\mu & \Lambda\end{pmatrix}\delta_{\mu,\Lambda'-\Lambda} \qquad (82)$$
$$\left. + V_{H_2}(r)C^{0}_{0}(\theta,\phi)\delta_{\Lambda'\Lambda}\right]$$

In Eq. (82), the values of μ are determined by the bottom row of the 3-*j* symbol. This property requires that $-\Lambda'-\mu+\Lambda=0$, or $\mu=\Lambda-\Lambda'$, where Λ and Λ' can be 0 and ±1. Thus μ takes on values ranging from –2 to 2 in integer steps. The matrix elements of the diabatic electronic potential energy Λ' including the contribution from the H_2 molecule can be written as

$$V^D(r,\theta,R)=\begin{array}{c|ccc} & |1\rangle & |0\rangle & |-1\rangle \\ \hline \langle 1| & V_{00}-\frac{1}{5}V_{20}+V_{H_2}\delta_{\lambda_r,0} & -\frac{\sqrt{3}}{5}V_{21} & -\frac{\sqrt{6}}{5}V_{22} \\ \langle 0| & -\frac{\sqrt{3}}{5}V_{21} & V_{00}+\frac{2}{5}V_{20}+V_{H_2}\delta_{\lambda_r,0} & \frac{\sqrt{3}}{5}V_{21} \\ \langle -1| & -\frac{\sqrt{6}}{5}V_{22} & \frac{\sqrt{3}}{5}V_{21} & V_{00}-\frac{1}{5}V_{20}+V_{H_2}\delta_{\lambda_r,0} \end{array} \quad (83)$$

The matrix elements of $V^D(R,\theta,r)$ are expressed in terms of coefficients $V_{\lambda_a\mu}$ given by

$$V_{\lambda_a\mu}=-V_{\lambda_a-\mu}=\sum_{\lambda_r}C_\mu^{\lambda_r}(\theta,\phi=0)V_{\lambda_r\lambda_a\mu}(r,R) \quad (84)$$

To cast $V^D(r,\theta,R)$ into a form which can be compared with the numerical *ab initio* diabatic PESs, the following transformation to the Cartesian basis is made.

$$\begin{aligned} |x\rangle &= \frac{1}{\sqrt{2}}(-|1\rangle+|-1\rangle) \\ |y\rangle &= \frac{i}{\sqrt{2}}(|1\rangle+|-1\rangle) \\ |z\rangle &= |0\rangle \end{aligned} \quad (85)$$

This transformation yields the following expression for $V^D(R,\theta,r)$:

$$V^D(r,\theta,R)=\begin{array}{c|ccc} & |z\rangle & |x\rangle & |y\rangle \\ \hline \langle z| & V_{00}+\frac{2}{5}V_{20}+V_{H_2}\delta_{\lambda_r,0} & \frac{\sqrt{6}}{5}V_{21} & 0 \\ \langle x| & \frac{\sqrt{6}}{5}V_{21} & V_{00}-\frac{1}{5}V_{20}+\frac{\sqrt{6}}{5}V_{22}+V_{H_2}\delta_{\lambda_r,0} & 0 \\ \langle y| & 0 & 0 & V_{00}-\frac{1}{5}V_{20}-\frac{\sqrt{6}}{5}V_{22}+V_{H_2}\delta_{\lambda_r,0} \end{array} \quad (86)$$

As expected, $V^D(r,\theta,R)$ has the same block diagonal form as Eq. (78). Eq. (86) is the analytical form of the electrostatic Hamiltonian, Eq. (77). Now the numerical diabatic PES must be fit to the same functional form so that a term-by-term comparison can be made.

The numerical diabatic PESs are expanded in terms of reduced Wigner rotation matrix elements which have the following relationship to renormalized spherical harmonics[82, 83]

$$d_{\mu 0}^{\lambda_r}(\theta) = \left(\frac{4\pi}{2\lambda_r + 1}\right) Y_{\mu}^{\lambda_r *}(\theta, \phi = 0) = C_{\mu}^{\lambda_r}(\theta, \phi = 0) \tag{87}$$

The following functions are used to fit each diabatic PES.

$$\begin{aligned}
V_{zz}(r,\theta,R) &= \sum_{\lambda_r=0} V_{zz}^{\lambda_r}(r,R)\, d_{00}^{\lambda_r}(\theta) \\
V_{xz}(r,\theta,R) &= \sum_{\lambda_r=1} V_{xz}^{\lambda_r}(r,R)\, d_{10}^{\lambda_r}(\theta) \\
V_{xx}(r,\theta,R) &= V_s(r,\theta,R) + V_d(r,\theta,R) \\
&= \sum_{\lambda_r=0} V_s^{\lambda_r}(r,R)\, d_{00}^{\lambda_r}(\theta) + \sum_{\lambda_r=2} V_d^{\lambda_r}(r,R)\, d_{20}^{\lambda_r}(\theta) \\
V_{yy}(r,\theta,R) &= V_s(r,\theta,R) - V_d(r,\theta,R) \\
&= \sum_{\lambda_r=0} V_s^{\lambda_r}(r,R)\, d_{00}^{\lambda_r}(\theta) - \sum_{\lambda_r=2} V_d^{\lambda_r}(r,R)\, d_{20}^{\lambda_r}(\theta)
\end{aligned} \tag{88}$$

The functions $V_s(r,\theta,R)$ and $V_d(r,\theta,R)$ are introduced to separate fitting functions with different symmetry, in this case the $d_{00}^{\lambda_r}(\theta)$ and $d_{20}^{\lambda_r}(\theta)$ terms. They are defined as

$$\begin{aligned}
V_s(r,\theta,R) &= \tfrac{1}{2}\left[V_{xx}(r,\theta,R) + V_{yy}(r,\theta,R)\right] \\
V_d(r,\theta,R) &= \tfrac{1}{2}\left[V_{xx}(r,\theta,R) - V_{yy}(r,\theta,R)\right]
\end{aligned} \tag{89}$$

The function $V_d(r,\theta,R)$ can also be defined as

$$V_d(r,\theta,R) = \tfrac{1}{2}\left[V_{yy}(r,\theta,R) - V_{xx}(r,\theta,R)\right] \tag{90}$$

Both definitions have been found in the literature (Weeks[37] uses Eq. (89) while Alexander[26, 27] uses Eq. (90)), and the choice is arbitrary.

The fit coefficients in Eq. (88) are compared term-by-term with the corresponding expansion coefficients in Eq. (86) yielding

$$\begin{aligned} V_{zz}^{\lambda_r}(r,R) &= V_{\lambda_r 00}(r,R) + \frac{2}{5}V_{\lambda_r 20}(r,R) + V_{H_2}(r)\delta_{\lambda_r,0} \\ V_{xz}^{\lambda_r}(r,R) &= \frac{\sqrt{6}}{5}V_{\lambda_r 21}(r,R) \\ V_{s}^{\lambda_r}(r,R) &= V_{\lambda_r 00}(r,R) - \frac{1}{5}V_{\lambda_r 20}(r,R) + V_{H_2}(r)\delta_{\lambda_r,0} \\ V_{d}^{\lambda_r}(r,R) &= \frac{\sqrt{6}}{5}V_{\lambda_r 22}(r,R) \end{aligned} \qquad (91)$$

These equations are then inverted to give the desired fit coefficients $V_{\lambda_r\lambda_a\mu}(r,R)$ in terms of the expansion coefficients of the numerical PESs.

$$\begin{aligned} V_{\lambda_r 00}(r,R) &= \frac{1}{3}\left(V_{zz}^{\lambda_r}(r,R) + 2V_{s}^{\lambda_r}(r,R)\right) - V_{H_2}(r)\delta_{\lambda_r,0} \\ V_{\lambda_r 20}(r,R) &= \frac{5}{3}\left(V_{zz}^{\lambda_r}(r,R) - V_{s}^{\lambda_r}(r,R)\right) \\ V_{\lambda_r 21}(r,R) &= \frac{5}{\sqrt{6}}V_{xz}^{\lambda_r}(r,R) \\ V_{\lambda_r 22}(r,R) &= \frac{5}{\sqrt{6}}V_{d}^{\lambda_r}(r,R) \end{aligned} \qquad (92)$$

As seen in Eq. (92) the definition of $V_d(r,\theta,R)$ introduces a sign change in the $V_{\lambda_r 22}(r,R)$ expansion coefficients. The sign of $V_{\lambda_r 22}(r,R)$ was verified to have no effect on the calculation of the electrostatic interaction potential $\hat{V}_{el}$.

Now that the expansion coefficients $V_{\lambda_r\lambda_a\mu}(r,R)$ are known, the representation of the electrostatic interaction potential $\hat{V}_{el}$ in the coupled angular momentum asymptotic basis given by Eq. (74) is complete.

Structure of the Asymptotic Representation

The full Hamiltonian, Eq. (60), is not diagonal when expressed as a matrix in the asymptotic representation. The Kronecker deltas that appear in the matrix elements for each term in the full Hamiltonian determine which asymptotic basis states, defined by the labels in Eq. (57), will couple with one another. Terms which have the Kronecker delta $\delta_{x'x}$, Eq. (63), are completely diagonal in the asymptotic representation. This includes the radial and vibrational kinetic energy operators (Eqs. (62) and (64)), the spin-orbit coupling operator (Eq. (72)), the rotational kinetic energy operator of the H_2 molecule (Eq. (65)), and the electronic Hamiltonian of the hydrogen molecule (Eq. (79)) are diagonal in the asymptotic representation.

The rotational kinetic energy of the boron atom with the CM of the H_2 molecule (Eq. (71)) and the electrostatic interaction potential (Eq. (74)) are not diagonal in the asymptotic representation. By examining the Kronecker deltas in these terms, the matrix elements can be organized into a hierarchy of block diagonal pieces, each of which is infinitely large. The *J* block are the largest in this hierarchy. Each *J* block is subdivided into *M* sub-blocks. Each *M* block contains identical information about the system, so only one *M* block needs to be considered. This is illustrated in Figure 5 for a truncated *J* = $+1/2$ block. The grey regions in Figure 5 are zero. Under the CS approximation, the gray regions within a given *M* block are zero; however, when this approximation is lifted the entire *M* block may have non-zero values.

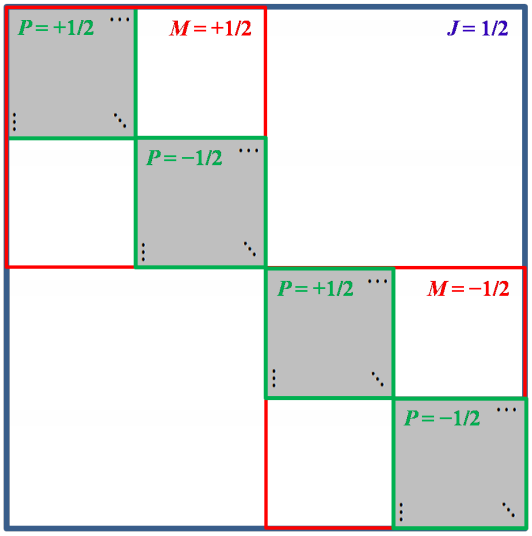

Figure 5. A visualization of the $J = 1/2$ block of the matrix elements of the asymptotic Hamiltonian

As shown in Figure 5, each M block (red) is further subdivided into smaller P blocks (green). The ellipses indicate that each P block is infinite in dimension. The grey regions indicate the location of non-zero matrix elements. The white regions are where the matrix elements are zero. The electrostatic interaction potential is diagonal in this block. The Kronecker delta $\delta_{P'P}$ in Eq. (74) reinforces a result that arises from the 3-j symbols in Eq. (75) and (76). The following two equations are obtained using the condition that the bottom row of a 3-j symbol must sum to zero:

$$\begin{aligned} -k' + \mu + k &= 0 \\ \omega - \mu - \omega' &= 0 \end{aligned} \qquad (93)$$

These equations imply that $k' + \omega' = k + \omega$, or $\Delta P = 0$.[91] However, the matrix elements of the tumbling motion of boron and H_2 molecule are not diagonal in the P block. This is the primary reason for invoking the CS approximation. Under the CS approximation off-diagonal P blocks are zero, and a specific P block can be chosen for the calculation rather than having to consider the entire M block.

The P block can be further subdivided into a parahydrogen block and an orthohydrogen block. Since these states do not couple they are block diagonal in P. In this work only transitions from the ground rotational state $j = 0$ re considered. This restricts the basis functions to include only parahydrogen states ($j = 0,2,4,6$ ...).

Given that only even values of j will be used and that j_a will be either $1/2$ or $3/2$, the basis functions for the $J = 1/2$ block under the CS approximation can be identified. This work examines the $P = +1/2$ block, which leads to the requirement that $k + \omega = +1/2$. The basis functions which meet this requirement are shown below.

$$j = 0, \quad \left| \begin{matrix} j & j_a \\ k & \omega \end{matrix} \right\rangle \in \left\{ \left| \begin{matrix} 0 & 1/2 \\ 0 & 1/2 \end{matrix} \right\rangle , \left| \begin{matrix} 0 & 3/2 \\ 0 & 1/2 \end{matrix} \right\rangle \right\} \tag{94}$$

$$j = 2,4,6\ldots, \quad \left| \begin{matrix} j & j_a \\ k & \omega \end{matrix} \right\rangle \in \left\{ \left| \begin{matrix} j & 3/2 \\ 2 & -3/2 \end{matrix} \right\rangle , \left| \begin{matrix} j & 3/2 \\ 1 & -1/2 \end{matrix} \right\rangle , \left| \begin{matrix} j & 1/2 \\ 1 & -1/2 \end{matrix} \right\rangle , \left| \begin{matrix} j & 1/2 \\ 0 & 1/2 \end{matrix} \right\rangle , \left| \begin{matrix} j & 3/2 \\ 0 & 1/2 \end{matrix} \right\rangle , \left| \begin{matrix} j & 3/2 \\ -1 & 3/2 \end{matrix} \right\rangle \right\} \tag{95}$$

As shown in Figure 6, the parahydrogen block has a 2-by-2 sub-block corresponding to $j = 0$. For each additional value of j considered an additional six basis functions are added. At first glance, it does not seem that some of the basis functions in Eq. (94) and (95) belong in the $J = 1/2$ block since their values for j and j_a sum to greater than $1/2$. Their inclusion in this block is a consequence of how the three angular momenta of this system couple to give the total angular momentum.[83]

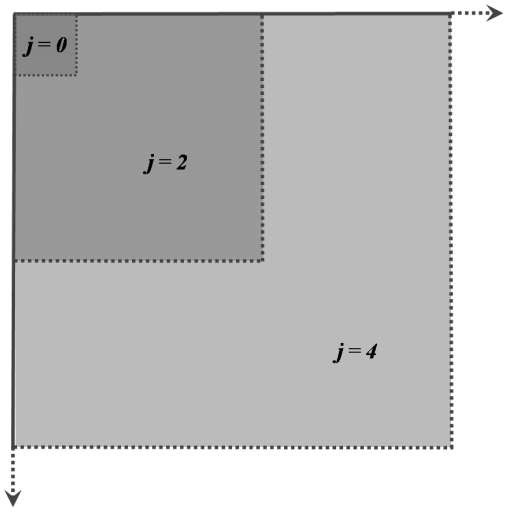

Figure 6. A visualization of the parahydrogen block within the *P* sub-block of the matrix elements of the asymptotic Hamiltonian

Since an infinite number of basis function cannot be considered in a numerical calculation, the basis set must be truncated. This is done by considering values of j for which the rotational energy is less than the total energy of the collision being considered. This threshold value of j is designated j_{max} and leads to a basis size given by $d = 2 + 3j_{max}$. The rotational energy levels (in atomic units) of the H_2 rotor are given by

$$E_j(r) = \frac{j(j+1)}{2\mu_{H_2} r^2} \qquad (96)$$

These energies depend on the bond length of H_2 which is no longer a constant. However, for the energies considered in this work, the equilibrium bond length is used as an estimate. Energies between 0.0 a.u. and 0.01 a.u. are considered (less than the energy required to excite the first vibrational mode of H_2). Using Eq. (96), this leads to $j_{max} = 6$ and a basis size of 20.

The Time-Dependent Schrödinger Equation

The time-dependent Schrödinger equation (TDSE) can be represented using the basis functions defined by Eqs. (94) and (95). The general form of the TDSE is given by Eq. (2). The Hamiltonian can be broken into a kinetic energy term and a potential energy term. For the B + H_2 system the kinetic term is composed of the kinetic energy operators given by Eqs. (62) and (64). The potential energy term is the sum of the H_2 rotational and tumbling kinetic energy, the electrostatic interaction potential, and the spin-orbit coupling. The matrix elements of this operator are referred to as effective PES and are given by

$$V_{eff}^{D}(r,R)_{\zeta'\zeta} = \left\langle \zeta', r', R' \left| \frac{\hat{L}^2}{2\mu_{B,H_2}R^2} + \frac{\hat{\jmath}^2}{2\mu_{H_2}r^2} + \hat{V}_{el} + \hat{H}_{el}^{H_2} + \hat{H}_{so} \right| \zeta, r, R \right\rangle \qquad (97)$$

The labels ζ and ζ' represent states for which appropriate values for each of the labels in Eq. (57) have been chosen. The superscript D is used to indicate that $V_{eff}^{D}(R,r)_{\zeta'\zeta}$ is not diagonal in this representation.

In matrix form, the TDSE is given by (atomic units)

$$\begin{aligned} i\frac{\partial}{\partial t}\begin{pmatrix} \Phi_1(r,R,t) \\ \Phi_2(r,R,t) \\ \vdots \end{pmatrix} &= \begin{pmatrix} H_{11} & H_{12} & \cdots \\ H_{21} & H_{22} & \cdots \\ \vdots & \vdots & \ddots \end{pmatrix}\begin{pmatrix} \Phi_1(r,R,t) \\ \Phi_2(r,R,t) \\ \vdots \end{pmatrix} \\ &= \left[\left\{ \frac{-1}{2\mu_{B,H_2}}\frac{\partial^2}{\partial R^2} - \frac{-1}{2\mu_{H_2}}\frac{\partial^2}{\partial r^2} \right\}\begin{pmatrix} 1 & 0 & \cdots \\ 0 & 1 & \cdots \\ \vdots & \vdots & \ddots \end{pmatrix} \right. \\ &\quad \left. + \begin{pmatrix} V_{eff}^{D}(r,R)_{11} & V_{eff}^{D}(r,R)_{12} & \cdots \\ V_{eff}^{D}(r,R)_{21} & V_{eff}^{D}(r,R)_{22} & \cdots \\ \vdots & \vdots & \ddots \end{pmatrix} \right] \begin{pmatrix} \Phi_1(r,R,t) \\ \Phi_2(r,R,t) \\ \vdots \end{pmatrix} \end{aligned} \qquad (98)$$

where the radial kinetic energy and the vibrational kinetic energy operators have been simplified by introducing the reduced wave function $\Phi(r,R,t) = rR\Psi(r,R,t)$. The formal solution (in atomic units) governing the time evolution of the reduced wave functions is

$$\begin{pmatrix}\Phi_1(r,R,\Delta t)\\ \Phi_2(r,R,\Delta t)\\ \vdots\end{pmatrix} = exp\left[-i\begin{pmatrix}H_{11} & H_{12} & \cdots\\ H_{21} & H_{22} & \cdots\\ \vdots & \vdots & \ddots\end{pmatrix}\Delta t\right]\begin{pmatrix}\Phi_1(r,R,0)\\ \Phi_2(r,R,0)\\ \vdots\end{pmatrix} \quad (99)$$

Eq. (99) represents the time evolution of a collection of wave functions, denoted $\Phi_i(r,R,\Delta t)$, under the influence of the Hamiltonian ***H***. The time interval is given by Δt.

The wave functions propagate on a potential surface given by a corresponding diagonal element of $V_{eff}^{D}(r,R)$. However, with each propagation step Δt the off-diagonal elements of $V_{eff}^{D}(r,R)$ couple the wave functions causing probability amplitude to be redistributed over the entire collection of PESs. If the effective potential energy $V_{eff}^{D}(r,R)$ were diagonal, this redistribution would not occur and each wave function would propagate independently on its own potential surface.

Eq. (99) can be expressed in a form more suitable for numeric computation by applying the split operator approximation (SOA).

$$\begin{pmatrix}\Phi_1(r,R,\Delta t)\\ \Phi_2(r,R,\Delta t)\\ \vdots\end{pmatrix} \approx exp\left[-i\begin{pmatrix}V_{11} & V_{12} & \cdots\\ V_{21} & V_{22} & \cdots\\ \vdots & \vdots & \ddots\end{pmatrix}\frac{\Delta t}{2}\right]exp\left[-i\begin{pmatrix}T_{11} & T_{12} & \cdots\\ T_{21} & T_{22} & \cdots\\ \vdots & \vdots & \ddots\end{pmatrix}\Delta t\right]exp\left[-i\begin{pmatrix}V_{11} & V_{12} & \cdots\\ V_{21} & V_{22} & \cdots\\ \vdots & \vdots & \ddots\end{pmatrix}\frac{\Delta t}{2}\right]\begin{pmatrix}\Phi_1(r,R,0)\\ \Phi_2(r,R,0)\\ \vdots\end{pmatrix} \quad (100)$$

In Eq. (100), terms of order than $(\Delta t)^3$ and higher involve commutators of $\hat{T}$ and $\hat{V}$. These terms can be neglected provided that the time step Δt is sufficiently small. The SOA is described in detail in Leforestier et al. [92] Wave packet propagation using the SOA has been demonstrated by Alvarellos and Metiu.[93]

Each exponential function in Eq. (100) is easily evaluated by moving into the representation where each operator is diagonal. An exponential function with a matrix argument must be expanded in a Taylor series to evaluate it. If the matrix is diagonal this Taylor series simply yields a new diagonal matrix where the values of each element are

the exponentiated values of the corresponding value of the original matrix. This is illustrated in Eq. (101).

$$exp\begin{pmatrix} A_1 & 0 & 0 \\ 0 & A_2 & 0 \\ 0 & 0 & A_3 \end{pmatrix} = \begin{pmatrix} e^{A_1} & 0 & 0 \\ 0 & e^{A_2} & 0 \\ 0 & 0 & e^{A_3} \end{pmatrix} \qquad (101)$$

The kinetic energy operators in Eq. (98) are diagonal in the asymptotic representation. A Fourier transform changes the kinetic energy operators for the coordinate representation into the momentum representation, replacing the derivative operators $-\nabla^2$ with numbers κ^2. This simplifies the evaluation of the exponential function by multiplying momenta rather than differentiating with respect to nuclear coordinates.

The exponential functions containing the effective potential energy term can also be transformed in a similar way. It is possible to define a unitary transformation $\mathbb{U}$ for each (r, R) point that diagonalizes the effective potential energy. Using this spatially dependent transformation matrix $\mathbb{U}(r, R)$, the effective potential $\mathbf{V}^{\mathbf{D}}_{eff}$, Eq. (97), transform as follows

$$\begin{aligned} \mathbb{U}^{\dagger}(r,R)\mathbf{V}^{\mathbf{D}}_{eff}\boldsymbol{\Phi}^{\boldsymbol{D}} &= \mathbb{U}^{\dagger}(r,R)\mathbf{V}^{\mathbf{D}}_{eff}\mathbb{U}(r,R)\mathbb{U}^{\dagger}(r,R)\boldsymbol{\Phi}^{\boldsymbol{D}} \\ &= \mathbf{V}^{\mathbf{A}}_{eff}\boldsymbol{\Phi} \end{aligned} \qquad (102)$$

Once the effective potential has been transformed, Eq. (101) can be used to evaluate the exponential.

The time evolution of the reduced wave functions under the SOA is given by

$$\boldsymbol{\Phi}^{\boldsymbol{D}}(r,R,\Delta t) = \mathbb{U}\mathbb{U}^{\dagger}\boldsymbol{e}^{-i\widehat{V}\Delta t/2}\mathbb{U}\mathbb{U}^{\dagger}\mathcal{F}^{-1}\mathcal{F}\boldsymbol{e}^{-i\widehat{T}\Delta t}\mathcal{F}^{-1}\mathcal{F}\mathbb{U}\mathbb{U}^{\dagger}\boldsymbol{e}^{-i\widehat{V}\Delta t/2}\mathbb{U}\mathbb{U}^{\dagger}\boldsymbol{\Phi}^{\mathbf{D}}(r,R,0) \qquad (103)$$

Eq. (103) describes each processing step as $\boldsymbol{\Phi}^{\mathbf{D}}(r, R, 0)$ becomes $\boldsymbol{\Phi}^{\boldsymbol{D}}(r, R, \Delta t)$. First, the wave packet and exponential operator $\boldsymbol{e}^{-i\widehat{V}\Delta t/2}$ are transformed to the adiabatic basis and then multiplied. The result of this operation is first transformed back to the diabatic

representation and then Fourier transformed to the momentum representation. A two dimensional Fourier transform used to transform both radial and vibrational kinetic energies, Eqs. (62) and (64). The exponential operator $\boldsymbol{e^{-i\hat{T}\Delta t}}$ is diagonalized by this transformation. An inverse Fourier transform returns the result of this multiplication back to the coordinate representation. Here again the wave packet and exponential operator $\boldsymbol{e^{-i\hat{V}\Delta t/2}}$ are transformed to the adiabatic basis and then multiplied. Finally, the result is transformed back into the diabatic representation yielding the time evolved wave packet $\boldsymbol{\Phi^D}(r, R, \Delta t)$.

Introduction to the Scattering Problem

By using the propagation scheme described by Eq. (100), an initial wave packet can be propagated under the influence of the effective potential, Eq. (97). In this way the nonadiabatic effects captured in the full Hamiltonian are incorporated into the wave packet dynamics. Information about the system can be extracted from these evolved wave packets. This work focuses on calculating scattering matrix (S-matrix) elements. S-matrix elements are used to calculate the probability of state transitions due to an interaction. The method of calculating S-matrix elements from the propagation of wave packets falls within the framework of the CPM. Before discussing the details of the CPM, a very brief introduction to scattering theory is given. All of the scattering theory presented here is discussed in more detail in Taylor.[94]

In atomic/molecular scattering experiments the interaction between reactants takes place within a region no larger than several atomic diameters and on very short time-scales. Although new ultra-fast spectroscopic techniques are beginning to probe

these small time-scales, nearly all of what happens within the interaction region is unobservable. The fundamental goal of a scattering problem is to relate the state of a system's reactants well before the scattering event to the state of a system's products well after the interaction. By doing so, the initial state can be related to the possible experimental outcomes when the final state is measured.

Figure 7 depicts a wave function as it propagates through the interaction region (shown as a grey box).

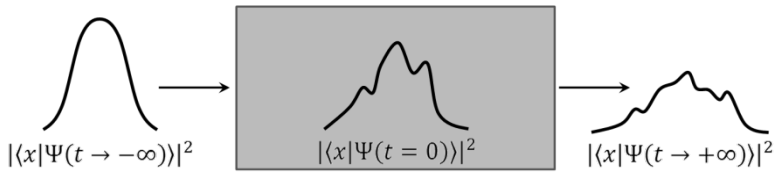

Figure 7. A visualization of a wave packet as it scatters off of the interaction region

The time $t \to -\infty$ refers to a time before the interaction when the wave packet is spatially separated from the interaction region (has no significant probability amplitude in the region). The time $t \to +\infty$ refers to a time after the interaction when the wave packet has left the interaction region. Both of these regions are referred to as the asymptotic limit. In the asymptotic limit the wave packet evolves under the influence of the asymptotic Hamiltonian denoted by $\widehat{H}_0$. The asymptotic Hamiltonian is the limit of the full Hamiltonian when the wave packet is spatially separated from the interaction. By the time the wave packet enters the shaded interaction region of Figure 7 the full Hamiltonian $\widehat{H}$ has lost its asymptotic character. The choice of the time origin $t = 0$ is arbitrary. A common choice places the wave packet well within the interaction region at $t = 0$. The

wave packet continues to evolve as it exits the interaction region. As the wave packet is spatially separated from the interaction region the full Hamiltonian again regains its asymptotic character. At some time well after the wave packet has exited the interaction region ($t \to +\infty$) it is compared with a product state wave packet.

Figure 7 depicts a single channel scattering event—a single input wave packet scattering into a single output packet. The B + H_2 system has many different channels. The number of channels available is determined by the value of j_{max}. For instance, if $j_{max} = 0$ then there are two possible channels to consider: $\left| \begin{matrix} 0 & 1/2 \\ 0 & 1/2 \end{matrix} \right\rangle$ and $\left| \begin{matrix} 0 & 3/2 \\ 0 & 1/2 \end{matrix} \right\rangle$. Figure 8 depicts a two channel scattering event where the incoming wave packet is defined in a single channel.

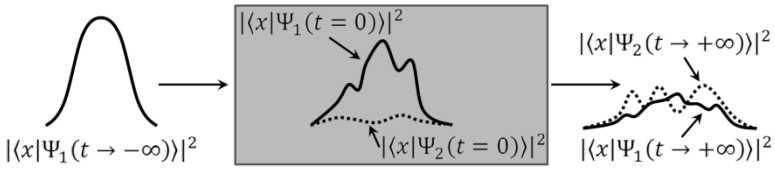

Figure 8. A visualization of a two channel scattering event

As the wave packet enters the interaction region, the probability amplitude of the wave packet is redistributed among both channels as time progresses. Both wave packets will continue to propagate giving a detector a chance of measuring an outcome for either channel. For $j_{max} = 6$ there are 20 different channels (when no vibrational transition occurs, $v = v'$) each labeled by a different set of quantum numbers contained in ζ

(Eq. (57)). The wave packets shown in Figure 7 and Figure 8 are one-dimensional. The B + H_2 system has two dimensional wave packets. The dimensions correspond to the Jacobi coordinates R and r.

The reactant states of the B + H_2 system are defined by forming a superposition of eigenstates of the asymptotic Hamiltonian (Eq. (58)). The reactant state can be specified; however, the product state is a result of the scattering event. The reactant and product states are defined as

$$\begin{aligned} |\Psi_{\text{react}}\rangle &= |\Psi(\text{t} \to -\infty)\rangle \\ |\Psi_{\text{prod}}\rangle &= |\Psi(\text{t} \to +\infty)\rangle \end{aligned} \qquad (104)$$

The TDSE, Eq. (98), prescribes how to propagate this wave packet in time. In Eq. (99), the operator $e^{-i\hat{H}\Delta t}$ is called the time evolution operator (TEO). As shown in Eq. (99) the TEO propagates a wave function defined at $t = 0$ to a time $t = \Delta t$. The TEO is used to propagate the reactant state through the interaction region. The reactant state will eventually evolve into the product state.

The reactant wave packet is defined as a superposition of plane waves labeled by κ within a given channel defined by ζ and ν given by Eq. (105).

$$\begin{aligned} \left|\Phi^{\zeta}_{\text{react}}\right\rangle &= \int d\kappa^{\zeta} \left|\zeta, \nu^{\zeta}, \kappa^{\zeta}\right\rangle \left\langle \zeta, \nu^{\zeta}, \kappa^{\zeta} \middle| \Phi^{\zeta}_{\text{react}} \right\rangle \\ &= \int d\kappa^{\zeta} \eta^{\zeta}(\kappa^{\zeta}) \left|\zeta, \nu^{\zeta}, \kappa^{\zeta}\right\rangle \end{aligned} \qquad (105)$$

The expansion coefficients of this superposition of plane waves are given by $\eta^{\gamma}(\kappa^{\zeta}) = \left\langle \zeta, \nu^{\zeta}, \kappa^{\zeta} \middle| \Phi^{\zeta}_{\text{react}} \right\rangle$.

The discussion of scattering in Taylor[94] defines an initial wave packet $|\Phi_{\text{in}}\rangle$ at $t = 0$ that when propagated to the asymptotic limit using the asymptotic Hamiltonian produces the reactant state of system $|\Psi(t \to -\infty)\rangle$. In the asymptotic region $|\Phi_{\text{in}}(t \to -\infty)\rangle = |\Psi(t \to -\infty)\rangle$. Choosing an initial wave packet already localized in the asymptotic region eliminates this step. The TEO is then used to propagate $|\Phi_{\text{in}}(t \to -\infty)\rangle$ forward in time under the influence of the full Hamiltonian to create the actual state of the system during the interaction $|\Psi(t = 0)\rangle$. This process is depicted in Figure 9.

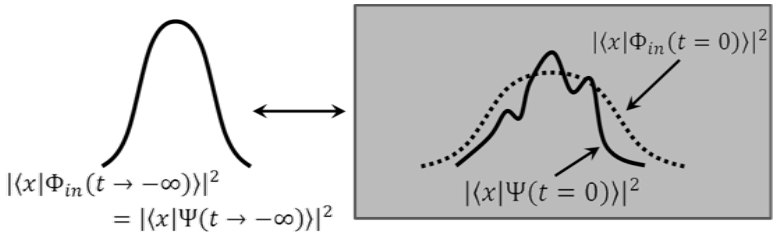

Figure 9. A depiction of how the actual state of the system $|\Psi(t = 0)\rangle$ is mapped to $|\Phi_{\text{in}}\rangle$

When grouped together, the TEOs that accomplish the propagations depicted in Figure 9 are called Møller operators. The TEO are given separately by Eqs. (106) and (107).

$$\hat{U}_0(t) = e^{-i\hat{H}_0 t} \qquad (106)$$

Eq. (106) represents the TEO under the asymptotic Hamiltonian. The TEO under the full Hamiltonian is given by Eq. (107).

$$\hat{U}(t) = e^{-i\hat{H}t} \qquad (107)$$

Using Eqs. (106) and (107) the Møller operators are defined as follows.

$$\Omega_{\pm} = \lim_{t \to \mp\infty} \hat{U}^{\dagger}(t)\, \hat{U}_0(t) \qquad (108)$$

The Møller operator that maps $|\Phi_{\text{in}}\rangle$ to $|\Psi(\text{t} = 0)\rangle$ is Ω_{+}. The sign in the subscript of the Møller operator is opposite the sign in the limit. The Hermitian conjugate of the full Hamiltonian TEO is used to ensure that it propagates in the opposite time direction as the asymptotic Hamiltonian TEO. The state resulting from the operation of Ω_{+} on $|\Phi_{\text{in}}\rangle$ is called the Møller state $|\Phi_{+}\rangle$.

$$|\Phi_{+}\rangle = \Omega_{+}|\Phi_{\text{in}}\rangle \qquad (109)$$

The Møller state $|\Phi_{+}\rangle$ represents $|\Psi(\text{t} = 0)\rangle$, the actual state of the system at $\text{t} = 0$.

Now the Møller state must be propagated forward in time to the asymptotic limit to determine the final state of the system $|\Psi(\text{t} \to +\infty)\rangle$ which is the product state $|\Psi_{\text{prod}}\rangle$. This final state $|\Psi(\text{t} \to +\infty)\rangle$ must also be mapped to a wave function defined at $\text{t} = 0$. Both of these steps are done by applying the Møller operator $\Omega_{-}^{\dagger}$ on the state $|\Phi_{+}\rangle$ to give $|\Phi_{\text{out}}\rangle$. The state $|\Phi_{\text{out}}\rangle$ is the state defined at $\text{t} = 0$ that when propagated forward in time under the asymptotic Hamiltonian becomes the product state.

Eq. (110) shows how the Hermitian conjugate of the Møller operator Ω_{-} switches the order of propagation.

$$\begin{aligned} \Omega_{-}^{\dagger} &= \left\{ \lim_{t \to +\infty} \hat{U}^{\dagger}(t)\, \hat{U}_0(t) \right\}^{\dagger} \\ &= \lim_{t \to +\infty} \hat{U}_0^{\dagger}(t) \hat{U}(t) \end{aligned} \qquad (110)$$

Now the wave packet is propagated forward in time under the full Hamiltonian and then propagated backward in time using the asymptotic Hamiltonian. Thus the Møller operator $\Omega_{-}^{\dagger}$ maps $|\Phi_{+}\rangle$ onto $|\Phi_{\text{out}}\rangle$. Figure 10 depicts how this happens for $|\Phi_{\text{out}}\rangle$. The states $|\Phi_{\text{in,out}}\rangle$ represent wave functions that when propagated to their respective

asymptotic limits map onto the asymptotic wave function of the actual state of the system $|\Psi(t \to \pm\infty)\rangle$. These states are often referred to as the 'in' or 'out' asymptote.

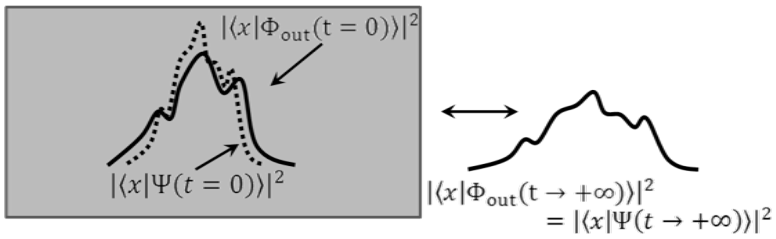

Figure 10. A depiction of how the actual state of the system $|\Psi(t=0)\rangle$ is mapped to $|\Phi_{out}\rangle$

The scattering operator $\hat{S}$ is constructed by combining both Møller operators.

$$\begin{aligned} |\Phi_{out}\rangle &= \Omega_{-}^{\dagger}\Omega_{+}|\Phi_{in}\rangle \\ &= \hat{S}|\Phi_{in}\rangle \end{aligned} \qquad (111)$$

The scattering operator $\hat{S}$ maps the 'in' asymptote $|\Phi_{in}\rangle$ to the 'out' asymptote $|\Phi_{out}\rangle$. Eq. (111) can be used to calculate the probability of measuring an outcome of a scattering event. This probability is expressed as

$$\begin{aligned} P &= \left|\langle\Phi_m|\hat{S}|\Phi_{in}\rangle\right|^2 \\ &= |\langle\Phi_m|\Phi_{out}\rangle|^2 \\ &= |\langle\Phi_-|\Phi_+\rangle|^2 \end{aligned} \qquad (112)$$

In Eq. (112), the state $|\Phi_m\rangle$ is the experimental outcome state. It is chosen from the set of eiegnfunctions of a Hermitian operator (an observable). For example, if an experiment measured the total energy of the final state after the interaction, the state $|\Phi_m\rangle$ would be chosen from the eigenfunctions of the Hamiltonian operator. The initial state $|\Phi_{in}\rangle$ and the measurement state $|\Phi_m\rangle$ can also be chosen as an eiegenstate of the asymptotic

Hamiltonian. This would give the probability of system starting in the state $|\Phi_{\text{in}}\rangle$ being measured in the state $|\Phi_{\text{m}}\rangle$ after the interaction.

The Time-Dependent Channel Packet Method

In the time-dependent CPM, reactant states (the channel packets) are chosen and propagated using TEOs.[43, 44] These evolved wave packets are then compared to measurement wave packets defined in many channels to calculate probabilities using Eq. (112). The basis functions given by Eqs. (94) and (95) define the input and output channels of the scattering problem for the B + H_2 scattering problem. Wave packets are created within these channels.

The asymptotic Hamiltonian for the B + H_2 system can be broken into three pieces (Eqs. (53), (54), and (55)). When considering the energy of the scattering experiment, it is useful to express the asymptotic Hamiltonian (Eq. (46)) as

$$\begin{aligned}\widehat{H}_0 &= \widehat{H}_0^{trns} + \widehat{H}_0^{rot} + \widehat{H}_0^{\text{vib}} \\ &= \widehat{H}_0^{trns} + \widehat{H}_{\text{int}}\end{aligned} \qquad (113)$$

Eq. (113) groups the angular moment/spin-orbit and vibrational Hamiltonians as the internal Hamiltonian $\widehat{H}_{\text{int}}$. The $\widehat{H}_{\text{int}}$ component describes the internal rotational and vibrational dynamics of H_2 and the spin-orbit coupling of the boron atom. The eigenstates of $\widehat{H}_{\text{int}}$ are the asymptotic eigenstates described by Eq. (57). The eigenstates of $\widehat{H}_0^{trns}$ are plane waves labeled by the corresponding momentum κ. In the coordinate representation $|\kappa\rangle$ is expressed as

$$\langle R|\kappa\rangle = \frac{1}{\sqrt{2\pi}} e^{i\kappa R} \qquad (114)$$

A superposition of plane waves is required to form a normalizable wave function. In conjunction with the reduced wave function used in Eq. (98), the definition of the reduced momentum operator $\hat{p}_R$ in both the momentum and coordinate representations is given as (in atomic units)

$$\begin{aligned} \hat{p}_R &\leftrightarrow k_R^{\gamma} \text{ (momentum)} \\ \hat{p}_R &\leftrightarrow -i\frac{\partial}{\partial R} \text{ (coordinate)} \end{aligned} \qquad (115)$$

The action of the asymptotic Hamiltonian can then be expressed as

$$\begin{aligned} \widehat{H}_0\left|\zeta, v^{\zeta}, \kappa^{\zeta}\right\rangle &= \left(\widehat{H}_0^{k} + \widehat{H}_{\text{int}}\right)\left|\zeta, v^{\zeta}, \kappa^{\zeta}\right\rangle \\ &= \left(E_{\kappa}^{\zeta} + E_{\text{int}}^{\zeta}\right)\left|\zeta, v^{\zeta}, \kappa^{\zeta}\right\rangle \end{aligned} \qquad (116)$$

where E_{int}^{ζ} is the energy eigenvalue associated with $\widehat{H}_{\text{int}}$. The energy eigenvalue associated with $\widehat{H}_0^{\kappa}$ is E_{κ}^{ζ}. The label ζ is retained on the eigenvalue because it is associated with a specific channel given by $\left|\zeta, v^{\zeta}, \kappa^{\zeta}\right\rangle$

When vibrational transitions are permitted, the label v^{ζ} creates manifolds within the channel ζ, thus multiplying the size of the basis by the number of vibrational transitions considered. This work will restrict H_2 to the ground vibrational state ($v^{\zeta} = v^{\zeta'} = 0$). However, the theory developed thus far is general enough to accommodate the calculation of transitions to higher order vibrational modes. In these cases the label ζ designates a channel and v^{ζ} designates a manifold within the channel. There is a risk of entering the energy regime where boron and H_2 react to form BH_2 when modeling higher order vibrational transitions. Modeling the reaction requires additional potential energy surfaces not considered in this work.

Each plane wave component is associated with an energy given in atomic units by

$$E = E_{\text{int}}^{\zeta} + \frac{\left|\kappa^{\zeta}\right|^2}{2\mu_{B,H_2}}$$
$$\left|\kappa^{\zeta}\right| = \left\{2\mu_{B,H_2}\left(E - E_{\text{int}}^{\zeta}\right)\right\}^{1/2} \qquad (117)$$

Forming a superposition of plane waves serves two purposes: it creates a normalizable wave packet, and allows the calculation of scattering probabilities as a function of energy. The initial and outcome wave packets $\left|\Phi_{\text{in,m}}^{\zeta}\right\rangle$ are constructed by forming a linear combination of plane waves. Using eigenfuntions defined at $t = 0$ this superposition can be expressed as

$$\begin{aligned}\left|\Phi_{\text{in,m}}^{\zeta}\right\rangle &= \int d\kappa^{\zeta}\left|\zeta, \nu^{\zeta}, \kappa^{\zeta}\right\rangle\left\langle\zeta, \nu^{\zeta}, \kappa^{\zeta}\right|\left.\Phi_{\text{in,m}}^{\zeta}\right\rangle \\ &= \int d\kappa^{\zeta}\eta_{\pm}^{\zeta}(\kappa^{\zeta})\left|\zeta, \nu^{\zeta}, \kappa^{\zeta}\right\rangle \\ &= \int dE_{\kappa}^{\zeta}\eta_{\pm}^{\zeta}\left(E_{\kappa}^{\zeta}\right)\left|\zeta, \nu^{\zeta}, E_{\kappa}^{\zeta}\right\rangle\end{aligned} \qquad (118)$$

where

$$\left|\zeta, \nu^{\zeta}, E_{\kappa}^{\zeta}\right\rangle = \left(\frac{\mu_{B,H_2}}{\left|\kappa^{\zeta}\right|}\right)^{\frac{1}{2}}\left|\zeta, \nu^{\zeta}, \kappa^{\zeta}\right\rangle \qquad (119)$$

and

$$\begin{aligned}\eta_{\pm}^{\zeta}(\kappa^{\zeta}) &= \left\langle\zeta, \nu^{\zeta}, \kappa^{\zeta}\right|\left.\Phi_{\text{in,m}}^{\zeta}\right\rangle \\ \eta_{\pm}^{\zeta}\left(E_{\kappa}^{\zeta}\right) &= \left\langle\zeta, \nu^{\zeta}, E_{\kappa}^{\zeta}\right|\left.\Phi_{\text{in,m}}^{\zeta}\right\rangle \\ \eta_{\pm}^{\zeta}\left(E_{\kappa}^{\zeta}\right) &= \left(\frac{\mu_{B,H_2}}{\left|\kappa^{\zeta}\right|}\right)^{\frac{1}{2}}\eta_{\pm}^{\zeta}(\kappa^{\zeta})\end{aligned} \qquad (120)$$

Eq. (118) expresses the superposition as a function of the wave number κ^{ζ} and the energy E_{κ}^{ζ}. Eqs. (119) and (120) give the relationships needed to perform this transformation. Here the label ζ has been retained in the superscript for $\left|\Phi_{\text{in,m}}^{\zeta}\right\rangle$ indicating that the wave packet is defined in a specific channel. The expansion

coefficients in Eq. (120) are chosen so that $\eta_{+}^{\zeta}(\kappa^{\zeta})$ corresponds to $|\Phi_{\text{in}}^{\zeta}\rangle$ and $\eta_{-}^{\zeta}(\kappa^{\zeta})$ corresponds to $|\Phi_{\text{m}}^{\zeta}\rangle$. The coefficients $\eta_{\pm}^{\zeta}(\kappa^{\zeta})$ are generally chosen to give a Gaussian function in the coordinate representation.

Once these states have been constructed, they can be propagated using the Møller operators. Theoretically the propagation must be done over an infinite time interval; however, for computational purposes the wave packets must be created in and propagated well into the regime of the asymptotic Hamiltonian. For the B + H_2 system, this occurs as the electrostatic interaction potential approaches zero. Once propagated, Eq. (112) can be used to calculate the probability. However, this is not the probability of a single eigenstate scattering into a different eigenstate. The states $|\Phi_{\text{in,m}}^{\zeta}\rangle$ are formed from a superposition of eigenstates of the asymptotic Hamiltonian. It is possible to extract energy (momentum) resolved S-matrix elements—the probability of a well-defined energy state transitioning to another well-defined energy state.

Energy Resolved S-matrix Elements

The eigenstates of the translation operator (Eq. (114)) are not proper wave functions since they cannot be normalized. As a result, a superposition of these states was formed to create a normalizable wave packet. The wave packet itself is not an eigenstate of the asymptotic Hamiltonian and does not have a well defined energy. In this section the method for extracting energy (momentum) resolved S-matrix elements is derived. The discussion in this section is motivated by the derivation of energy resolved S-matrix elements performed by Tannor and Weeks 1993.[42]

The derivation begins by examining the different propagation steps contained in the scattering matrix operator in the term $\left\langle \Phi_{\mathrm{m}}^{\zeta'} \middle| \hat{S} \middle| \Phi_{\mathrm{in}}^{\zeta} \right\rangle$ found in Eq. (112). The superscripts ζ and ζ' serve as a reminder that the initial state and the measurement state can be defined in different reactant/product channels. These superscripts will be omitted to simplify the notation. To simplify the notation further $|\Phi_\alpha\rangle$ will represent $\left|\Phi_{\mathrm{in}}^{\zeta}\right\rangle$ and $\left|\Phi_\beta\right\rangle$ will represent $\left|\Phi_{\mathrm{m}}^{\zeta'}\right\rangle$.

$$
\begin{aligned}
\langle \Phi_\beta | \hat{S} | \Phi_\alpha \rangle &= \langle \Phi_\beta | \Omega_-^\dagger \Omega_+ | \Phi_\alpha \rangle \\
&= \langle \Phi_\beta | \Omega_-^\dagger \Omega_+ | \Phi_\alpha \rangle \\
&= \left\langle \Phi_\beta \middle| \left\{ \lim_{t' \to +\infty} \hat{U}_0^\dagger(t') \hat{U}(t') \right\} \left\{ \lim_{t \to -\infty} \hat{U}^\dagger(t)\, \hat{U}_0(t) \right\} \middle| \Phi_\alpha \right\rangle \\
&= \left\langle \Phi_\beta(t \to +\infty) \middle| \left\{ \lim_{t' \to +\infty} \hat{U}(t') \right\} \left\{ \lim_{t \to -\infty} \hat{U}^\dagger(t) \right\} \middle| \Phi_\alpha(t \to -\infty) \right\rangle \\
&= \left\langle \Phi_\beta(t \to +\infty) \middle| \left\{ \lim_{\substack{t' \to +\infty \\ t \to -\infty}} e^{-i\hat{H}(t'-t)} \right\} \middle| \Phi_\alpha(t \to -\infty) \right\rangle
\end{aligned}
\qquad (121)
$$

Eq. (121) shows how the different propagation steps of the Møller operators can be separated and used to propagate the wave packets $|\Phi_\alpha\rangle$ and $\left|\Phi_\beta\right\rangle$ to their respective asymptotic limits. The remaining TEOs can be consolidated. The limits on t and t' create a positive time interval, the propagation time t_p. The propagation time is given by

$$
t_p = t' - t \qquad (122)
$$

With this new definition of time, Eq. (121) can be written as

$$
\begin{aligned}
\langle \Phi_\beta | \hat{S} | \Phi_\alpha \rangle &= \lim_{t_p \to +\infty} \langle \Phi_\beta(t \to +\infty) | e^{-i\hat{H}t_p} | \Phi_\alpha(t \to -\infty) \rangle \\
&= \lim_{t_p \to +\infty} C_{\zeta'\zeta}(t_p)
\end{aligned}
\qquad (123)
$$

where the time-dependent correlation function $C_{\zeta'\zeta}(t_p)$ is defined as

$$C_{\zeta'\zeta}(t_p) = \langle \Phi_\beta(t \to +\infty) | e^{-i\hat{H}t_p} | \Phi_\alpha(t \to -\infty) \rangle \quad (124)$$

The correlation function $C_{\zeta'\zeta}(t_p)$ captures the overlap between the measurement state $|\Phi_\beta(t \to +\infty)\rangle$ and the evolving reactant state $|\Phi^{\zeta}_{\text{react}}\rangle = |\Phi_\alpha(t \to -\infty)\rangle$ as a function of time. When the limit as the propagation time $t_p \to +\infty$ is taken, the result is the S-matrix element $\langle \Phi_\beta | \hat{S} | \Phi_\alpha \rangle$.

The derivation proceeds by taking the Fourier transform of both sides of Eq. (121) arriving at the following expression

$$\lim_{t_p \to +\infty} \int_0^{t_p} dt_p' \langle \Phi_\beta | \hat{S} | \Phi_\alpha \rangle e^{i\bar{E}t_p'} = \lim_{t_p \to +\infty} \int_0^{t_p} dt_p' C_{\zeta'\zeta}(t_p') e^{i\bar{E}t_p'} \quad (125)$$

The time origin is chosen so that the propagation of $|\Phi_\alpha(t \to -\infty)\rangle$ begins at $t_p = 0$. However, the limits of integration can be extended to earlier times since there is no significant overlap between $|\Phi_\beta(t \to +\infty)\rangle$ and the evolving reactant state $|\Phi_\alpha(t \to -\infty)\rangle$ for times earlier than $t_p = 0$. Thus, Eq. (125) can be cast into a form easily recognized as a Fourier transform.

$$\begin{aligned} \lim_{t_p \to +\infty} \int_{-t_p}^{t_p} dt_p' \langle \Phi_\beta | \hat{S} | \Phi_\alpha \rangle e^{i\bar{E}t_p'} &= \lim_{t_p \to +\infty} \int_{-t_p}^{t_p} dt_p' C_{\zeta'\zeta}(t_p') e^{i\bar{E}t_p'} \\ \int_{-\infty}^{+\infty} dt_p' \langle \Phi_\beta | \hat{S} | \Phi_\alpha \rangle e^{i\bar{E}t_p'} &= \int_{-\infty}^{+\infty} dt_p' C_{\zeta'\zeta}(t_p') e^{i\bar{E}t_p'} \end{aligned} \quad (126)$$

The right-hand side of Eq. (126) is the Fourier transform of the correlation function. This can be computed numerically by propagating the reactant wave packet using the TEO $e^{-i\hat{H}t_p}$, calculating the correlation function $C_{\zeta'\zeta}(t_p)$ for each value of t_p, and then

taking the finite Fourier transform of the resulting array of points. The right-hand side of Eq. (126) can be manipulated further to reveal energy-resolved S-matrix elements.

This is done by first expressing $\langle \Phi_\beta | \hat{S} | \Phi_\alpha \rangle$ in terms of the asymptotic eigenstates by using completeness relationships.

$$\langle \Phi_\beta | \hat{S} | \Phi_\alpha \rangle = \sum_{\alpha', \beta', \nu^{\alpha'}, \nu^{\beta'}} \int_0^\infty dE_\kappa^{\beta'} \int_0^\infty dE_\kappa^{\alpha'} \left\langle \Phi_\beta \middle| \beta', \nu^{\beta'}, E_\kappa^{\beta'} \right\rangle \left\langle \beta', \nu^{\beta'}, E_\kappa^{\beta'} \middle| \hat{S} \middle| \alpha', \nu^{\alpha'}, E_\kappa^{\alpha'} \right\rangle \times \langle \alpha', \nu^{\alpha'}, E_\kappa^{\alpha'} | \Phi_\alpha \rangle \quad (127)$$

The term $\left\langle \beta', \nu^{\beta'}, E_\kappa^{\beta'} \middle| \hat{S} \middle| \alpha', \nu^{\alpha'}, E_\kappa^{\alpha'} \right\rangle$ is the energy-resolved S-matrix element. The terms $\langle \alpha', \nu^{\alpha'}, E_\kappa^{\alpha'} | \Phi_\alpha \rangle$ in Eq. (127) can be express as follow by using the definition given by Eq. (118).

$$\begin{aligned} \langle \alpha', \nu^{\alpha'}, E_\kappa^{\alpha'} | \Phi_\alpha \rangle &= \int_0^\infty dE_\kappa^\alpha \eta_-^\alpha (E_\kappa^\alpha) \langle \alpha', \nu^{\alpha'}, E_\kappa^{\alpha'} | \alpha, \nu^\alpha, E_\kappa^\alpha \rangle \\ &= \int_0^\infty dE_\kappa^\alpha \eta_-^\alpha (E_\kappa^\alpha) \delta_{\alpha'\alpha} \delta_{\nu^{\alpha'}\nu^\alpha} \delta(E_\kappa^{\alpha'} - E_\kappa^\alpha) \\ &= \eta_-^\alpha (E_\kappa^\alpha) \delta_{\alpha'\alpha} \delta_{\nu^{\alpha'}\nu^\alpha} \end{aligned} \quad (128)$$

In a similar fashion, the term $\left\langle \Phi_\beta(t \to +\infty) \middle| \beta', \nu^{\beta'}, E_\kappa^{\beta'} \right\rangle$ can be written

$$\left\langle \Phi_\beta(t' \to +\infty) \middle| \beta', \nu^{\beta'}, E_\kappa^{\beta'} \right\rangle = \eta_+^\beta \left(E_\kappa^\beta \right) \delta_{\beta'\beta} \delta_{\nu^{\beta'}\nu^\beta} \quad (129)$$

When Eqs. (128) and (129) are inserted into Eq. (127) the following expression is obtained.

$$\langle \Phi_\beta | \hat{S} | \Phi_\alpha \rangle = \int_0^\infty dE_\kappa^{\beta'} \int_0^\infty dE_\kappa^{\alpha'} \eta_+^\beta \left(E_\kappa^{\beta'} \right) \eta_-^\alpha (E_\kappa^{\alpha'}) \left\langle \beta', \nu^{\beta'}, E_\kappa^{\beta'} \middle| \hat{S} \middle| \alpha', \nu^{\alpha'}, E_\kappa^{\alpha'} \right\rangle \quad (130)$$

Eq. (130) is inserted in the right-hand expression of Eq. (126) to yield

$$\int_{-\infty}^{+\infty} dt_p' \langle \Phi_\beta | \hat{S} | \Phi_\alpha \rangle e^{i\bar{E}t_p'}$$
$$= \int_{-\infty}^{+\infty} dt_p' \int_0^{\infty} dE_\kappa^{\beta'} \int_0^{\infty} dE_\kappa^{\alpha'} \eta_+^\beta \left(E_\kappa^{\beta'}\right) \eta_-^\alpha (E_\kappa^{\alpha'}) \left\langle \beta', \nu^{\beta'}, E_\kappa^{\beta'} \middle| \hat{S} \middle| \alpha', \nu^{\alpha'}, E_\kappa^{\alpha'} \right\rangle e^{i\bar{E}t_p'} \quad (131)$$

The term $\bar{E}$ can be defined in the following way

$$\bar{E} = E'' - E_\kappa^{\alpha'} \quad (132)$$

where E'' is a constant energy offset. The integral over time now leads to a delta function as shown in Eq. (133).

$$\int_0^{\infty} dE_\kappa^{\beta'} \int_0^{\infty} dE_\kappa^{\alpha'} \eta_+^\beta \left(E_\kappa^{\beta'}\right) \eta_-^\alpha \left(E_\kappa^{\alpha'}\right) \left\langle \beta', \nu^{\beta'}, E_\kappa^{\beta'} \middle| \hat{S} \middle| \alpha', \nu^{\alpha'}, E_\kappa^{\alpha'} \right\rangle 2\pi\delta\left(E'' - E_\kappa^{\alpha'}\right) \quad (133)$$

The delta function $\delta\left(E'' - E_\kappa^{\alpha'}\right)$ leads to the following simplification.

$$\int_0^{\infty} dE_\kappa^{\beta'} \eta_+^\beta \left(E_\kappa^{\beta'}\right) \eta_-^\alpha (E'') \left\langle \beta', \nu^{\beta'}, E_\kappa^{\beta'} \middle| \hat{S} \middle| \alpha', \nu^{\alpha'}, E'' \right\rangle \quad (134)$$

Eq. (135) introduce the on-shell S-matrix element $S_{\alpha\beta}(E)$ defined as

$$S_{\alpha\beta}(E)\delta\left(E_\kappa^{\beta'} - E\right) = \left\langle \beta', \nu^{\beta'}, E_\kappa^{\beta'} \middle| \hat{S} \middle| \alpha', \nu^{\alpha'}, E \right\rangle \quad (135)$$

The on-shell S-matrix element allows for further simplification of Eq. (134). The right-hand term of Eq. (126) becomes

$$\int_{-\infty}^{+\infty} dt_p' \langle \Phi_\beta | \hat{S} | \Phi_\alpha \rangle e^{i\bar{E}t_p'} = 2\pi\eta_+^\beta(E)\eta_-^\alpha(E)S_{\alpha\beta}(E) \quad (136)$$

Further manipulation of Eq. (126) yields

$$S_{\alpha\beta}(E) = \frac{1}{2\pi\eta_+^\beta(E)\eta_-^\alpha(E)} \int_{-\infty}^{+\infty} dt_p' C_{\zeta'\zeta}\left(t_p'\right) e^{iEt_p'} \quad (137)$$

Eq. (137) can also be expressed in terms of momentum by using Eq. (120).

$$S^{\zeta'\zeta}_{\kappa^{\zeta'}\kappa^{\zeta}} = \frac{\left(\left|\kappa^{\zeta'}\right|\left|\kappa^{\zeta}\right|\right)^{1/2}}{2\pi\mu_{B,H_2}\eta_{+}^{\beta}\left(\kappa^{\zeta'}\right)\eta_{-}^{\alpha}\left(\kappa^{\zeta}\right)} \int_{-\infty}^{+\infty} dt'_p C_{\zeta'\zeta}\left(t'_p\right) e^{iEt'_p} \quad (138)$$

Energy and momentum resolved S-matrix elements can be calculated using Eqs. (137) and (138). Through Eq. (112) the probability of a reactant state being measured is a given product state can be calculated.

Energy resolved S-matrix elements calculated over a range of total angular momentum values can be used to calculate cross-sections and reaction rates. Cross-sections are given by

$$\sigma_{\zeta\to\zeta'}(E) = \frac{\pi}{(\kappa^{\zeta})^2}\sum_{J}(2J+1)\left|S_{\zeta,\zeta'}(E)\right|^2 \quad (139)$$

where κ^{ζ} is defined in Eq. (117). The total angular momentum J is contained within the state labels ζ and ζ' defining the asymptotic basis set. Reaction rates can be calculated using the following equation.

$$k_{\zeta\to\zeta'}(T) = \left(\frac{8k_BT}{\pi\mu_{B,H_2}}\right)(k_BT)^{-2}\int_{0}^{\infty} Ee^{\frac{-E}{k_BT}}\sigma_{\zeta\to\zeta'}(E)dE \quad (140)$$

This work restricts the total angular momentum to $J = 1/2$. Consequently cross-sections and reaction rates will not be calculated.

III. Results and Discussion

The Adiabatic Potential Energy Surface and Derivative Coupling Data Set

The $1\,^2A'$, $2\,^2A'$, and $1\,^2A''$ adiabatic PESs and DCTs used in this research were calculated by Dr. Dave Yarkony (Johns Hopkins University) using his suite of *ab initio* programs. The adiabatic PESs were calculated at the SA-MCSCF/CI level. The contracted basis set (13*s*8*p*3*d*)/[8*s*5*p*3*d*] was used for boron.[95, 96] The contracted basis set (8*s*3*p*1*d*)/[6*s*3*p*1*d*] was used for hydrogen.[97] This approach for the electronic structure calculation was used in previous work on the B + H_2 system and has been validated by experimental endoergicity measurements.[29, 45] Previous electronic structure calculations were carried out on a two dimensional grid given by Jacobi coordinates (R, θ); the coordinate r was fixed at the equilibrium value of the H_2 bond length.[26, 36, 37] The electronic structure calculation for this work was carried out for several values of the H_2 bond length making it possible to consider H_2 vibrational transitions in future work.

Adiabatic PESs and DCTs were calculated at points on a three dimensional grid given by Jacobi coordinates (r, θ, R). Each point on this grid represents a given spatial configuration of the B + H_2 nuclei. The values of R range from zero to 10 a.u. in steps of 0.2 a.u. for a total of 51 grid points in this coordinate. The values of θ range from zero to $\pi/2$ radians in steps of $\pi/20$ for a total of 11 grid points in this coordinate. The values of r include 0.7 a.u. and range from 0.904 a.u. to 4.402 a.u. in steps of 0.5 a.u. for a total of 9 grid points in this coordinate. The complete three-dimensional grid contains 5049 points. In Appendix F the three adiabatic PESs are plotted for the configurations with C_{2v} symmetry ($\theta = \pi/2$) and $D_{\infty h}$ symmetry ($\theta = 0$).

This grid is coarse in comparison to grids designed to characterize the topology of a conical intersection. Numerical grids in these studies are typically no larger than 1 au distance from a conical intersection.[72-76] The coarse grid introduces step-size error that enters into the line integral used to calculate the ADT mixing angle. It also tends to under sample the sharp features that exist near conical intersections. An example of this is shown in Figure 11.

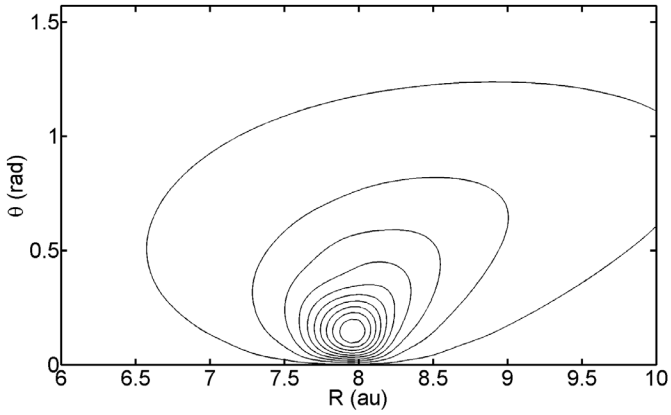

Figure 11. Contour plot of the derivative coupling component $\tau_R(R,\theta)$ for r = 0.7 au with contours starting at 0.1 au and spaced in 0.195 au increments

In Figure 11 the contours begin at 0.1 au and are spaced in increments of 0.195 au. The derivative coupling component τ_R rises to a sharp peak near the collinear configuration for $(r, R) = (0.7, 8.0)$ au. However, the peak appears to vanish for the collinear configuration ($\theta = 0$). A sharp peak does exist in the collinear configuration, but the grid does not have sufficient resolution to capture it.

The numerical grid for this work also has regions where the nuclei are in close proximity. The electronic structure calculation was not performed when two nuclei were

within a proximity threshold. The proximity threshold was set to 0.699 au for H–H distances and 1.17 au for H–B. An energy ceiling of 0.2707 au was established for these regions. These regions have no impact on the dynamics of the system for small energies.

Aside from these omissions, the raw data had other noticeable blemishes as shown in Figure 12.

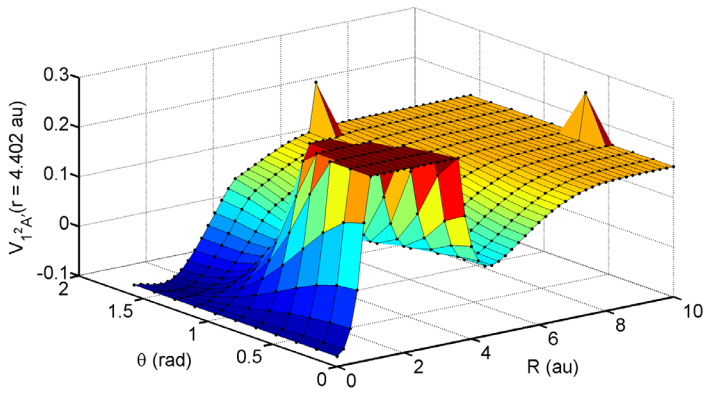

Figure 12. A slice of the $V_{1^2A'}$ adiabatic PES for $r = 1.402$ au adiabatic PES showing two noticeable outlying points

Figure 12 is a slice of the $V_{1^2A'}$ adiabatic PES surface for $r = 4.402$ au. In this slice there are two obvious outlying points. The figure also has a mesa-like structure where the proximity threshold of 0.2707 au was applied. It is not known how these points converged to these values, nor was it possible to recalculate the data at these points. The data for outlying points were interpolated using a low-order polynomial fitting function and compared with neighboring values to ensure continuity.

The raw DCT data also had numerical artifacts that were corrected. The DCTs were numerically determined to an arbitrary phase factor. Since the PESs and DCTs are

real valued, this phase factor resulted in an arbitrary sign being assigned to a value. The correction of this phase error is described by Belcher.[98] An attempt was made to identify outlying points in the phase-corrected NACT data. This was abandoned since it is difficult to distinguish an outlying point from the naturally sharp features that exist in the DCT data. In Appendix G a selection of DCT surfaces are presented.

The Cartesian-to-Jacobi Coordinate Transform

The electronic structure code required Cartesian coordinate inputs. In Cartesian coordinates, the B + H_2 system has 9 DOF; three Cartesian coordinates for each nuclei. These coordinates can be transformed to a new set of coordinates which consist of three coordinates for the CM, three Euler angles, and three internal coordinates. The internal DOF of are described by the Jacobi coordinates R, the distance between the boron atom and the hydrogen molecule CM; r, the bond length of the hydrogen molecule; and θ, the polar angle between the axis containing the boron atom and the axis containing the hydrogen atoms. This is shown in Figure 3.

In the absence of external fields the PESs and NACTs are not dependent on SF coordinates, and without loss of generality the B + H_2 system can be restricted to the SF xz plane. The orientation of the B + H_2 configuration in the plane is given by the BF internal coordinates, a single Euler angle, and the coordinates of the B + H_2 CM. Table 1 lists the Cartesian and SF/BF coordinates used.

Table 1. The Cartesian and SF/BF coordinates used to specify nuclear configurations for the electronic structure calculation

Cartesian Coordinates	SF/BF Coordinates
x_{H1}	r
y_{H1}	R
x_{H2}	θ
y_{H2}	x_{cm}
x_B	y_{cm}
y_B	ω

The relationship between these coordinates is illustrated in Figure 13.

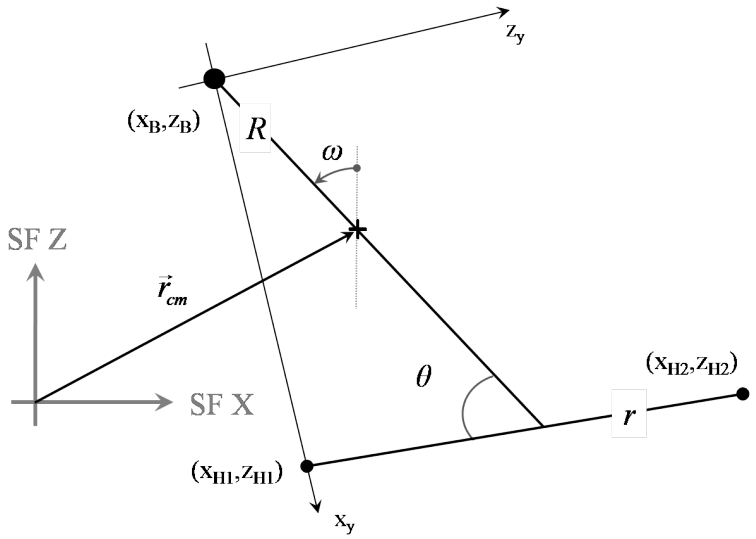

Figure 13. The geometrical relationship between Cartesian coordinates and Jacobi coordinates for the B + H_2 system

The B + H_2 system lies within the plane defined by the SF *X* and *Z* axes. The internal Jacobi coordinates *r, R,* and θ are the same described in Figure 3. The vector $\vec{r}_{cm}$ is given by the Cartesian components (x_{cm}, z_{cm}) and points to the CM of the B + H_2 system. The

CM has been displaced for clarity. The angle ω is the polar angle with respect to the SF Z axis. The transformation between these coordinates is given by the following equations:

$$
\begin{aligned}
r &= \{(x_{H2} - x_{H1})^2 + (z_{H2} - z_{H1})^2\}^{1/2} \\
R &= \left\{\left(\tfrac{1}{2}x_{H2} + \tfrac{1}{2}x_{H1} - x_B\right)^2 + \left(\tfrac{1}{2}z_{H2} + \tfrac{1}{2}z_{H1} - z_B\right)^2\right\}^{1/2} \\
\theta &= \cos^{-1}\left\{\frac{\left(\tfrac{1}{2}x_{H2} + \tfrac{1}{2}x_{H1} - x_B\right)(x_{H2} - x_{H1}) + \left(\tfrac{1}{2}z_{H2} + \tfrac{1}{2}z_{H1} - z_B\right)(z_{H2} - z_{H1})}{rR}\right\} \\
\omega &= \cos^{-1}\left\{\frac{\left(\tfrac{1}{2}x_{H2} + \tfrac{1}{2}x_{H1} - x_B\right)}{R}\right\} \\
x_{cm} &= \frac{1}{M}(m_B x_B + m_h x_{H1} + m_H x_{H2}) \\
z_{cm} &= \frac{1}{M}(m_B z_B + m_h z_{H1} + m_H z_{H2})
\end{aligned}
\qquad (141)
$$

The electronic structure calculation is invariant with respect to the location of the CM and the Euler angle ω. Hence, only three coordinates are required to specify the internal configuration of the B + H_2 system. The numerical calculation was simplified by defining a new set of coordinate axes shown in Figure 13 as x_y and x_y. The boron atom is located at the origin of the x_y and x_y axes. One of the hydrogen atoms is fixed on the x_y axis, while allowing the other hydrogen atom to move freely in the plane as internal coordinates changed.

The NACTs also had to be transformed from Cartesian coordinates to Jacobi coordinates. As defined in Eq. (21), the DCTs involve partial derivatives with respect to nuclear coordinates. This complicates the coordinate transformation. To obtain the NACTs as functions of internal Jacobi coordinates the Cartesian partial derivatives must be transformed to partial derivatives with respect to internal Jacobi coordinates. An example of this is given in Eq. (142) for the internal Jacobi coordinate R.

$$
\begin{aligned}
\tau_R^A &= \left\langle \phi_i^A \middle| \frac{\partial}{\partial R}\phi_j^A \right\rangle \\
&= \left\langle \phi_i^A \middle| \left\{\frac{\partial x_B}{\partial R}\frac{\partial}{\partial x_B} + \frac{\partial z_B}{\partial R}\frac{\partial}{\partial z_B} + \frac{\partial x_{H1}}{\partial R}\frac{\partial}{\partial x_{H1}} + \frac{\partial z_{H1}}{\partial R}\frac{\partial}{\partial z_{H1}} + \frac{\partial x_{H2}}{\partial R}\frac{\partial}{\partial x_{H2}} + \frac{\partial z_{H2}}{\partial R}\frac{\partial}{\partial z_{H2}}\right\} \phi_j^A \right\rangle
\end{aligned}
\qquad (142)
$$

Eq. (142) uses the chain rule to express the partial derivative operator $\frac{\partial}{\partial R}$ as the sum partial derivate operators with respect to Cartesian coordinates. The chain rule can be expressed for all of the partial derivatives via the following matrix equation.

$$\begin{pmatrix} \frac{\partial \phi_j^A}{\partial r} \\ \frac{\partial \phi_j^A}{\partial R} \\ \vdots \end{pmatrix} = \begin{pmatrix} \frac{\partial x_{H1}}{\partial r} & \frac{\partial z_{H1}}{\partial r} & \cdots \\ \frac{\partial x_{H1}}{\partial R} & \frac{\partial z_{H1}}{\partial R} & \cdots \\ \vdots & \vdots & \ddots \end{pmatrix} \begin{pmatrix} \frac{\partial \phi_j^A}{\partial x_{H1}} \\ \frac{\partial \phi_j^A}{\partial z_{H1}} \\ \vdots \end{pmatrix} \quad (143)$$

The matrix of partial derivatives in Eq. (143) transforms the partial derivative with respect to Cartesian coordinates to partial derivatives with respect to internal Jacobi coordinates. However, the coordinate transformation equations (Eq. (141)) cannot be inverted analytically. Consequently, it is not possible to obtain analytic expressions for the expressions in the transformation matrix of Eq. (143). The coordinate transformation equations can be used to express the following chain rule relation.

$$\begin{pmatrix} \frac{\partial \phi_j^A}{\partial x_{H1}} \\ \frac{\partial \phi_j^A}{\partial z_{H1}} \\ \vdots \end{pmatrix} = \begin{pmatrix} \frac{\partial r}{\partial x_{H1}} & \frac{\partial r}{\partial z_{H1}} & \cdots \\ \frac{\partial R}{\partial x_{H1}} & \frac{\partial R}{\partial z_{H1}} & \cdots \\ \vdots & \vdots & \ddots \end{pmatrix} \begin{pmatrix} \frac{\partial \phi_j^A}{\partial r} \\ \frac{\partial \phi_j^A}{\partial R} \\ \vdots \end{pmatrix} \quad (144)$$

The matrices in Eq. (143) and (144) are inverses of one another as shown in the next equation.

$$\begin{pmatrix} \frac{\partial r}{\partial x_{H1}} & \frac{\partial r}{\partial z_{H1}} & \cdots \\ \frac{\partial R}{\partial x_{H1}} & \frac{\partial R}{\partial z_{H1}} & \cdots \\ \vdots & \vdots & \ddots \end{pmatrix}^{-1} = \begin{pmatrix} \frac{\partial x_{H1}}{\partial r} & \frac{\partial z_{H1}}{\partial r} & \cdots \\ \frac{\partial x_{H1}}{\partial R} & \frac{\partial z_{H1}}{\partial R} & \cdots \\ \vdots & \vdots & \ddots \end{pmatrix} \quad (145)$$

The transformation was accomplished by using Eq. (141) to compute the matrix of partial derivatives with respect to Cartesian coordinates. This matrix was inverted and used to compute the proper transformation to Jacobi partial derivatives.

Path Dependence of the ADT Mixing Angle

With properly transformed DCTs, the line integral, Eq. (35), can be carried out to determine the ADT mixing angle. Eq. (35) was derived under the assumption that the diabatic derivative couplings would be negligible. This was enforced by setting $\vec{\tau}_{12}^{D} = 0$ in Eq. (33). The condition that $\vec{\tau}_{12}^{A}$ must be curl-free (Eq. (36)) followed from this assumption. Under these conditions the line integral is expected to be path independent. However, as discussed earlier, truncating the electronic basis set ignores residual coupling between the $1\,^2A'$, $2\,^2A'$, and $1\,^2A''$ electronic eigenstates that span the ^2P manifold and electronic eigenstates outside the ^2P manifold. This has the effect of introducing a transverse component into $\vec{\tau}_{12}^{A}$ (Eq. (39)).[53, 56] This component is not removed by the ADT, invalidating the key assumption used to derive Eq. (35). Hence the error introduced by this component is termed nonremovable error.

This nonremovable derivative coupling also invalidates the curl-free condition as shown by Eq. (41). Consequently, the line integral is no longer expected to be path independent. To examine the path dependence of the line integral, two different paths were chosen. Both paths use the same starting point of $(r_0, \theta_0, R_0) = (4.402, \pi/2, 10)$ au. Path A integrates along the internal Jacobi coordinates in the following order: r, R, and θ. Path B integrates along the order θ, r, and R. Both paths end at the point labeled (r, θ, R). Figure 14 illustrates these two paths.

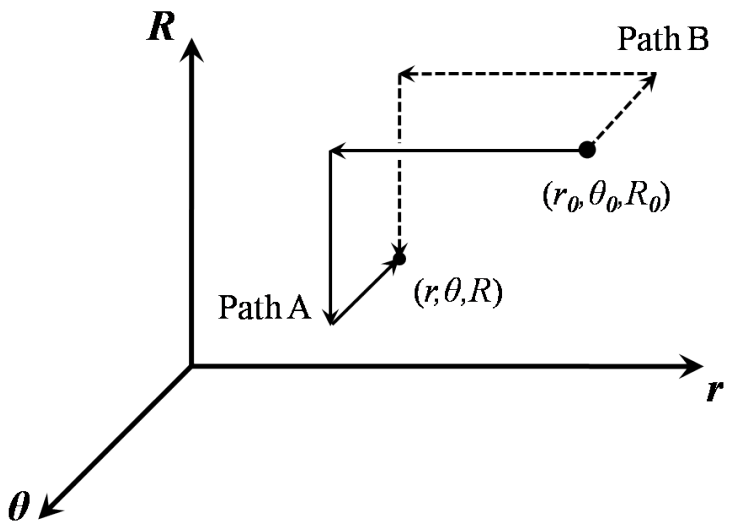

Figure 14. Depiction of Path A (solid line) and B (dashed line) within the 3-dimensional coordinate space defined by the Jacobi coordinates r, θ, and R

Figure 15 and Figure 16 compare these two paths for nuclear configurations for which $\theta = \pi/20$. This value of θ was chosen to avoid the step size error in the derivative couplings illustrated in Figure 11. Path B integrates along the R direction of τ_R^A for the collinear direction and is influenced by the step size error. Figure 15 plots the ADT mixing angle γ as a function of the Jacobi coordinate R along the line where $\theta = \pi/20$ and $r = 0.7$ au. The black circles in Figure 15 indicate the line integral passed through regions where the electronic structure calculation was not performed.

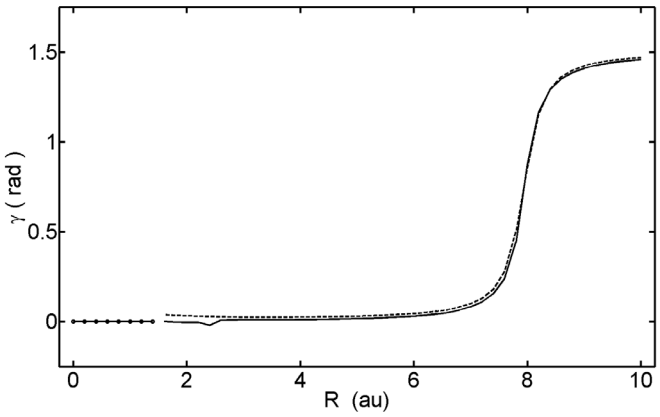

Figure 15. A comparison of the ADT mixing angle γ calculated from the line integral using Path A (solid line) and Path B (dashed line) along the line where $\theta = \pi/20$ and $r = 0.7$ au

Path A (solid) and Path B (dashed) are nearly identical in this figure indicating that the contribution of the transverse component of $\vec{\tau}_{12}^{A}$ is small in this region.

Figure 16 plots the ADT mixing angle γ as a function of the Jacobi coordinate R along the line where $\theta = \pi/20$ and $r = 2.402$ au.

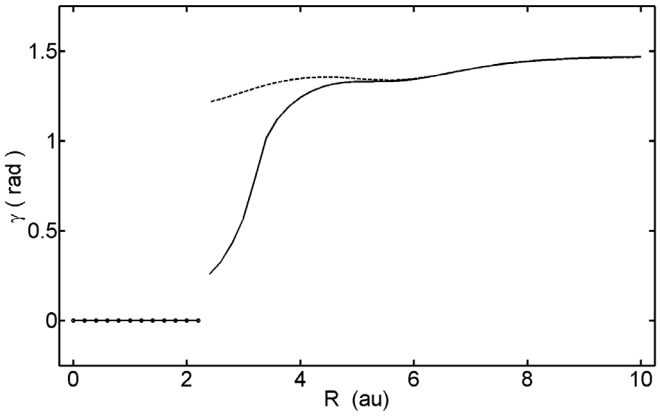

Figure 16. A comparison of the ADT mixing angle γ calculated from the line integral using Path A (solid line) and Path B (dashed line) along the line where $\theta = \pi/20$ and $r = 2.402$ au

In Figure 16 the paths are nearly identical for values of $R > 6$. The paths diverge for smaller values of R. It is not clear from the figure which path is more adversely affected by the transverse component, nor is the true value of the ADT mixing angle known.

In general, when R is large both paths are nearly identical for all values of the H_2 bond length r. As R decreases the paths diverge as r becomes large. The path difference indicates the presence of the transverse component of $\vec{\tau}_{12}^{A}$. This was further confirmed by calculating the curl of $\vec{\tau}_{12}^{A}$.

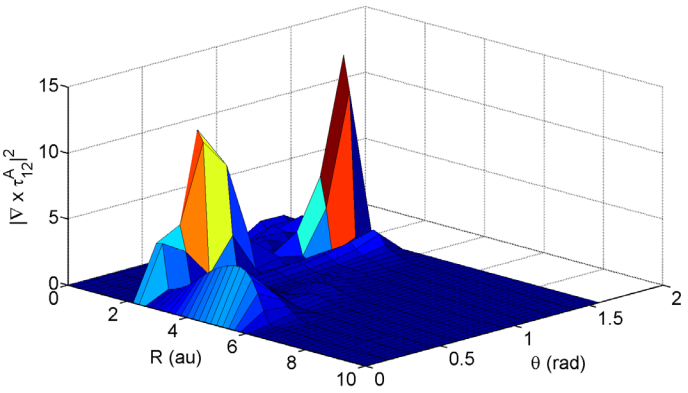

Figure 17. The magnitude of the curl of the derivative coupling vector field for $r = 2.402$ au

Figure 17 shows the total magnitude of the curl of $\vec{\tau}_{12}^{A}$ for the plane where $r = 2.402$ au. The curl was not calculated for points along the boundary of the data set. The curl is non-zero which is another indication, according to Eq. (41), of the presence of a non-zero transverse component of $\vec{\tau}_{12}^{A}$. However, Eq. (41) does not indicate the magnitude of the transverse component.

The transverse and longitudinal components of $\vec{\tau}_{12}^{A}$ can be computed using the following definitions found in Chapter 6 of Jackson's *Classical Electrodynamics* (3rd Ed.)[68]:

$$\vec{\tau}_{12}^{A,l} = -\frac{1}{4\pi}\vec{\nabla}\int\frac{\vec{\nabla}'\cdot\vec{\tau}_{12}^{A}}{|\vec{q}-\vec{q}'|}d^3\vec{q}'$$
$$\vec{\tau}_{12}^{A,t} = \frac{1}{4\pi}\vec{\nabla}\times\vec{\nabla}\times\int\frac{\vec{\tau}_{12}^{A}}{|\vec{q}-\vec{q}'|}d^3\vec{q}' \qquad (146)$$

This decomposition was not performed given the under-sampled features in the NACTs. An accurate determination of $\vec{\tau}_{12}^{A,t}$ would require the electronic structure calculation to be performed on a denser numerical grid.

Expected Behavior of the ADT Mixing Angle and the Diabatic Surfaces

The effect of $\vec{\tau}_{12}^{A,t}$ can be further characterized by starting and ending the line integral at points where the true value of the ADT mixing angle is known. Using arguments given by Alexander[26, 27], the ADT mixing angle can be predicted for certain symmetry configurations of B + H_2. While Alexander's data was restricted to the equilibrium H_2 bond length *r*, these arguments are valid for all values of *r*.

The diagonal diabatic PESs V_{xx}, V_{yy}, and V_{zz} obey the same symmetry relationship that the adiabatic PESs obey: $V(r,\pi-\theta,R) = V(r,\theta,R)$. The diabatic coupling surface V_{xz} is different. In the range $0 < \theta < \frac{\pi}{2}$ the center-of-charge of the H_2 molecule lies closest to the lobe of positive phase of the 2*p* orbital perpendicular to BF Z axis while for $\frac{\pi}{2} < \theta < \pi$ the center-of-charge lies closest to the lobe of negative phase. Thus, the diabatic coupling surface V_{xz} obeys the symmetry relation $V(r,\pi-\theta,R) = -V(r,\theta,R)$.

This requires that $V_{xz}(\theta = 0) = V_{xz}\left(\theta = \frac{\pi}{2}\right) = 0$ to maintain the continuity of V_{xz}. According to Eq. (38), this requires the ADT mixing to be zero or $\pi/2$ for $\theta = 0$ and $\pi/2$.[26] The value of the ADT mixing angle is set by examining the behavior of the $1^2A'$ and $2^2A'$ PESs.

As stated earlier the $1^2A'$ and $2^2A'$ orbitals can be chosen to correspond to the p_z and p_x orbital of the boron atom respectively. The ADT given by Eq. (31) can be seen as an orthogonal rotation of these orbitals in the SF *XZ* plane, where the orientation of the H_2 molecule influences the magnitude of the rotation. When the B + H_2 system has C_{2v} symmetry ($\theta = \pi/2$) the $1\,^2A'$ and $2\,^2A'$ adiabatic PESs do not cross. This is illustrated in Figure 18.

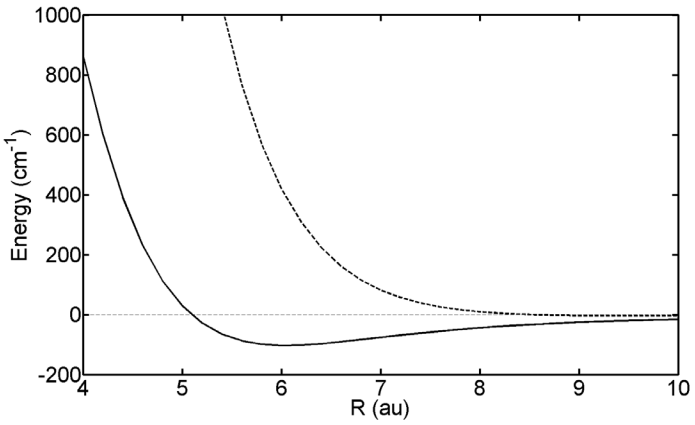

Figure 18. A plot of the $1\,^2A'$ (solid line) and $2\,^2A'$ (dashed line) adiabatic PESs for C_{2v} geometry and r = 1.402 au

In Figure 18 the solid line corresponds to the $1\,^2A'$ PES and the dashed line corresponds to the $2\,^2A'$ PES. This figure can be compared with the upper plot in Figure 3 in Alexander.[26] As the boron atom approaches the H_2 molecule in the perpendicular

geometry the p_x and p_z do not change orientation. Since the 1 $^2A'$ and 2 $^2A'$ adiabatic PESs do not cross the 1 $^2A'$ PES maintains the p_z orbital orientation and the 2 $^2A'$ maintains the p_x orbital orientation. The ADT mixing angle is constant, here taken to be zero for all values R along the line where $\theta = \pi/2$ and r = 1.402 au.

For the collinear configuration ($\theta = 0$ and r = 1.402 au), $C_{\infty h}$ symmetry, the 1 $^2A'$ and 2 $^2A'$ adiabatic PESs appear to meet near $R = 6.5$ as shown in Figure 19. Again the solid and dashed lines correspond to the 1 $^2A'$ and 2 $^2A'$ PESs respectively. This figure can be compared with the lower plot in Figure 3 in Alexander.[26] If the numerical grid in Figure 19 were more densely sampled the PESs would touch at a single point.

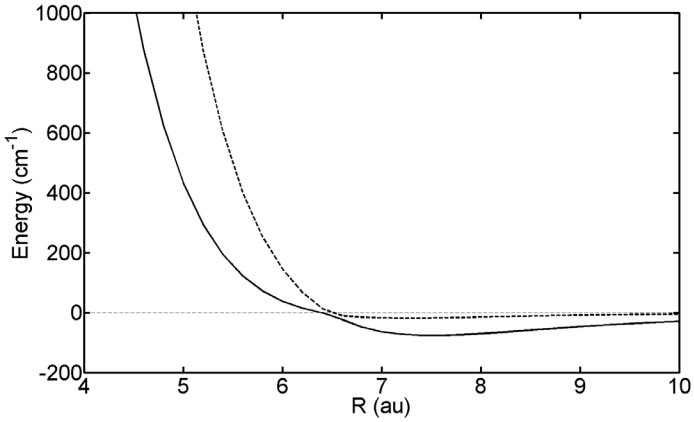

Figure 19. A plot of the 1 $^2A'$ (solid line) and 2 $^2A'$ (dashed line) adiabatic PESs for $C_{\infty h}$ geometry and r = 1.402 au

This is an example of a conical intersection. As the PESs approach $R = 6.5$ au each undergoes a sharp change in slope. The slope of the 1 $^2A'$ PES surface as it approaches $R = 6.5$ au from the left most closely matches the slope of the 2 $^2A'$ PES surface as it continues to greater values of R. Likewise, the slope of the 2 $^2A'$ PES surface as it

approaches $R = 6.5$ au from the left most closely matches the slope of the $1\,^2A'$ PES surface as it continues to greater values of R. The orientations of the $1\,^2A'$ and $2\,^2A'$ wave functions undergo a sharp change near $R = 6.5$ au. For $R < \sim 6.5$ au the $1\,^2A'$ wave function corresponds to the p_z orbital. For $R < \sim 6.5$ au the $1\,^2A'$ wave function corresponds to the p_x orbital. The $2\,^2A'$ wave function undergoes a similar transition. This sharp transition is the source of the singularity in the DCTs in this region.

The goal of the ADT is to remove this singularity. Figure 19 suggests that this can be done by choosing the ADT mixing angle so that the resulting diabatic PESs for the collinear configuration are associated with the same orbital. This eliminates the sharp change in orientation thereby eliminating the derivative coupling in the diabatic basis. This is accomplished by setting the ADT mixing angle equal to $\pi/2$ radians where the p_x state lies energetically below the p_z state ($R < \sim 6.5$ au), and setting the angle to zero where the p_z state lies energetically below the p_x state ($R > \sim 6.5$ au).[26] The result of this transformation is shown in Figure 20.

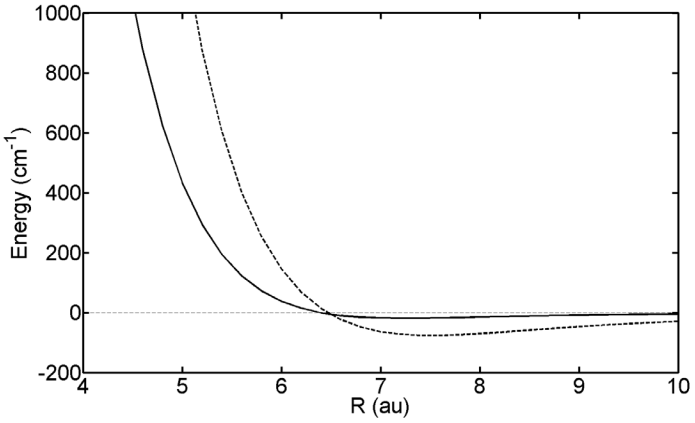

Figure 20. A plot of the V_{xx} (solid line) and V_{zz} (dashed line) diabatic PESs for $C_{\infty h}$ geometry and $r = 1.402$ au

In Figure 20 the solid and dashed lines correspond to the V_{xx} and V_{zz} PESs respectively. After the transformation wave functions associated with V_{xx} and V_{zz} correspond entirely to the p_x and p_z orbitals respectively. There is no sharp orientation change in the diabatic wave functions thus the derivative coupling term is eliminated.

With the behavior of the ADT mixing angle established for C_{2v} and $C_{\infty h}$ geometries the effect of $\vec{\tau}_{12}^{A,t}$ on the ADT mixing can be further characterized by performing the line integral along a path that begins in a C_{2v} configuration and ends in a $C_{\infty h}$ configuration. A C_{2v} configuration is chosen as a starting point since value of the ADT mixing angle zero for all C_{2v} configurations. This eliminates the requirement of choosing a single reference point for the line integral. This path is illustrated in Figure 21.

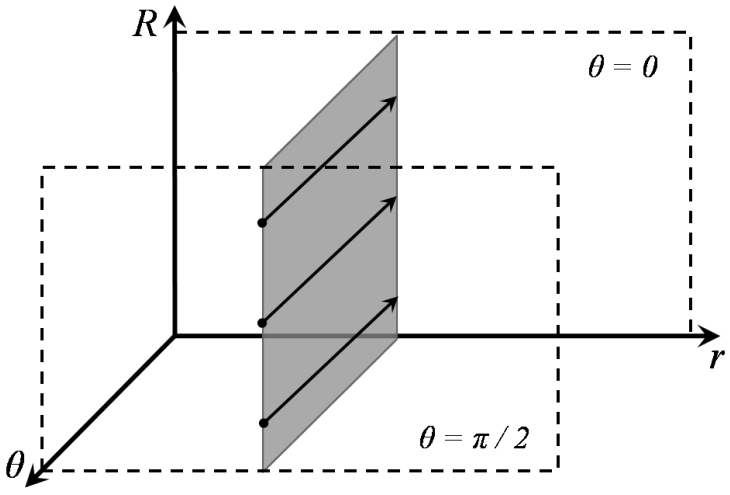

Figure 21. An illustration of the line integral path chosen to take advantage of symmetry derived boundary conditions

The line integral is performed starting at $\theta = \pi/2$ and ending at $\theta = 0$ for every value of R for a given value of the H_2 bond length. Figure 22 presents the results of the ADT mixing angle calculated using the path described in Figure 21 for $r = 1.402$ au and $\theta = 0$. The dot-dash lines indicate zero and $\pi/2$ levels of the ADT mixing angle. The black dots indicate the line integral passed through regions where the electronic structure calculation was not performed. Figure 22 has a step-function-like transition between zero and $\pi/2$ near $R \approx 6.5$ a.u. as expected from Figure 19; however, the sharp features immediately before and after the transition are due to step-size error.

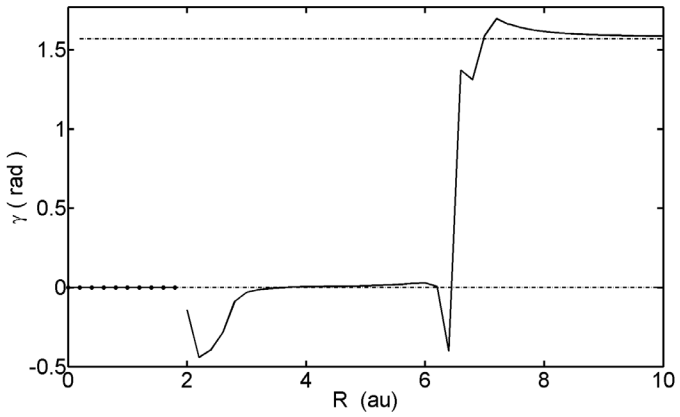

Figure 22. The ADT mixing angle calculated using the line integral starting at $\theta = \pi/2$ and ending at $\theta = 0$ for $r = 1.402$ au

Figure 22 also shows a deviation from $\pi/2$ for $R > 8$ au and a deviation from zero $R <$ 3. These deviations are due to contributions of $\vec{\tau}_{12}^{A,t}$ to the line integral.

Figure 23 presents another example of how the transverse component can affect the line integral. Here the line integral is carried out for $r = 2.402$ au and $\theta = 0$.

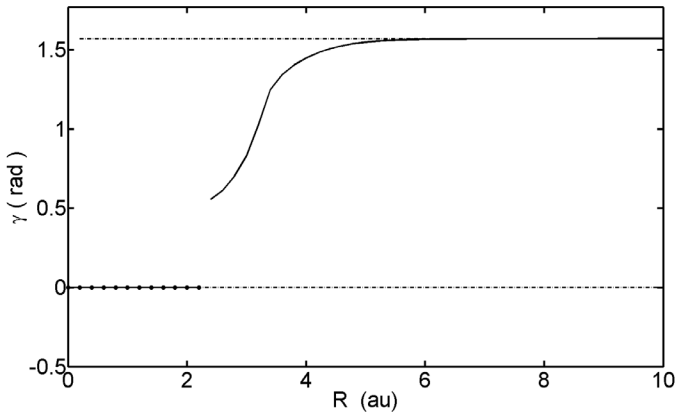

Figure 23. The ATD mixing angle calculated using the line integral starting at $\theta = \pi/2$ and ending at $\theta = 0$ for $r = 2.402$ au

For this value of r and θ the $1\ ^2A'$ and $2\ ^2A'$ wave functions do not experience a rapid change in orientation. The ATD mixing is expected to remain $\pi/2$. As shown in Figure 23 angle has a value near $\pi/2$; however, as R gets smaller it smoothly deviates from $\pi/2$. This is a dramatic manifestation of the nonremovable component of the derivative coupling vector field.

In general for the $\theta = 0$ plane, for $r \leq 1.902$ au the ADT mixing angle transitions from $\pi/2$ to zero at some point as R becomes smaller for the collinear configuration. The jagged features near these transitions are due to step size error in the DCTs as discussed earlier. However, the smooth deviations from zero and $\pi/2$ are due to the nonremovable component of the derivative coupling error. This error dominates the ADT mixing angle $r \geq 2.402$ au, and is illustrated in Figure 23.

The ADT mixing angle passes on the errors introduced by $\vec{\tau}_{12}^{A,t}$ to the diabatic surfaces. This is clearly seen in the V_{xz} diabatic PES. Figure 24 shows the V_{xz} PES

calculated for $r = 2.902$ au bond length. The diabatic coupling surface is not zero along the line $\theta = 0$ as predicted by symmetry arguments. Figure 24 demonstrates that the error introduced into the diabatic PESs can be energetically significant.

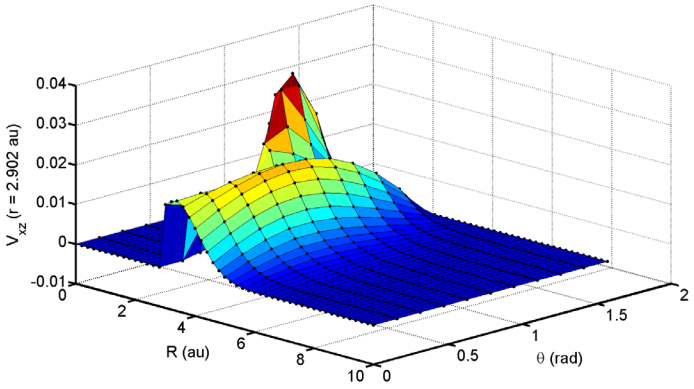

Figure 24. The diabatic coupling surface V_{xz} for $r = 2.902$ au calculated using the ADT mixing angle determined by the line integral starting at $\theta = \pi/2$ and ending at $\theta = 0$

The deviation from zero is on the order of 0.01 au. The scattering calculation discussed later probes energies in the range of zero to 0.01 au. This deviation will adversely impact the molecular dynamics calculated using these surfaces.

Weighted-Path Line Integral

Unless the derivative coupling vector field $\vec{\tau}_{12}^{A}$ is decomposed into its longitudinal and transverse components the contribution of the transverse component to the ATD mixing angle cannot be removed. As mentioned earlier, this decomposition was not attempted in this work due to the under-sampled features in the NACTs. As the line integral is performed error from $\vec{\tau}_{12}^{A,t}$ is accumulated along the path with the points

furthest from the reference point suffering the most contamination. The symmetry derived boundary conditions helped mitigate this error by reducing the length of the path required to make a determination of the ADT mixing angle. The path described in Figure 21 involved a single integration along a path in the τ_θ^A component of the derivative coupling vector field. This integration scheme, however, did not prevent the error displayed in Figure 24.

The line integral determines the ADT mixing angle up to an overall constant γ_0. A single starting point is selected to ensure this constant is the same for all determinations of the ADT mixing angle for a given data set. The symmetry derived boundary conditions provide a way to begin the line integral from multiple points while setting the overall constant consistently across the data. The direction of the integration in Figure 21 can be reversed provided the symmetry derived boundary conditions are used to set the constant appropriately. When this is done the value of the ATD mixing angle is set properly in the $\theta = 0$ plane and the integral accumulates error along the path to the $\theta = \pi/2$ plane. Each path accumulates the same magnitude of error at the end of the path.

For clarity, Path 1 is defined as the path that begins in the $\theta = \pi/2$ plane and ends in the $\theta = 0$ plane. Path 2 begins in the $\theta = 0$ plane and ends in the $\theta = \pi/2$ plane. These two paths can be used to define a weighted-path line integral using the following equation:

$$\gamma(\theta) = \left(\frac{\theta}{\pi/2}\right)\gamma_1(\theta) + \left(\frac{\pi/2 - \theta}{\pi/2}\right)\gamma_2(\theta) \qquad (147)$$

In Eq. (147) $\gamma_1(\theta)$ and $\gamma_2(\theta)$ are the ADT mixing angle calculated along Path 1 and 2 respectively. A linear weighting is used to emphasize the contribution of each path in the region where it has accumulated the least error. Figure 25 illustrates these three paths.

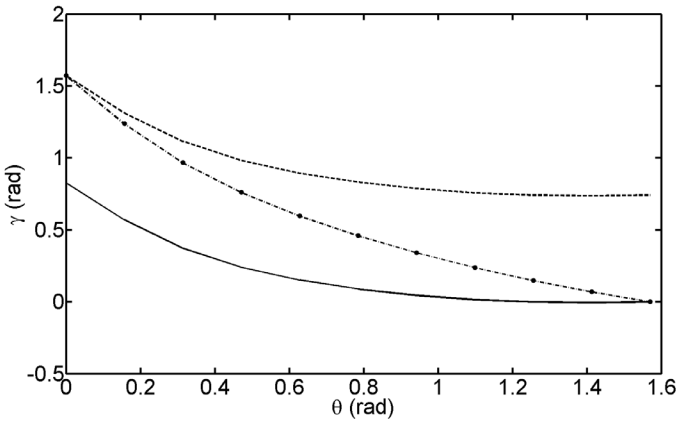

Figure 25. The ADT mixing angle plotted as function of θ for Path 1 (solid line), Path 2 (dashed), and the weighted path (dash-dot) for $r = 2.402$ au and $R = 3.0$ au

Figure 25 plots the ADT mixing angle for the path corresponding to $r = 2.402$ au and $R = 3.0$ au. Path 1 (solid line) is set to the symmetry derived value of zero at $\theta = \pi/2$, but fails to reach the expected value of $\gamma = \pi\backslash 2$ at $\theta = 0$. Path 2 (dashed line) is set to the symmetry derived value of $\pi/2$ at $\theta = 0$, but fails to reach the expected value of $\gamma = 0$ at $\theta = \pi\backslash 2$. Paths 1 and 2 have accumulated the same magnitude of error at the end of each path. The weighted path (dash-dot) is obtained from Eq. (147). While the weighted path has the correct symmetry derived boundary conditions, it is not known to what extent the accumulated error is mitigated. Figure 15 and Figure 16 indicate that the transverse component $\vec{\tau}_{12}^{A,t}$ is not evenly distributed throughout the data set.

The weighted-path line integral approach was used to calculate the ADT mixing angle for the entire data set. Only Path 1 was used when regions where the electronic structure calculation was not performed were encountered. Figure 26 shows the V_{xz} PES calculated for $r = 2.902$ au bond length this time using the ADT determined by the weighted-path line integral.

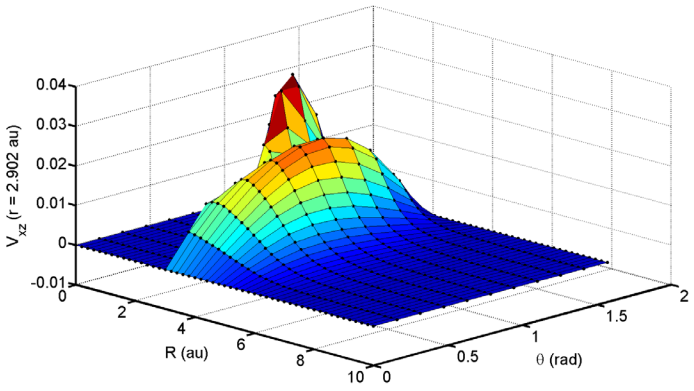

Figure 26. The diabatic coupling surface V_{xz} for $r = 2.902$ au constructed using ADT mixing angle calculated from the weighted-path line integral

Unlike Figure 24, the diabatic coupling surface V_{xz} is now zero along the line $\theta = 0$. The weighted-path line integral successfully corrects the deviations from the symmetry derived boundary condition; however, it is sensitive to step-size error in the data. This is illustrated in the next series of figures. The diabatic coupling surface V_{xz} displayed in Figure 27 has a step-size induced error along the line $\theta = 0$ near $R = 8$.

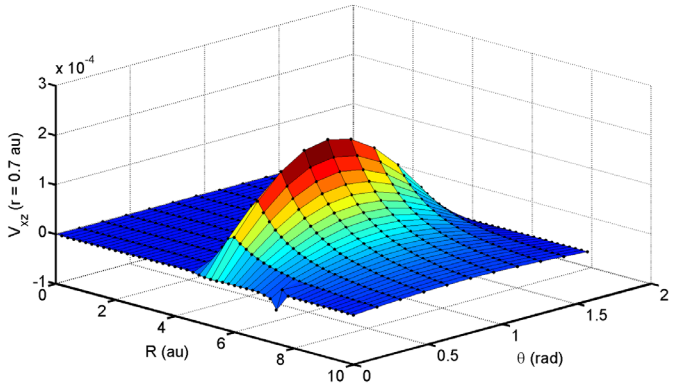

Figure 27. The diabatic coupling surface V_{xz} for $r = 0.7$ au constructed using ADT mixing angle calculated from the line integral starting at $\theta = \pi/2$ and ending at $\theta = 0$

This diabatic surface was the result of an ADT determined by integration using only Path 1. The derivative coupling surface for the component $\tau^A_{\theta,12}$ for $r = 0.7$ is shown in Figure 28 to illustrate the source of this step-size error.

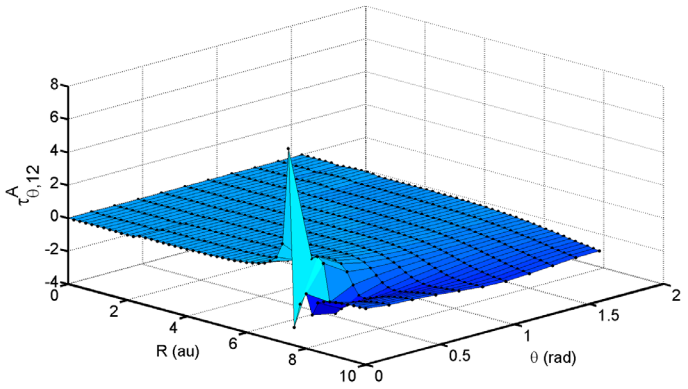

Figure 28. The derivative coupling surface for the component $\tau^A_{\theta,12}$ for $r = 0.7$ au

The sharp discontinuity near in $R = 8$ au is indicative of a conical intersection. The $\tau^A_{\theta,12}$ component of the derivative coupling surfaces was interpolated using a cubic spline fit in

an unsuccessful effort to alleviate step-size error. The grid of nuclear coordinates does not sample these sharp features well enough for interpolation to be of any benefit. The cubic spline fit did not model the shape of the discontinuity along θ well. The next figure illustrates the effect the discontinuity near R = 8 au in Figure 28 has on the diabatic surface constructed from the ADT determined by the weighted-path line integral over the uninterpolated derivative couplings.

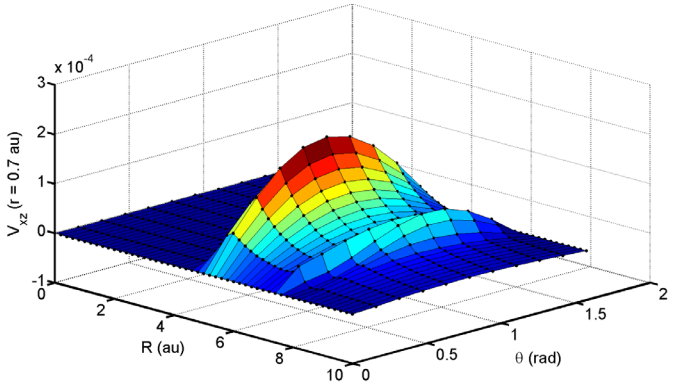

Figure 29. The diabatic coupling surface V_{xz} for $r = 0.7$ au constructed using ADT mixing angle calculated from the weighted-path line integral

Figure 29 shows that the weighted-path line integral performed well in the regions where the derivative coupling term is smooth. However, according to Eq. (147) Path 2 is weighted more heavily than Path 1 near $\theta = 0$. Path 1 is affected by the discontinuity in the DCT and carries this error through the path. All regions affected by this step-size error were smoothed using cubic spline interpolation as shown in Figure 30.

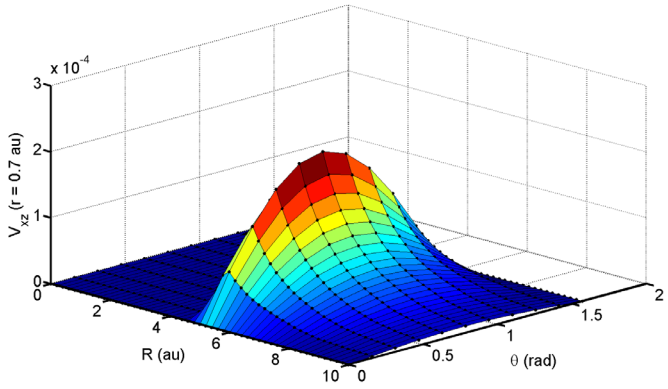

Figure 30. The smoothed diabatic coupling surface V_{xz} for $r = 0.7$ au constructed using ADT mixing angle calculated from the weighted-path line integral

A selection of diabatic surfaces constructed using the ADT determined from the weighted-path line integral are presented in Appendix H.

Diabatic Potential Energy Surface Fitting

The diabatic PESs are required to represent the electrostatic interaction potential $\hat{V}_{el}$ in the asymptotic basis. Eqs. (74), (75), and (76) express the analytical representation of $\hat{V}_{el}$ in the asymptotic basis. This representation includes the expansion coefficients $V_{\lambda_r\lambda_a\mu}(r,R)$ which are determined from a numerical fit to the diabatic PESs. In Eq. (88) the diabatic PES are expressed as an expansion in terms of reduced Wigner rotation matrix elements, Eq. (87). The expansion coefficients are calculated numerically by fitting each diabatic PES to the appropriate reduced Wigner rotation matrix. The relationship between the expansion coefficients $V_{\lambda_r\lambda_a\mu}(r,R)$ and the reduced Wigner rotation matrices is given by Eqs. (84) and (87). The reduced Wigner rotation

matrix elements are generated by using the following relationship with the associated Legendre polynomials[83, 99]:

$$\begin{aligned} d_{\mu 0}^{\lambda_r}(\theta) &= \left(\frac{4\pi}{2\lambda_r+1}\right) Y_{\mu}^{\lambda_r *}(\theta, \phi = 0) \\ &= (-1)^{\mu} \left[\frac{(\lambda_r-\mu)!}{(\lambda_r+\mu)!}\right]^{\frac{1}{2}} P_{\lambda_r}^{\mu}(\cos\theta) \end{aligned} \quad (148)$$

An analytic expression is derived for each expansion coefficient. This process is shown for V_{xz} as an example. The V_{xz} PES is fit using the $d_{10}^{\lambda_r}(\theta)$ reduced matrix element given by

$$\begin{aligned} d_{10}^{\lambda_r}(\theta) &= \left[\frac{(\lambda_r-1)!}{(\lambda_r+1)!}\right]^{\frac{1}{2}} P_{\lambda_r}^{1}(\cos\theta) \\ &= -\left[\frac{1}{\lambda_r(\lambda_r+1)}\right]^{\frac{1}{2}} P_{\lambda_r}^{1}(\cos\theta) \end{aligned} \quad (149)$$

Inserting Eq. (149) into Eq. (88) yields

$$V_{xz}(r,\theta,R) = \sum_{\lambda_r=1} V_{xz}^{\lambda_r}(r,R) \left\{ -\left[\frac{1}{\lambda_r(\lambda_r+1)}\right]^{\frac{1}{2}} P_{\lambda_r}^{1}(\cos\theta) \right\} \quad (150)$$

Both sides of Eq. (150) are then multiplied by $P_{\lambda_r'}^{1}(\cos\theta)\sin\theta$ and integrated over θ from 0 to π to yield

$$\begin{aligned} &\int_0^{\pi} V_{xz}(r,\theta,R) P_{\lambda_r'}^{1}(\cos\theta)\sin\theta\, d\theta \\ &= \int_0^{\pi} \left\{ \sum_{\lambda_r=1} V_{xz}^{\lambda_r}(r,R) \left\{ -\left[\frac{1}{\lambda_r(\lambda_r+1)}\right]^{\frac{1}{2}} P_{\lambda_r}^{1}(\cos\theta) \right\} \right\} P_{\lambda_r'}^{1}(\cos\theta)\sin\theta\, d\theta \end{aligned} \quad (151)$$

The associated Legendre polynomials have the following orthogonality relationship:

$$\int_0^{\pi} P_l^m(\cos\theta) P_{l'}^m(\cos\theta)\sin\theta\, d\theta = \frac{2(l+m)!}{(2l+1)(l-m)!}\delta_{k,l} \quad (152)$$

The orthogonality relationship simplifies Eq. (151) to

$$V_{xz}^{\lambda_r}(r,R) = \frac{-\left(\lambda_r + \frac{1}{2}\right)}{[\lambda_r(\lambda_r+1)]^{1/2}} \int_0^{\pi} V_{xz}(r,R) P_{\lambda_r}^1(\cos\theta) \sin\theta \, d\theta \qquad (153)$$

Since the data was only calculated for θ between 0 and $\pi/2$ the symmetry properties of each surface with respect to $\theta = \pi/2$ was used to extend each surface to $\theta = \pi$. The V_{xz} has odd symmetry with respect to $\theta = \pi/2$ the values of V_{xz} change sign when reflected about this plane. The other potential energy surfaces have even symmetry with respect to this plane. The analytic expressions for the expansion coefficients of these surfaces are given by

$$V_{zz}^{\lambda_r}(r,R) = \left(\lambda_r + \frac{1}{2}\right) \int_0^{\pi} V_{zz}(r,R) P_{\lambda_r}^0(\cos\theta) \sin\theta \, d\theta$$

$$V_{s}^{\lambda_r}(r,R) = \left(\lambda_r + \frac{1}{2}\right) \int_0^{\pi} V_{s}(r,R) P_{\lambda_r}^0(\cos\theta) \sin\theta \, d\theta \qquad (154)$$

$$V_{d}^{\lambda_r}(r,R) = \frac{\left(\lambda_r + \frac{1}{2}\right)}{[\lambda_r(\lambda_r-1)(\lambda_r+1)(\lambda_r+2)]^{1/2}} \int_0^{\pi} V_{d}(r,R) P_{\lambda_r}^2(\cos\theta) \sin\theta \, d\theta$$

These integrals are performed along the θ direction for each (r,R) pair. In Eqs. (153) and (154) the λ_r' symbols have been replaced with λ_r symbols. This work calculated fit coefficients for $\lambda_r = 0,2,4,6,8$ to be directly comparable to the surfaces calculated by HIBRIDON™, a suite FORTRAN programs used to calculate Alexander's B + H_2 surfaces.[26, 100]

The number oscillations a given associated Legendre polynomial experiences increases as λ_r increases. Beyond a limiting value of λ_r the finite grid is no longer able to sample the oscillations. This aliasing limits the order of the associated Legendre polynomials that can be accurately projected on the numeric grid. An example of this is shown in Figure 31. Although the solid line clearly represents P_{36}^0, when it is sampled

using the θ grid used in this work (dashed line) it appears to be P_4^0. The θ grid is marked with an asterisk.

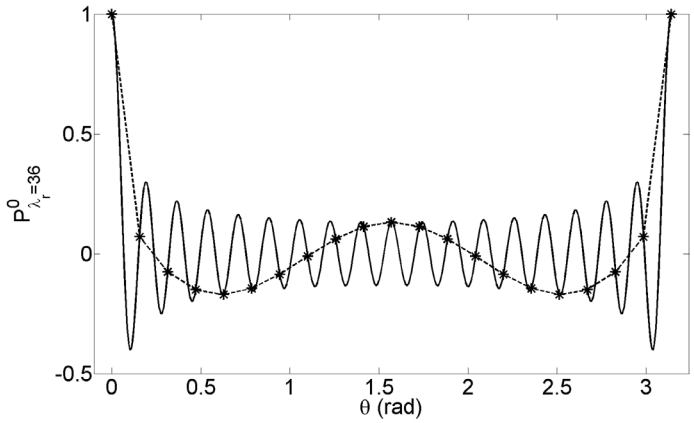

Figure 31. The associated Legendre polynomial P_{36}^0 plotted on a finely sampled grid (solid) and the grid used in this work (dashed) with grid points indicated by an asterisk

Associated Legendre polynomials with orders higher than $\lambda_r = 20$ are aliased on the θ grid used in this work. Furthermore, the accuracy of the fit coefficients steadily decreases as λ_r increases due to step-size error in the integration of Eqs. (153) and (154). This is illustrated in Figure 32. In Figure 32 the RMS fitting error for V_{zz} is plotted as a function of the fit order λ_r for $(r, R) = (1.402, 8.0)$. The RMS error decreases for the first three values of λ_r, but steadily increases to the first alias peak.

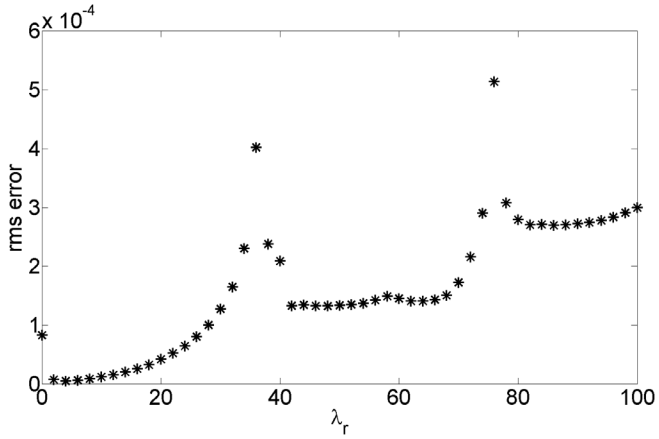

Figure 32. RMS fitting error of V_{zz} calculated as a function of fit order for $(r, R) = (1.402, 8.0)$ au

This effect can be reduced by interpolating the diabatic PESs along θ on a more densely sampled grid and then performing the fit. Unlike the DCTs, the diabatic PESs vary slowly along θ as illustrated in Figure 33.

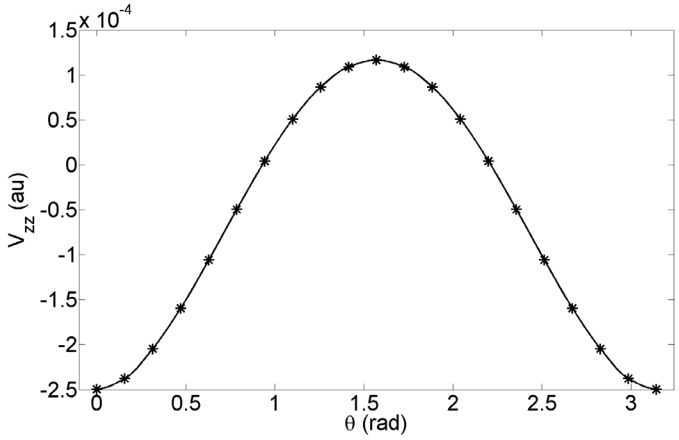

Figure 33. The diabatic PES V_{zz} (asterisks) interpolated using a piecewise cubic Hermite polynomial (solid line) plotted as a function of θ for $(r, R) = (1.402, 8.0)$ au

The asterisks mark the points where the electronic structure calculation was carried out. The solid line is a piecewise cubic Hermite polynomial interpolation of the data. Figure 34 is a comparison of the RMS error for the interpolated and non-interpolated data.

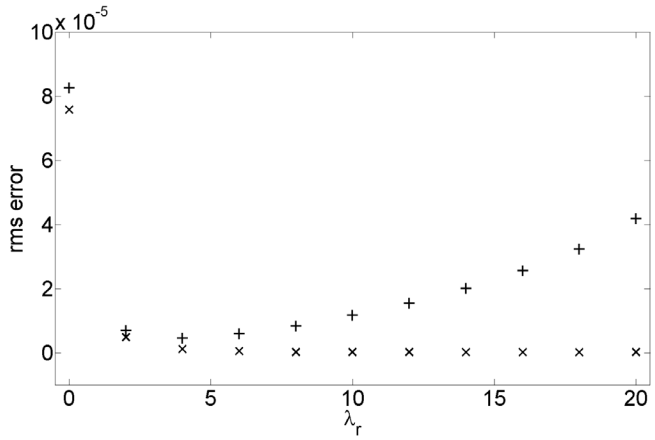

Figure 34. A comparison of the RMS fitting error of the non-interpolated data (+) and the interpolated data (x)

As shown in Figure 34, the RMS error of the interpolated data (+) is less affected by step-size error in Eqs. (153) and (154). The diabatic PESs were interpolated along the θ direction before calculating the fit coefficients. Figure 35 plots a selection of these coefficients which is directly comparable with Figure 6 of Alexander.[27]

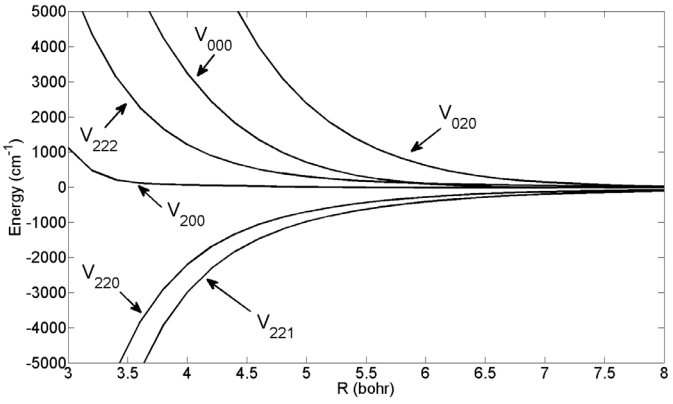

Figure 35. A selection of $V_{\lambda_r\lambda_a\mu}$ expansion coefficients plotted as a function of R

For Figure 35 the sign of the V_{222} coefficient was chosen to be consistent with Alexander's of V_d (Eqs. (89) and (90)). The values of the expansion coefficients are comparable to Alexander. The expansion coefficients were then inserted into Eq. (92) to yield the $V_{\lambda_r\lambda_a\mu}$ expansion coefficients required in Eq. (74) to represent the electrostatic interaction potential in the asymptotic basis.

Determining the H_2 Potential Energy Surface

As implied by Eq. (79), the diabatic PESs capture the effects of the electrostatic interaction potential $\hat{V}_{el}$ and the H_2 PES $V_{H_2}(r)$. For this work the contribution of $V_{H_2}(r)$ was not removed from the adiabatic or diabatic PESs. As a result the contribution of the H_2 PES must be removed from the $V_{000}(r,R)$, Eq. (92), expansion coefficients to calculate $\hat{V}_{el}$ properly. The H_2 PES also appears as a term in the effective PES matrix elements given by Eq. (97). The minimum value of $V_{H_2}(r)$ is also used to set the overall

offset of the data so that $V_{H_2}(r = 1.402) = 0$ au. This allows the results of this work to compared with Alexander[26] and Weeks.[37]

The contribution of $V_{H_2}(r)$ can be isolated by examining the asymptotic behavior of the diabtic PESs. The diabatic PESs have the following limits:

$$\lim_{R\to\infty} V_{xx}(r,R) = \lim_{R\to\infty} V_{yy}(r,R) = \lim_{R\to\infty} V_{zz}(r,R) = V_{H_2}(r)$$
$$\lim_{R\to\infty} V_{xz}(r,R) = 0 \qquad (155)$$

In the asymptotic limit the contribution of $\hat{V}_{el}$ goes to zero leaving only the contribution of $V_{H_2}(r)$. Consequently the coupling surface V_{xz} goes to zero while the other diabatic PESs converge to $V_{H_2}(r)$ as R gets large. Likewise the fitting function V_s also coverges to $V_{H_2}(r)$ while V_d converges to zero. Thus the expansion coefficients $V_{\lambda_r\lambda_a\mu}$ in Eq. (92) go to zero in the asymptotic limit as expected.

An accurate determination of $V_{H_2}(r)$ requires the adiabatic PESs to be calculated for a variety of values of the H_2 bond length in the asymptotic limit (large R). Figure 36 plots the expansion coefficient $V_{000}(r,R)$ near R = 10 as function of R for r = 1.402 au along with an exponential fit to this data. Figure 36 demonstrates that the asymptotic limit has not been reached by R = 10 and that $V_{000}(r = 1.402, R) \neq 0$ for large R. The values of the fit coefficients for $V_{000}(r = 1.402, R)$ exhibit a near exponential decay near $R = 10$.

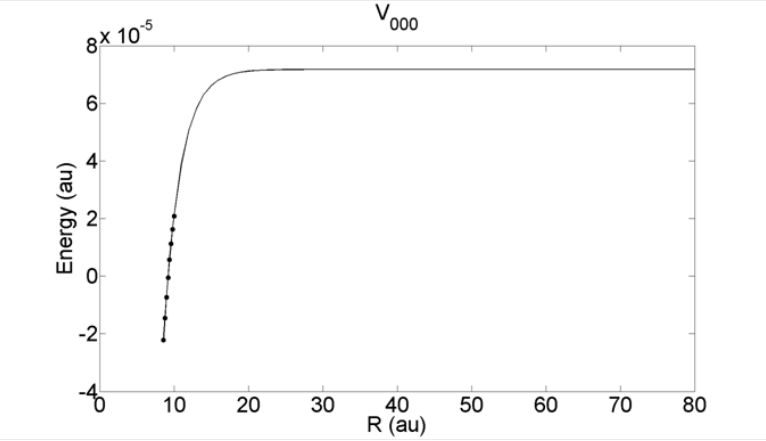

Figure 36. The expansion coefficient $V_{000}(r, R)$ near $R = 10$ plotted as a function of R for $r = 1.402$ au (dots) with an exponential fit to these points (solid line)

The last eight points ($R = 8.6 - 10$ au) were fit using a least squares fit with following exponential fitting function:

$$f(R) = a_1 e^{-a_2(R-a_3)} + a_4 \qquad (156)$$

The coefficient a_4 captures the value of the fit coefficient in the asymptotic limit. This fit is shown in Figure 36 as a solid line. The asymptotic values of V_{000} obtained this way are used to the global energy offset of the PESs so that $V_{H_2}(r = 1.402) = 0$ au. Figure 37 compares these values with the theoretical Morse potential values and *ab initio* determined LSTH (Liu-Siegbahn-Truhlar-Horowitz)[101, 102] values. The values of $V_{H_2}(r)$ obtained using the exponential fit of the V_{000} expansion coefficient (asterisk) are comparable to the Morse potential (dashed), but more closely follow the LSTH values (solid).

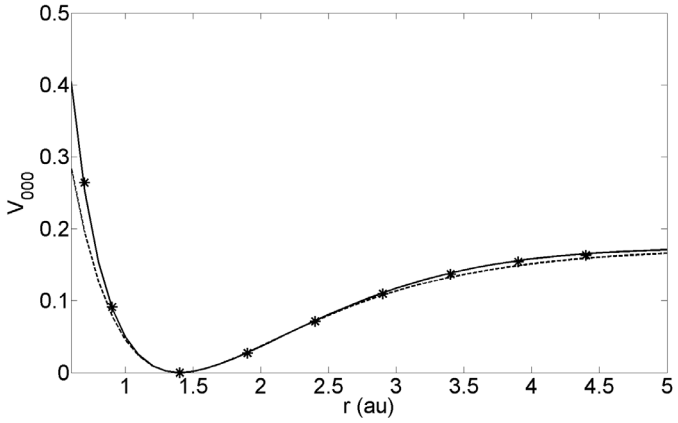

Figure 37. A comparison of LSTH (solid), Morse potential (dashed), and the asymptotic expansion coefficient V_{000} (asterisk) values for $V_{H_2}(r)$

The values of $V_{H_2}(r)$ must be interpolated to match the grid used for the effective PESs (Eq. (97)). Since $V_{H_2}(r)$ for this work is only sampled at nine points, the method of interpolation must be chosen carefully. Figure 38 compares three methods for fitting the H_2 PES in the asymptotic limit for the range $R = 0.7 - 2.5$ au.

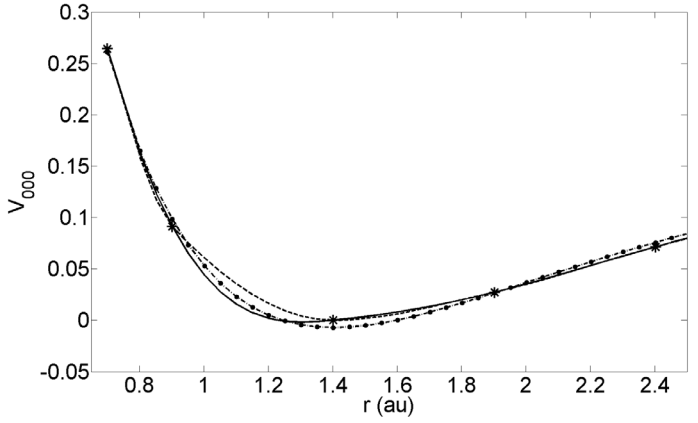

Figure 38. A comparison of three methods for fitting the H_2 PES in the asymptotic limit: cubic spline (solid), piecewise cubic Hermite (dashed), Morse fitting function (dash-dot), V_{000} data (asterisk)

Overall, the least squares fit using a Morse potential fitting function (dash-dot) had the most residual error since it was not constrained to the data (asterisk). The cubic spline (solid) and piecewise cubic Hermite polynomial (dashed) interpolation curves are nearly equal for $R > 2.0$ au. All three methods have difficulty fitting the well region located near $r = 1.402$ au. Only the piecewise cubic Hermite polynomial curve preserves the value of zero at $r = 1.402$ au. The cubic spline curve shifts the location of the minimum value of the potential well. The piecewise cubic Hermite polynomial curve was selected to construct $V_{H_2}(r)$ in the asymptotic limit. Future determinations of adiabatic PESs for other systems should include calculations made in the asymptotic limit.

Effective Potential Energy Surfaces

The diabatic effective PESs were generated using Eq. (97). A FORTRAN code was developed to read fit coefficient data; construct and interpolate the H_2 PES $V_{H_2}(r)$; interpolate the fit coefficients using cubic spline interpolation to yield data for any user specified grid of nuclear coordinates; generate the diabatic effective PESs on the user specified grid; and, diagonalize the diabatic effective PESs matrix at each value of (r, R) forming adiabatic effective PESs.

A selection of diabatic effective PESs are presented in Appendix I. Figure 39 compares the $r = 1.402$ au values of the first 14 diagonal diabatic effective PESs with those produced by HIBRIDON™.[100] Comparisons made with HIBRIDON™ are made using Eq. (90) as the definition of V_d. This does not affect the diagonal elements of $V_{eff}^{D}(r, R)$, nor does the sign of the off-diagonal elements affect the dynamics.

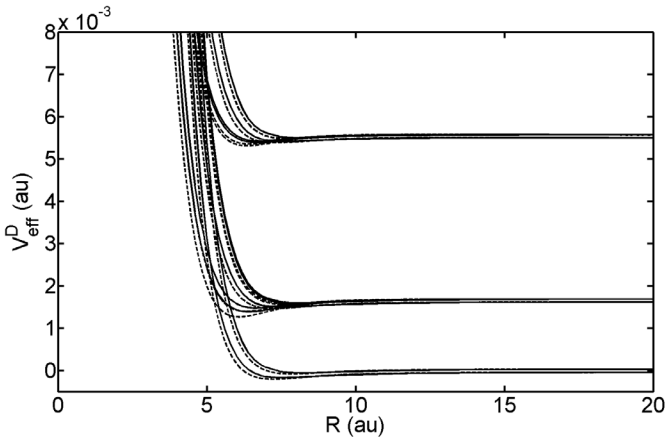

Figure 39. The first 14 diagonal matrix elements of $V_{eff}^{D}(r,R)$ for $r = 1.402$ au: the results of this work (solid line), the results produced by HIBRIDON™ (dashed line)

The surfaces plotted in Figure 39 correspond to the $j = 0, 2, 4$ values of the H_2 rotor. The potential well for the HIBRIDON™ surfaces is lower in energy; however, the surfaces share the same H_2 rotor energy spectrum as R becomes large. This indicates that the global offset has been chosen and applied properly. The H_2 rotor levels are split by spin-orbit coupling. Figure 40 plots the effective PESs corresponding to $j = 0$ on a smaller scale so that the differences between the HIBRIDON™ surfaces and this work might be more clearly observed.

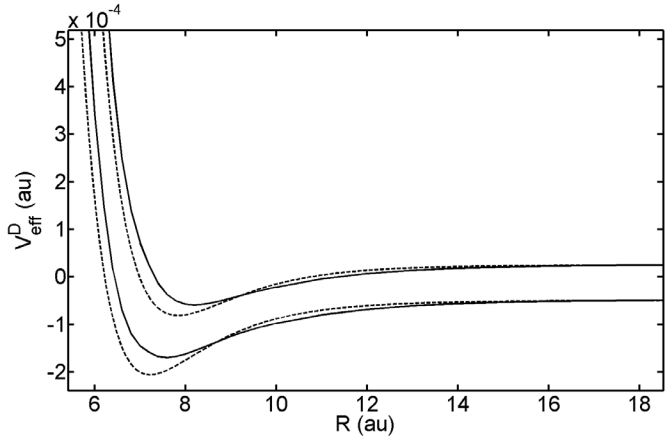

Figure 40. The first two diagonal matrix elements of $V_{eff}^{D}(r,R)$ for $r = 1.402$ au corresponding to $j = 0$: the results of this work (solid line), the results produced by HIBRIDON™ (dashed line)

As shown in Figure 40, the effective PESs calculated by HIBRIDON™ have deeper potential wells which occur at smaller values of R. This comparative behavior is typical of the effective PESs for higher j.

Figure 41 compares the off-diagonal elements of the first row of $V_{eff}^{D}(r,R)$ with those produced by HIBRIDON™.

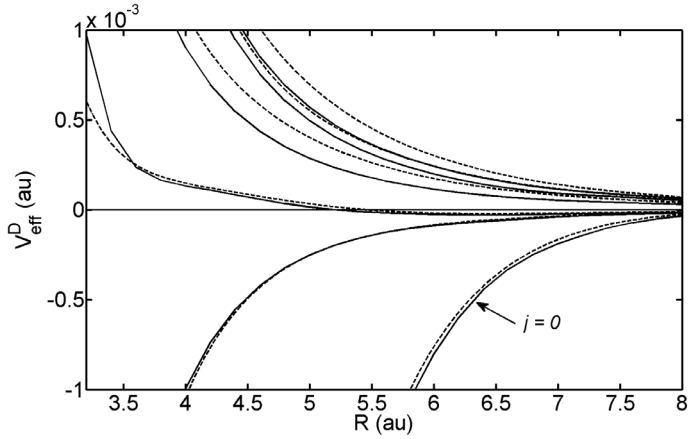

Figure 41. The off-diagonal matrix elements of $V_{eff}^{D}(r,R)$ corresponding to $j = 0$ and 2 (the single $j = 0$ surface is indicated): the results of this work (solid line), results produced by HIBRIDON™ (dashed line)

The single off-diagonal surface corresponding to $j = 0$ is marked in Figure 41. The other surfaces correspond to $j = 2$. While the off-diagonal surfaces are similar in form to those calculated by HIBRIDON™, there are significant differences. The differences observed in Figure 40 and Figure 41 will affect the resulting scattering matrix elements calculated from these surfaces. This will be explored in the next section.

Effective PES matrix element are represented by an *n*-by-*n* matrix in the asymptotic basis where *n* is the number of basis functions (Eq. (98)). This matrix can be diagonalized via a similarity transformation at each (r, R) value (Eq. (102)) to yield a diagonal set of adiabatic effective PESs as shown below.

$$\mathbb{U}^{\dagger}(r,R)\begin{pmatrix} V_{eff}^{D}(r,R)_{11} & V_{eff}^{D}(r,R)_{12} & \cdots \\ V_{eff}^{D}(r,R)_{21} & V_{eff}^{D}(r,R)_{22} & \cdots \\ \vdots & \vdots & \ddots \end{pmatrix}\mathbb{U}(r,R) = \begin{pmatrix} V_{eff}^{A}(r,R)_{11} & 0 & \cdots \\ 0 & V_{eff}^{A}(r,R)_{22} & \cdots \\ \vdots & \vdots & \ddots \end{pmatrix} \quad (157)$$

The adiabatic effective PESs are the eigenvalues of the effective PES matrix. These eigenvalues and are ordered in ascending order. A selection of these surfaces is presented in Appendix J.

The adiabatic effective PESs display avoided crossings similar to those encountered in the electronic adiabatic surfaces (Figure 19). An example of these crossings is shown in Figure 42.

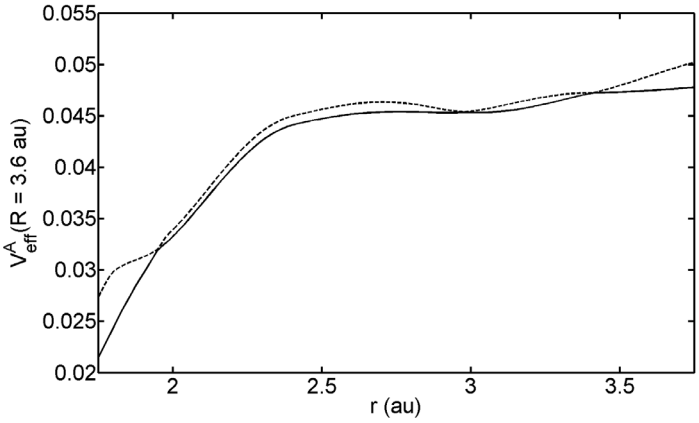

Figure 42. A slice along $R = 3.6$ au of the first (solid line) and second (dashed) adiabatic effective PESs

In Figure 42 a slice along $R = 3.6$ au of the first and second adiabatic effective PESs is plotted. This slice has surface crossings near $r = 2, 3,$ and 3.4 au. At this time it is not known if these crossings share similar properties to the conical intersections encountered in electronic adiabatic PESs, nor is it known how these crossing influence the dynamics of the system.

Scattering Matrix Elements

The diabatic effective PES data for $r = 1.402$ au was extracted and used in conjunction with code developed by Weeks[37] to calculate scattering matrix elements via the CPM. The code uses the SOA to propagate wave packets into the interaction region and back. Absorbing boundary conditions (BCs) are used to prevent the reflected wave packets from exiting the propagation grid and aliasing. The absorbing BCs allow the smaller propagation grid to accommodate longer propagation times. Table 2 lists the numerical parameters used to calculate the scattering matrix elements.

Table 2. Parameters used in the 1D propagation of wave packets

Item	Value (au)
Coordinate grid size	256
Coordinate grid spacing	0.3
Number of time steps	250 000
Time step size	25
Initial wave packet position	25
Initial wave packet momentum	± 5
Initial wave packet spread	0.5
Amplitude of absorbing BC	0.001
Spread of absorbing BC	15

These are the same propagation parameters used in Weeks.[37] The next figures compare scattering matrix elements for transitions out of the state $|j, k, j_a, \omega\rangle = |0, 0, 1/2, 1/2\rangle$.

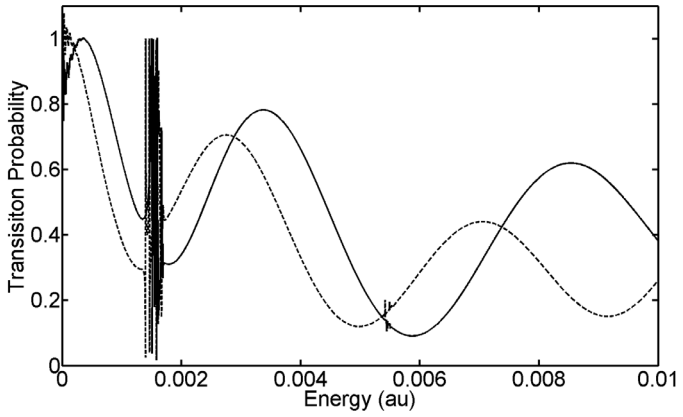

Figure 43. Transition probabilities as a function of energy for the transition $|0, 0, 1/2, 1/2\rangle \rightarrow |0, 0, 1/2, 1/2\rangle$: results from this work (solid line), results based on PESs produced by HIBRIDON™ (dashed line)

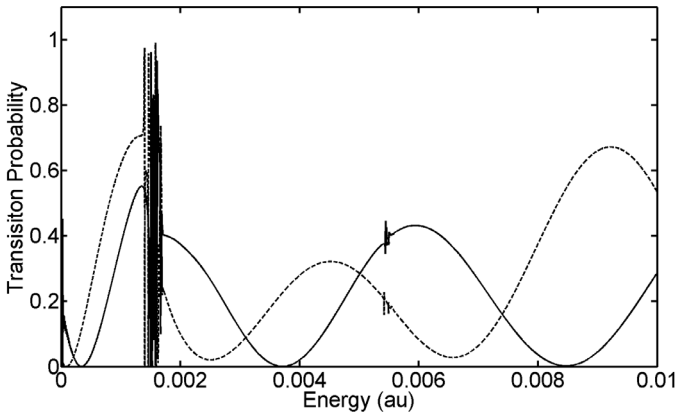

Figure 44. Transition probabilities as a function of energy for the transition $|0,0,1/2,1/2\rangle \rightarrow |0,0,1/2,3/2\rangle$: results from this work (solid line), results based on PESs produced by HIBRIDON™ (dashed line)

The scattering matrix elements shown Figure 43 and Figure 44 are characterized by broad smoothly varying Stueckelberg oscillations[103] which are interrupted by rapidly oscillating Feshbach resonances[104] near energy values of 0.0015 and 0.0055 au. While the transition probabilities have similar structure qualitatively, these figures show that both the Stueckelberg oscillations and the Feschbach resonances are sensitive to changes in the input diabatic effective PESs.

The Feshbach resonances occur at energies corresponding to the vibrational eigenvalues of the weakly bound B ⋯ H_2 van der Waals complex.[37] As shown in Figure 45 the Feshbach resonances are shifted to higher energies than those based on HIBRIDON™ surfaces. This is consistent with the difference in potential well depths of the diagonal effective PESs. On average the potential well depth for the first 20 diagonal diabatic effective PESs in this work is 2.6×10^{-5} au higher in energy than the HIBRIDON™ data set. This has the effect of raising the vibrational eigenvalues of the weakly bound B ⋯ H_2 van der Waals complex.

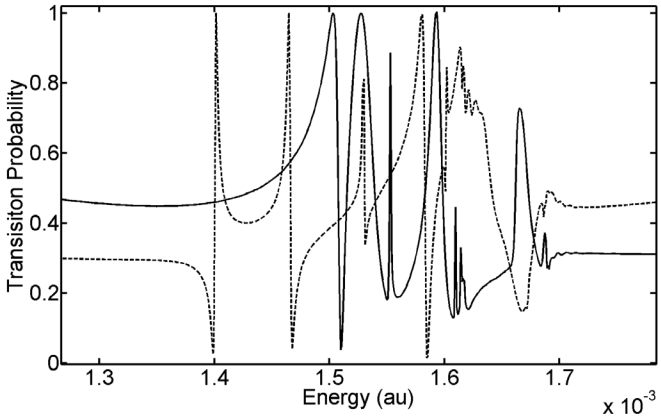

Figure 45. A plot of the Feshbach resonance region of the transition the transition $|0,0,1/2,1/2\rangle \rightarrow |0,0,1/2,1/2\rangle$: results from this work (solid line), results based on PESs produced by HIBRIDON™ (dashed line)

The shape of the Feshbach resonances is also different. This is largely due in to the differences in the off-diagonal coupling terms (Figure 41). The Feshbach resonances are also sharper for the HIBRIDON™ data set. This suggests that the shallower well structure observed in Figure 40 does not trap evolving wave packet amplitude for as long. The wave packet amplitude exiting the interaction region makes contributions to the correlation function (see Eqs. (124) and (138)) for smaller durations leading to broader features in the scattering matrix elements.

The shapes of the potential wells influence the phase of the Stueckelberg oscillations. As seen in Figure 43 and Figure 44, the maxima of the Stuekelberg oscillations calculated in this work occur at larger energies compared to those of the HIBRIDON™ data set. As the reactant wave packet enters the interaction region it experiences an effective PES with a different shape than the surfaces based on the HIBRIDON™ data set. During the interaction the evolving wave packet explores

different regions of the other effective PESs before exiting the interaction region. The differences in the shape of the effective PESs is primarily responsible for the phase differences in the Stuekelberg oscillations. The complicated interaction of the evolving wave packet with multiple effective PESs makes it difficult to predict *a priori* how changes in the effective PESs will affect the resulting scattering matrix elements. It is also not known how changes in the effective PESs affect the calculated cross sections and reaction rates.

IV. Conclusion

The diabatic and adiabatic effective PESs for the inelastic collision of a boron atom with a hydrogen molecule (Eq. (1)) were calculated from the $1\,^2A'$, $2\,^2A'$, and A'' adiabatic electronic PESs and the associated DCTs. The processing steps leading to the effective PESs are outlined in Table 3.

Table 3. Processing steps for obtaining effective PESs

Processing Steps	
1.	*Ab initio* calculation of electronic adiabatic PESs and DCTs
2.	Smooth electronic adiabatic PESs
3.	Apply Cartesian-to-Jacobi coordinate transformation to derivative couplings
4.	Calculate ADT mixing angle using weighted-path line integral
5.	Construct electronic diabatic PESs
6.	Smooth step-size induced error in electronic diabatic PESs
7.	Fit electronic diabatic PESs to associated Legendre polynomials
8.	Isolate asymptotic behavior and set global data offset
9.	Interpolate fit coefficients to user defined grid
10.	Construct diabatic effective PESs
11.	Diagonalize diabatic effective PES matrix elements to construct adiabatic effective PESs

The adiabatic electronic surfaces were calculated at the SA-MCSCF/CI level including the H_2 bond length as a DOF.[29, 45, 46] The derivative couplings were calculated directly from the SA-MCSCF/CI wave functions using analytic gradient techniques.[29, 47] The electronic structure calculation was not attempted for nuclear configurations with internuclear distances below a set threshold. In addition to these regions, the raw data set

contained points which did not converge to values near their neighboring points. In the process of performing the electronic structure calculation a metric based on the continuity of the angular momentum of the system was used to gauge convergence. There were a small number of points that met this metric but did not converge properly. These outlying points were smoothed in the electronic adiabatic surfaces; however, no attempt was made to smooth the derivative coupling surfaces due to their naturally spiky topology. Each outlying point was identified individually and smoothed.

After the DCTs were transformed from Cartesian to Jacobi coordinates the ADT mixing angle was calculated by performing a line integral through the derivative coupling vector field (Eq. (35)). When the ADT mixing angle was first calculated the standard approach of choosing a single reference point for the line integral was used. The resulting line integral was not path independent as assumed when deriving Eq. (35). Residual coupling between boron ^2P states and other states not considered in this work give rise to a transverse component of the derivative coupling field.[53, 56] This component introduces an error which accumulates along the line integral path—the nonremovable error.

This error has been characterized in regions in close proximity to conical intersections by integrating over a closed path. [72-76] When the path does not enclose a conical intersection the path integral should be zero. When a conical intersection is enclosed the resulting mixing angle should be $n\pi$ where the integer n is the number of enclosed conical intersections.[6, 67] The deviation from these values is a measure of the nonremovable error.

This work represents the first effort to characterize this error for a wide range of nuclear coordinates. The path independence of the line integral is one measure of the influence of the nonremovable error. As shown in Figure 15, not all regions in the data are strongly affected by this error. Previously published results on B + H_2 for $r = 1.402$ au lie in a region weakly affected by this error (Figure 22).[26, 27] Path integrals in regions where $r \geq 1.902$ au have significant path dependence (Figure 16). The curl of the derivative coupling vector field further verifies the presence of a non-zero transverse vector field. However, the path independence of the line integral is not an absolute measure of the nonremovable error. In this work, the symmetry of B + H_2 is used to predict the true value of the ADT mixing angle, providing an absolute measure of the contribution of the nonremovable error for the collinear and perpendicular nuclear configurations.

Symmetry derived boundary conditions allow the line integral to begin at any point at which the ADT mixing angle is known. This allows the overall length of the path to be reduced thereby limiting the amount of accumulated error. The ADT mixing angle was calculated by integrating over the θ component of the derivative coupling field and using boundary conditions to set the proper offset. This technique does not prevent significant error from accumulating (Figure 23). This error is passed on to the diabatic PESs (Figure 24).

The ADT mixing angle can only be predicted for specific nuclear configurations with special symmetry. Furthermore, the nonremovable error is not equally distributed through the data set (Figure 17). This prevents the contribution of the nonremovable error from being removed at each point along the path. For the B + H_2 system, the

symmetry derived boundary conditions allow two paths to be taken through the same data. The results of these line integrals can be averaged giving weight to regions less affected by the nonremovable error. While this does not eliminate the contribution of this error, the weighted-path line integral enforces the proper boundary conditions (Figure 26). This work introduces the weighted-path line integral as a method of producing more accurate diabatic PESs. The technique shows promise for systems with a high degree of symmetry and can aid the calculation of diabatic PESs for systems with a larger number of nuclei.

The weighted line integral is also sensitive to step-size error introduced by the finite grid of coordinates. The derivative coupling surfaces are most affected by this error due to the sharp features that they can possess (Figure 28). The nuclear grid used in this work under sampled these sharp features (Figure 11). Consequently, efforts to reduce this error by interpolating the derivative coupling data set were unsuccessful. Step size error was smoothed by masking the points and using cubic spline interpolation.

The smoothed diabatic PESs were fit using associated Legendre polynomials which in turn yielded the expansion coefficients required to construct the matrix elements of the electrostatic interaction potential $\hat{V}_{el}$. The asymptotic behavior of the system was modeled by using a least squares fit with an exponential fitting function for $R = 8.6 - 10$ au. The predicted H_2 PES surface agrees with the LSTH surface.[101, 102] Piecewise cubic Hermite polynomial was used to interpolate the H_2 PES in the asymptotic limit. The resulting surface was used to account for the contribution of the hydrogen molecule in the full Hamiltonian (Eq. (60)) as well as subtract its influence in the V_{000} expansion coefficient (Eq. (92)).

A FORTRAN code was developed to interpolate the expansion coefficients to a user defined grid. The diabatic effective PESs (Eq. (97)) were calculated on this grid. 20 basis functions (all basis up to and including $j = 6$) were used to compute the matrix elements $V_{eff}^{D}(r,R)_{\zeta'\zeta}$. The data corresponding to $r = 1.402$ au was extracted from these matrix elements and compared to values calculated by HIBRIDON™. The surfaces showed good agreement in shape and magnitude. The matrix elements $V_{eff}^{D}(r,R)_{\zeta'\zeta}$ were diagonalized at each (r,R) value to yield adiabatic effective PESs. These surfaces exhibit surface crossings similar to those encountered in the electronic adiabatic surfaces (compare Figure 19 with Figure 42); however, it is not known if they share similar properties associated with conical intersections.

Finally, the values of the diabatic effective PESs for $r = 1.402$ au were used in the same one dimensional CPM method code developed by Weeks et al.[37] to compute scattering matrix elements. The resulting scattering matrix elements exhibit Stuekelberg oscillations[103] and Feshbach resonances[104] shifted to higher energies than those based on the HIBRIDON™ data set.[37] The scattering matrix are sensitive to the form of the input effective PESs (Figure 43 and Figure 44). The difference in the well depths of the diabatic effective PESs affect both the Stuekelberg oscillations and Feshbach resonances.

Summary of Key Contributions

This work presents the adiabatic PESs and DCTs of the B + H_2 system calculated over an extended range of nuclear coordinates over all three internal nuclear DOF (boron distance, H_2 orientation, and H_2 bond length). Previous *ab initio* calculations of the adiabatic PESs for the B + H_2 system fixed the molecular hydrogen bond length at the

equilibrium value of 1.402 a.u. [26, 27, 36, 37] The DCTs were used to calculate the ADT mixing angle. Previous used other methods to estimate the ADT.[26, 27] The error introduced by employing a truncated set of adiabatic states was characterized by examining the path dependence of the line integral and using symmetry derived boundary conditions. The weighted-path line integral was employed as a new method for reducing the effect this error has the resulting diabatic PESs. The procedure for determining the $V_{\lambda_r \lambda_a \mu}$ expansion coefficients was modified to account for variable H_2 bond length. The two dimensional diabatic and adaiabtic effective PESs were calculated. The effective PESs data was extracted for $r = 1.402$ au and used to calculate scattering matrix elements using the CPM. These results were compared with previous results in the first attempt to observe the sensitivity of this calculation to the input electronic structure data.

Recommendations for Future Work

This work lays the foundation for many significant research endeavors. Table 4 summarizes the significant extensions of this work.

Table 4. A list of further research topics

	Future Work
1.	Relax centrifugal sudden approximation
2.	Relax pure precession approximation
3.	Extend asymptotic basis beyond $J = 1/2$
4.	Implement 2D propagation in CPM
5.	Examine the sensitivity of scattering matrix elements, cross sections, and reaction rates to input PESs
6.	Allow vibrational transitions ($v \neq v'$)
7.	Calculate diabatic B + H_2 surface for $r > 1.902$ au using non-NACT techniques

The CS approximation was implemented in this work to reduce the computational overhead. Relaxing the CS approximation will require significant changes to the code used to compute the effective PESs and calculate the scattering matrix elements. Once implemented, a comparison can be made between CS and non-CS scattering matrix elements to determine the error introduced by this approximation.

Relaxing the pure precession approximation (constant spin-orbit coupling coefficient ξ) requires a new set of electronic adiabatic PESs to be calculated. This effect must be included as a relativistic correction in the electronic structure code. Once accomplished, the error introduced by the pure precession approximation can be assessed.

The equations for cross-sections and reaction rates (Eqn. (139) and (140)) require the asymptotic basis to be extended beyond a total angular moment of $J = 1/2$. Although the asymptotic Hamiltonian is diagonal with respect to total angular momentum, extending the basis set will greatly increase the computational resources required to compute each total angular momentum block.

The computational requirements will also greatly increase when implementing 2D propagation in the CPM code. Once implemented the dynamical effects of the surface crossings observed in Figure 42 can be studied. There is further interest in observing how the added DOF, r, affects the Feshbach resonances and Stuekelberg oscillations observed in the transition probabilities (Figure 43 and Figure 44). 2D propagation could also serve as another measure of the sensitivity of the scattering matrix calculation. It would also be possible to study the sensitivity of the scattering matrix calculation by examining an analytic potential, such as the Morse potential. The parameters of an

analytic potential could be varied and the effect on the resulting scattering matrix could be studied.

Once the 2D propagation code has been implemented, vibrational transitions can be considered. Considering energies in this range also opens up the possibility that boron will react forming BH_2. The full treatment of the reaction requires PESs of the BH + H complex; however, reaction probabilities can be estimated by measuring the probability amplitude that exits the propagation grid for small R.

The results of this work indicate that the nonremovable error made a greater contribution to the ADT mixing angle for H_2 bond lengths $r > 1.902$ au. The B + H_2 surfaces calculated by Alexander were calculated for $r > 1.902$ au.[26, 27] Thus the calculation of the B + H_2 diabatic PESs for $r > 1.902$ au using methods that do not use DCTs would be valuable for determining how these methods are affected by the nonremovable error. This would also provide a way to further judge the utility of the weighted-path line integral approach to calculating the ADT mixing angle.

Appendix A The Antihermitian Property of the Derivative Coupling Terms

The DCTs given by Eq. (21) can be shown to be antihermitian. This important property reduces the number of DCTs that must be computed. The derivation of this property begins by taking the gradient with respect to nuclear coordinates on both sides of Eq. (14), the orthonormality condition of the electronic eigenstates.

$$\vec{\nabla}_{q_n}\left\{\int d\boldsymbol{q}_e \Phi_i^*(\boldsymbol{q}_n,\boldsymbol{q}_e)\Phi_j(\boldsymbol{q}_n,\boldsymbol{q}_e)\right\} = \vec{\nabla}_{q_n}\{\delta_{ij}\}$$

The gradient $\vec{\nabla}_{q_n}$ will pass through the integral and after using the product rule the following expression is obtained:

$$\int d\boldsymbol{q}_e\{\vec{\nabla}_{q_n}\Phi_i^*(\boldsymbol{q}_n,\boldsymbol{q}_e)\}\Phi_j(\boldsymbol{q}_n,\boldsymbol{q}_e) + \int d\boldsymbol{q}_e\Phi_i^*(\boldsymbol{q}_n,\boldsymbol{q}_e)\{\vec{\nabla}_{q_n}\Phi_j(\boldsymbol{q}_n,\boldsymbol{q}_e)\} = 0$$

When Eq. (21), the definition of the derivative coupling term $\vec{\tau}_{ij}^{A}$, is substituted into this expression the antihermitian relationship is obtained:

$$\vec{\tau}_{ij}^{A} = -\vec{\tau}_{ij}^{A*}$$

Appendix B The Derivation of the Generalized Hellmann-Feynmann Theorem

The generalized Hellmann-Feynmann theorem, Eq. (27), gives the clearest indication when a system will behave nonadiabatically. It shows that when the difference between the adiabatic PESs for two different electronic eigenstates is small, the derivative coupling $\vec{\tau}_{ij}^{A}$ will be large, possibly singular if the PESs are equal.

The Hellman-Feynman theorem establishes the following relationship

$$\frac{d}{d\lambda}E(\lambda) = \left\langle \psi(\lambda) \middle| \frac{d}{d\lambda}\hat{H}(\lambda) \middle| \psi(\lambda) \right\rangle$$

where $\hat{H}(\lambda)$ is a Hermitian operator, $|\psi(\lambda)\rangle$ is a normalized eigenstate, and $E(\lambda)$ is the corresponding eigenvalue all of which depend on the real valued parameter λ.[106] This equation involves a single eigenstate and eigenvalue, thus if $\left\langle \psi(\lambda) \middle| \frac{d}{d\lambda}\hat{H}(\lambda) \middle| \psi(\lambda) \right\rangle$ were expressed as a matrix it would be diagonal. To compare two different eigenstates and eigenvalues the generalized Hellmann-Feynman must be used.

The electronic TISE defined by Eq. (12) serves as the starting point for this derivation. In the expression above, λ is a collection of real parameters. These parameters correspond to the nuclear coordinates $\boldsymbol{q}_{\mathrm{n}}$ in Eq. (12). The derivative operator $\frac{d}{d\lambda}$ corresponds to $\vec{\nabla}_{q_n}$. The derivation proceeds as follows:

$$\hat{H}_{elec}|j(\boldsymbol{q}_n)\rangle = V_j^A(\boldsymbol{q}_n)\,|j(\boldsymbol{q}_n)\rangle$$

$$\langle i(\boldsymbol{q}_n)|\hat{H}_{elec}|j(\boldsymbol{q}_n)\rangle = \langle i(\boldsymbol{q}_n)|V_j^A(\boldsymbol{q}_n)|j(\boldsymbol{q}_n)\rangle$$

$$= V_j^A(\boldsymbol{q}_n)\langle i(\boldsymbol{q}_n)|j(\boldsymbol{q}_n)\rangle$$

$$= V_j^A(\boldsymbol{q}_n)\delta_{ij}$$

The derivatives with respect to nuclear coordinates are then taken on both sides and the product rule is used to expand the left hand side of the equation.

$$\vec{\nabla}_{q_n}\langle i(\boldsymbol{q}_n)|\hat{H}_{elec}|j(\boldsymbol{q}_n)\rangle$$

$$= \{\vec{\nabla}_{q_n}\langle i(\boldsymbol{q}_n)|\}\{\hat{H}_{elec}|j(\boldsymbol{q}_n)\rangle\} + \langle i(\boldsymbol{q}_n)|\vec{\nabla}_{q_n}\hat{H}_{elec}|j(\boldsymbol{q}_n)\rangle$$

$$+ \{\langle i(\boldsymbol{q}_n)|\hat{H}_{elec}\}\{\vec{\nabla}_{q_n}|j(\boldsymbol{q}_n)\rangle\}$$

The definition of the DCTs $\vec{\tau}_{ij}^A$, Eq. (21), is then used to further simplify the expression.

$$\langle i(\boldsymbol{q}_n)|\vec{\nabla}_{q_n}\hat{H}_{elec}|j(\boldsymbol{q}_n)\rangle + V_j^A(\boldsymbol{q}_n)\vec{\tau}_{ji}^A + V_i^A(\boldsymbol{q}_n)\vec{\tau}_{ij}^A = 0$$

After using antihermitian property of the DCTs derived in Appendix A, the general Hellman-Feynman theorem is given by

$$\vec{\tau}_{ij}^A = \frac{\langle i(\boldsymbol{q}_n)|\vec{\nabla}_{q_n}\hat{H}_{elec}|j(\boldsymbol{q}_n)\rangle}{V_j^A(\boldsymbol{q}_n) - V_i^A(\boldsymbol{q}_n)}$$

Appendix C The Effects of C_S Symmetry on Coupling Terms

Eq. (29) uses the result that only orbitals with the same symmetry will have non-zero coupling terms. This can be understood by examining the form of the coupling terms within the context of C_S symmetry. As shown in Figure 1 and Figure 2, functions with A' C_S are even functions with respect to inversion of electronic coordinates while functions A'' C_S are odd functions with respect to the same inversion. An integral of an odd (A'' C_S) function over a symmetric interval about the origin is zero. In Eqs. (21) and (22) both integrals are over electronic coordinates; however, the operators $\vec{\nabla}_{q_n}$ and $\nabla^2_{q_n}$ involve derivatives with respect to nuclear coordinates. If the resulting function under the integral sign is odd, then the integral will be zero.

It can be shown that the operators $\vec{\nabla}_{q_n}$ and $\nabla^2_{q_n}$ do not change the symmetry of a function. An example of this is expressed in the following equation:

$$\vec{\nabla}_{q_n}\Phi_{\mathrm{A}'}(\boldsymbol{q}_n) = f_{\mathrm{A}'}(\boldsymbol{q}_n)$$

The expression states that a function with A' operated on by $\vec{\nabla}_{q_n}$ yields a function with A' symmetry. If $\Phi_{\mathrm{A}'}(\boldsymbol{q}_n)$ were expanded in a Taylor expansion each term of the Taylor expansion must have symmetry properties consistent with the symmetry of the entire function. A simple example of this is the sine and cosine functions. A Taylor expansion of the sine function yields only terms with odd symmetry while an expansion of the cosine functions yields only terms with even symmetry. In the case of electronic eigenstates like $\Phi_{\mathrm{A}'}(\boldsymbol{q}_n)$, a multivariable Taylor expansion will result in various products of nuclear and electronic coordinates. When the operators $\vec{\nabla}_{q_n}$ and $\nabla^2_{q_n}$ are applied to the

expansion, the electronic coordinates will be treated as constants and thus will not be affected by the operation. This means the symmetry of each term in the expansion will remain the same with respect to electronic coordinates. Thus the function resulting in the operation maintains the same symmetry properties with respect to electronic coordinates as the original eigenstate.

Given that the functions resulting from the operators $\vec{\nabla}_{q_n}$ and $\nabla^2_{q_n}$ maintain the same symmetry as the original function, it is straightforward to determine symmetry of the function being integrated in Eqs. (21) and (22). The product of two functions which both have either $A'\ C_S$ or $A''\ C_S$ will result in a function with $A'\ C_S$ symmetry and the resulting integral will be non-zero. The product of a function with $A'\ C_S$ and a function with $A''\ C_S$ will result in a function with $A''\ C_S$ and the resulting integral will be zero. Thus coupling terms involving eigenstates with different symmetry will be zero.

Appendix D The Derivation of the ADT Mixing Angle

The ADT transformation given by Eq. (31) introduced the ADT mixing angle $\gamma(\boldsymbol{q}_n)$. The mixing angle must be chosen so that the derivative couplings in the diabatic basis $\vec{\tau}_{ij}^{D}$ are negligible. The definition of derivative couplings in the adiabatic basis $\vec{\tau}_{ij}^{A}$ are given by Eq. (21) as

$$\vec{\tau}_{ij}^{A} = \int d\boldsymbol{q}_e \Phi_i^{A*}(\boldsymbol{q}_n, \boldsymbol{q}_e) \vec{\nabla}_{q_n} \Phi_j^{A}(\boldsymbol{q}_n, \boldsymbol{q}_e)$$

The functions $\Phi_i^{A*}(\boldsymbol{q}_n, \boldsymbol{q}_e)$ and $\Phi_j^{A}(\boldsymbol{q}_n, \boldsymbol{q}_e)$ will be chosen to be real-valued functions. By choosing real-valued functions, the antihermitian property of the derivative couplings (Eq. (24)) implies that diagonal DCTs are zero

$$\vec{\tau}_{ii}^{A} = \vec{\tau}_{ii}^{D} = 0$$

Furthermore, the states with $A'C_S$ symmetry will not mix with the state with $A''C_S$ symmetry. This eliminates all but the $\vec{\tau}_{12}^{A}$ and $\vec{\tau}_{21}^{A}$ DCTs which are related to each other via the antihermitian property.

First, the transformation given in Eq. (31) is inverted to yield the adiabatic states in terms of the diabatic states.

$$\Phi_{1^2A'}^{A}(\boldsymbol{q}_n, \boldsymbol{q}_e) = \Phi_{1^2A'}^{D}(\boldsymbol{q}_n, \boldsymbol{q}_e) \cos\gamma(\boldsymbol{q}_n) + \Phi_{2^2A'}^{D}(\boldsymbol{q}_n, \boldsymbol{q}_e) \sin\gamma(\boldsymbol{q}_n)$$

$$\Phi_{2^2A'}^{A}(\boldsymbol{q}_n, \boldsymbol{q}_e) = -\Phi_{1^2A'}^{D}(\boldsymbol{q}_n, \boldsymbol{q}_e) \sin\gamma(\boldsymbol{q}_n) + \Phi_{2^2A'}^{D}(\boldsymbol{q}_n, \boldsymbol{q}_e) \cos\gamma(\boldsymbol{q}_n)$$

To allow for a more compact notation the functional dependence on nuclear and electronic coordinates is assumed. These equations are inserted into Eq. (21) to yield the following integral

$$\vec{\tau}_{12}^{A} = \int dr\{\Phi_{1^2A'}^{D}\cos\gamma(\boldsymbol{q}_n) + \Phi_{2^2A'}^{D}\sin\gamma(\boldsymbol{q}_n)\}\vec{\nabla}_{q_n}\{-\Phi_{1^2A'}^{D}\sin\gamma(\boldsymbol{q}_n) + \Phi_{2^2A'}^{D}\cos\gamma(\boldsymbol{q}_n)\}$$

When multiplied out, the integral has eight terms as shown below

$$\begin{aligned}\vec{\tau}_{12}^{A} = \int dr \Big\{ & -\Phi_{1^2A'}^{D}\vec{\nabla}_{q_n}\Phi_{1^2A'}^{D}\sin\gamma(\boldsymbol{q}_n)\cos\gamma(\boldsymbol{q}_n) - \left(\Phi_{1^2A'}^{D}\right)^2\cos^2\gamma(\boldsymbol{q}_n)\left(\vec{\nabla}_{q_n}\gamma(\boldsymbol{q}_n)\right) \\ & + \left(\Phi_{1^2A'}^{D}\vec{\nabla}_{q_n}\Phi_{2^2A'}^{D}\right)\cos^2\gamma(\boldsymbol{q}_n) \\ & - \Phi_{1^2A'}^{D}\Phi_{2^2A'}^{D}\sin\gamma(\boldsymbol{q}_n)\cos\gamma(\boldsymbol{q}_n)\left(\vec{\nabla}_{q_n}\gamma(\boldsymbol{q}_n)\right) \\ & - \left(\Phi_{2^2A'}^{D}\vec{\nabla}_{q,\alpha}\Phi_{1^2A'}^{D}\right)\sin^2\gamma(\boldsymbol{q}_n) \\ & - \Phi_{1^2A'}^{D}\Phi_{2^2A'}^{D}\sin\gamma(\boldsymbol{q}_n)\cos\gamma(\boldsymbol{q}_n)\left(\vec{\nabla}_{q_n}\gamma(\boldsymbol{q}_n)\right) \\ & + \Phi_{2^2A'}^{D}\vec{\nabla}_{q,\alpha}\Phi_{2^2A'}^{D}\sin\gamma(\boldsymbol{q}_n)\cos\gamma(\boldsymbol{q}_n) \\ & - \left(\Phi_{2^2A'}^{D}\right)^2\cos^2\gamma(\boldsymbol{q}_n)\left(\vec{\nabla}_{q_n}\gamma(\boldsymbol{q}_n)\right)\Big\}\end{aligned}$$

The terms that depend only on nuclear coordinates can be pulled outside the integral. The terms $\Phi_{1^2A'}^{D}\vec{\nabla}_{q_n}\Phi_{1^2A'}^{D}$ and $\Phi_{2^2A'}^{D}\vec{\nabla}_{q_n}\Phi_{2^2A'}^{D}$ lead to diagonal DCTs when integrated and are thus zero. When the orthonormailty condition, Eq. (14), is applied terms like $\left(\Phi_{1^2A'}^{D}\right)^2$ will integrate to unity while terms like $\Phi_{1^2A'}^{D}\Phi_{2^2A'}^{D}$ will integrate to zero. When these simplifications are made the expression above becomes

$$\begin{aligned}\vec{\tau}_{12}^{A} = & -\cos^2\gamma(\boldsymbol{q}_n)\left(\vec{\nabla}_{q_n}\gamma(\boldsymbol{q}_n)\right) + \cos^2\gamma(\boldsymbol{q}_n)\,\vec{\tau}_{12}^{D} - \sin^2\gamma(\boldsymbol{q}_n)\,\vec{\tau}_{21}^{D} \\ & - \sin^2\gamma(\boldsymbol{q}_n)\left(\vec{\nabla}_{q_n}\gamma(\boldsymbol{q}_n)\right)\end{aligned}$$

After using the antihermitian property of the DCTs and applying standard trigonometric identities the expression simplifies to

$$\vec{\tau}_{12}^{A} = -\cos^2\gamma(\boldsymbol{q}_n) = -\vec{\nabla}_{q_n}\gamma(\boldsymbol{q}_n) + \vec{\tau}_{12}^{D}$$

Thus when $\vec{\tau}_{12}^{D}$ is set to zero Eq. (34) is obtained.

$$\vec{\nabla}_{q_n}\gamma(\boldsymbol{q}_n) = -\vec{\tau}_{12}^{A}$$

The equation gives rise to the line integral, Eq. (35), yielding the ADT mixing angle $\gamma(\boldsymbol{q}_n)$ for each nuclear configuration.

Appendix E The Symmetry of the Electrostatic Interaction Potential

The symmetry of the H_2 molecule influences the structure of the electrostatic interaction potential when represented in the asymptotic basis. Because H_2 is a homonuclear diatomic molecule, when considering H_2 in the BF frame with the Jacobi coordinate θ, all functions containing this variable must have the property $f(\pi - \theta) = f(\theta)$. Thus when considering the diabatic PESs V_{xx} , V_{yy}, and V_{zz} given by Eqs. (88) only expansion coefficients $V_{\lambda_r \lambda_a \mu}(r, R)$ where λ_r is even will be non-zero. The coefficients for odd values of λ_r vanish due to the following propery of the reduced Wigner rotation matrix elements[26]:

$$d^{\lambda_r}_{\mu 0}(\pi - \theta) = (-1)^{\mu + \lambda_r} d^{\lambda_r}_{\mu 0}(\theta)$$

For V_{xx} , V_{yy}, and V_{zz}, μ is either 0 or 1. Thus when λ_r is odd the sum $\mu + \lambda_r$ is also odd causing a change in polarity.

Similarly, the coefficients for odd values of λ_r for V_{xy} will also vanish due to the requirement that V_{xy} vanish when $\theta = \pi/2$. This requirement is a consquence of the polarity of the boron $2p$ orbitals coupled by V_{xy}. As described in detail by Alexander[26], the sign of V_{xy} will flip as $\theta \to \pi - \theta$. Given that μ is unity for V_{xy}, odd values of λ_r lead to an even sum $\mu + \lambda_r$. This does not change the polarity as required. Therefore, all expansion coefficients for odd λ_r vanish for V_{xy} as well.

Knowing that λ_r will on take on even values, the property of 3-j symbols described by Eq. (81) will determine which angular momentum states j couple with one another. Since λ_r will always be even, j' and j must both be either odd or even for to

have a non-zero expansion coefficient. As a result, there are two subsets of states: even valued j states, and odd valued j states. States from one of these subsets will not couple with a state in the other subset. Therefore, states with even and odd j can be considered separately.[91] States with even values of j correspond to parahydrogen and odd values correspond to orthohydrogen. For this work only parahydrogen states are considered. This reduces the number of states that can be included in the basis due to the desire to keep the rotational energy below the energy required to excite the first vibrational mode of the H_2 molecule.

Appendix F The Adiabatic PESs of B + H_2

In this section the adiabatic PESs of the B + H_2 system are presented for the configurations with C_{2v} symmetry ($\theta = \pi/2$) and $C_{\infty h}$ symmetry ($\theta = 0$). The PESs are presented as a function of r and R. Each surface is rendered in a 2D color plot which captures the entire surface at-a-glance. Each 2D plot is accompanied by a 3D rendering to assist in visualizing the shape of the surface. The PESs were rendered on a grid 601 x 601 points using cubic spline interpolation. For energy values greater than 0.2707 au the PESs display wavy features caused by ringing from the cubic spline interpolation. The PES values were mapped to a color palette containing 200 values with bins ranging from the minimum value of the PES to the maximum value. The color scale of the 2D and 3D renderings are identical for a given PES orientation. The figures begin on the next page.

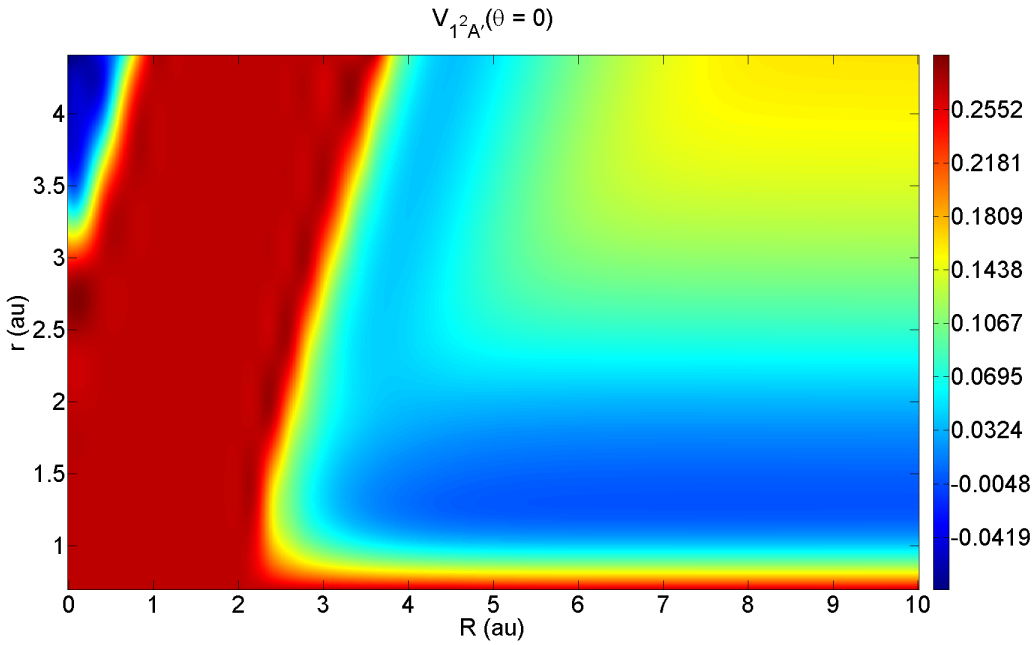

Figure 46. The 2D color rendering of the adiabatic PES $V_{1^2A'}(\theta = 0)$

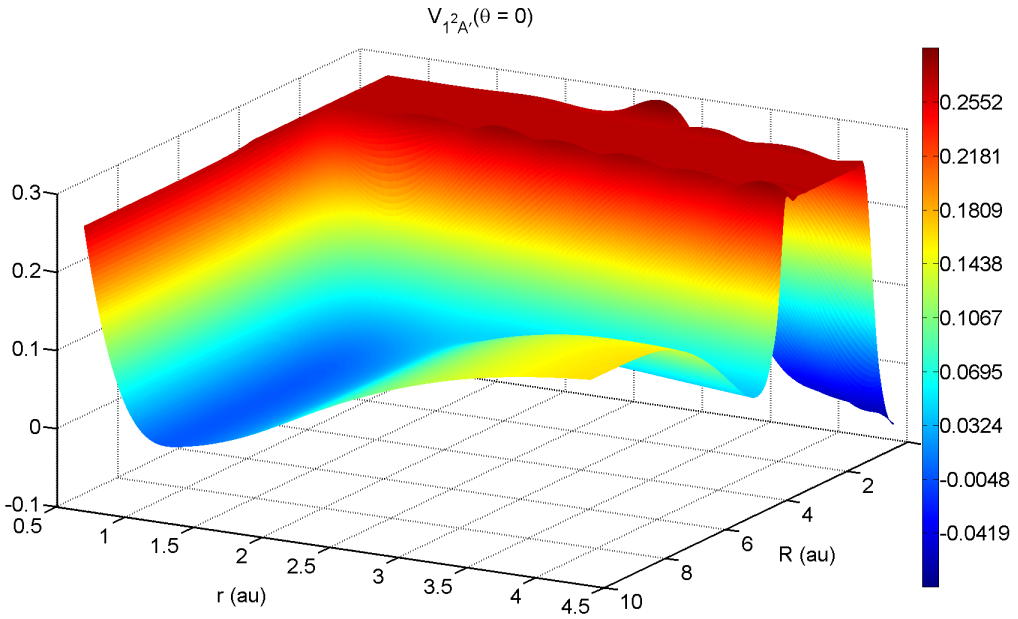

Figure 47. The 3D rendering of the adiabatic PES $V_{1^2A'}(\theta = 0)$

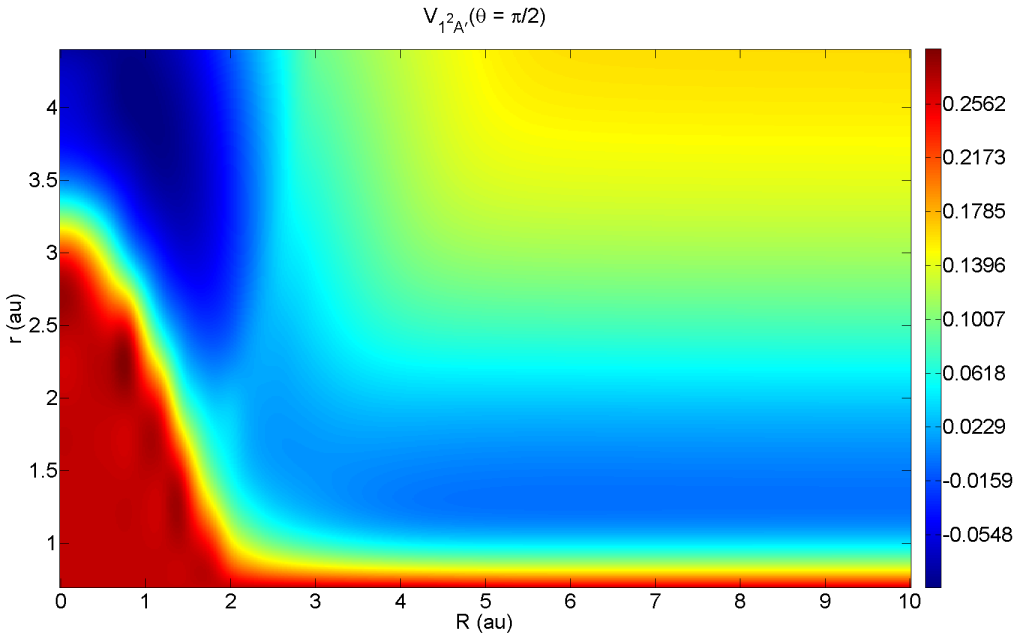

Figure 48. The 2D color rendering of the adiabatic PES $V_{1^2A'}(\theta = \pi/2)$

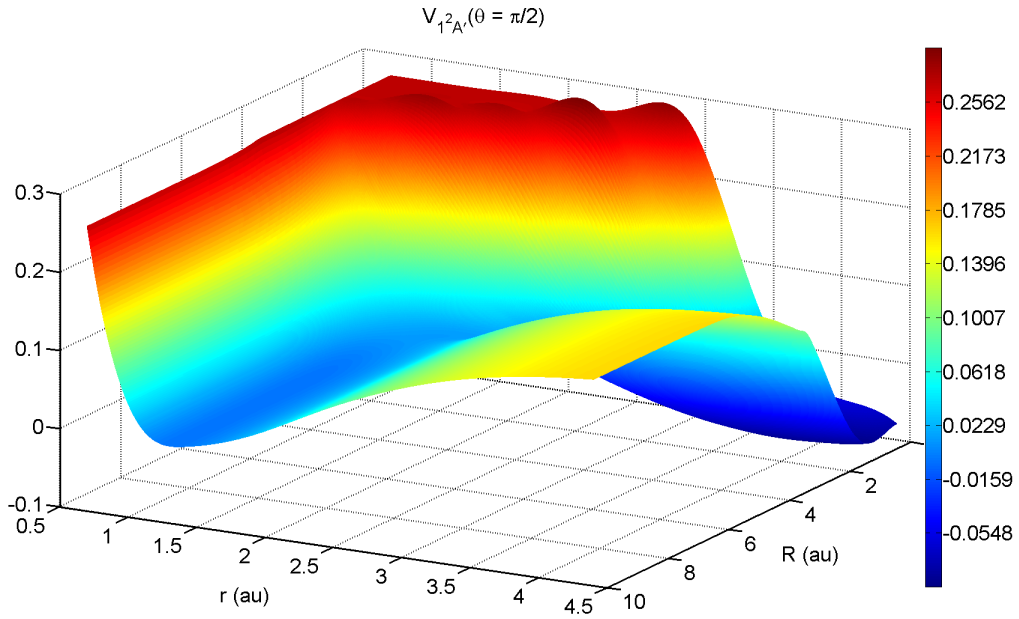

Figure 49. The 3D rendering of the adiabatic PES $V_{1^2A'}(\theta = \pi/2)$

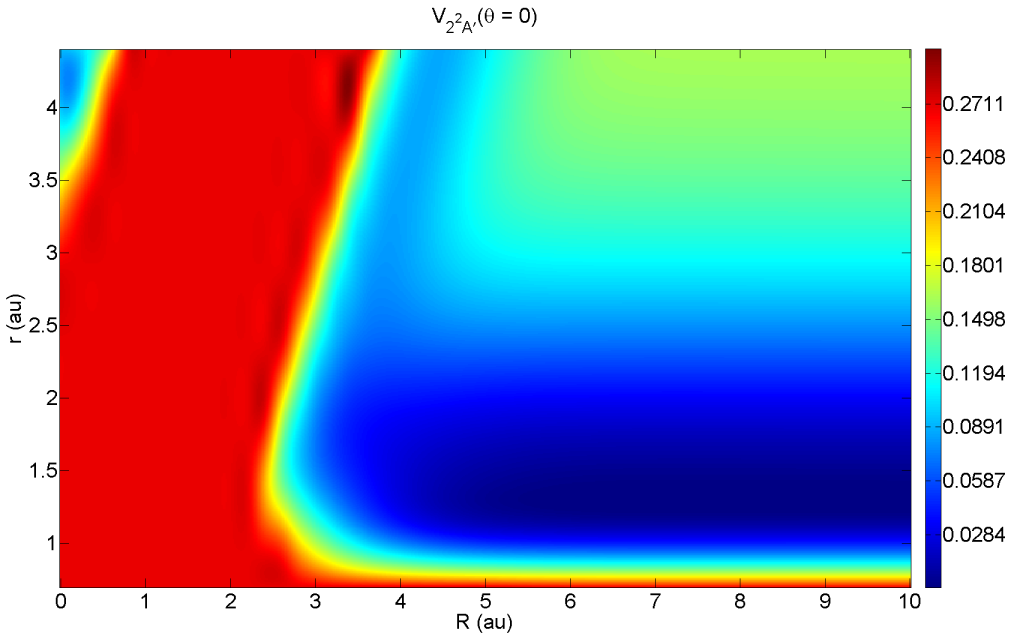

Figure 50. The 2D color rendering of the adiabatic PES $V_{2^2A'}(\theta = 0)$

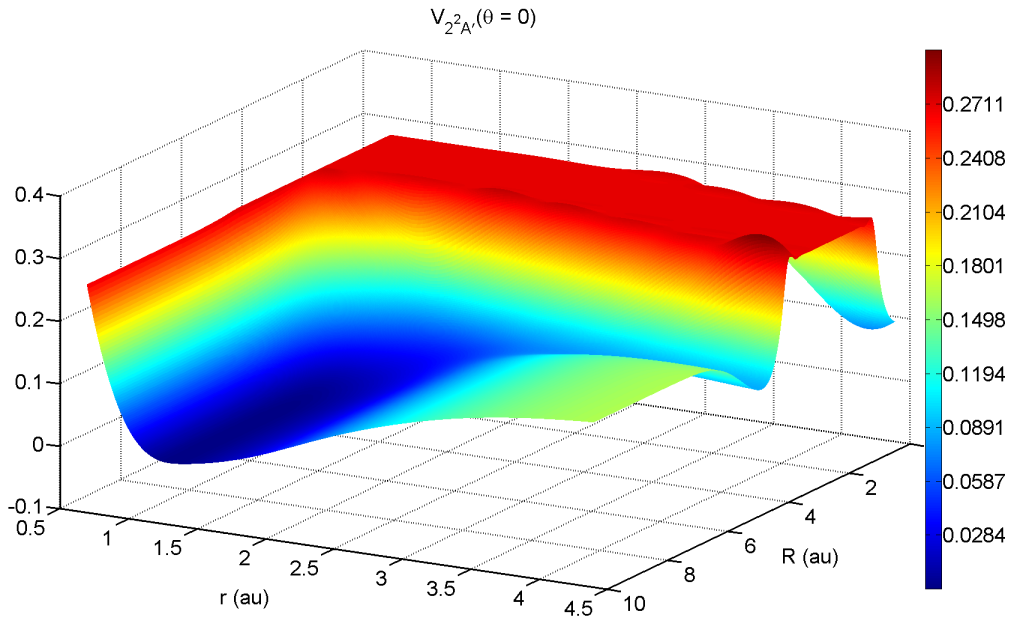

Figure 51. The 3D rendering of the adiabatic PES $V_{2^2A'}(\theta = 0)$

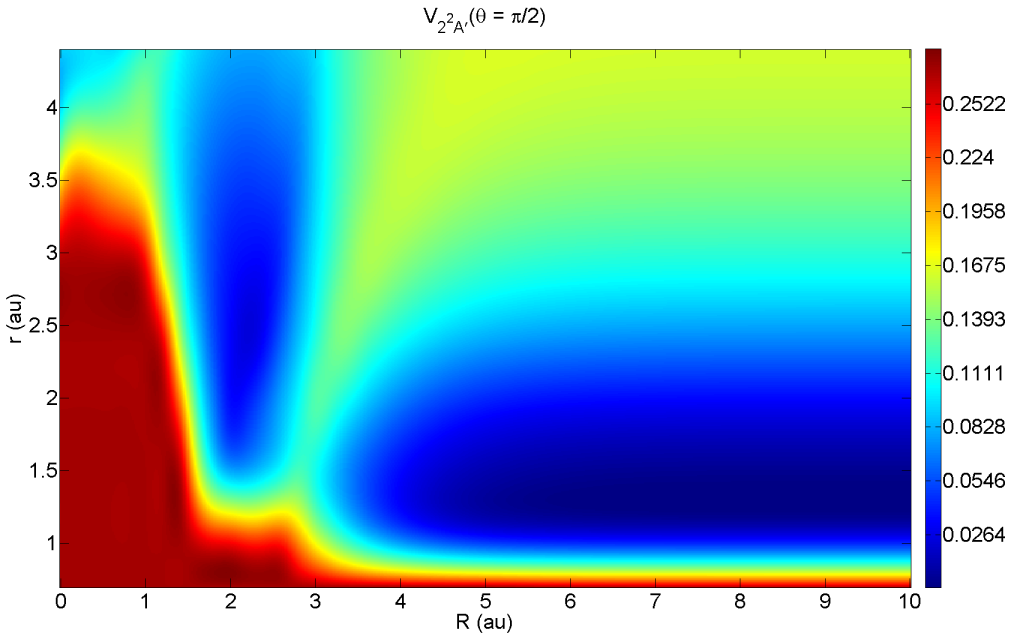

Figure 52. The 2D color rendering of the adiabatic PES $V_{2^2A'}(\theta = \pi/2)$

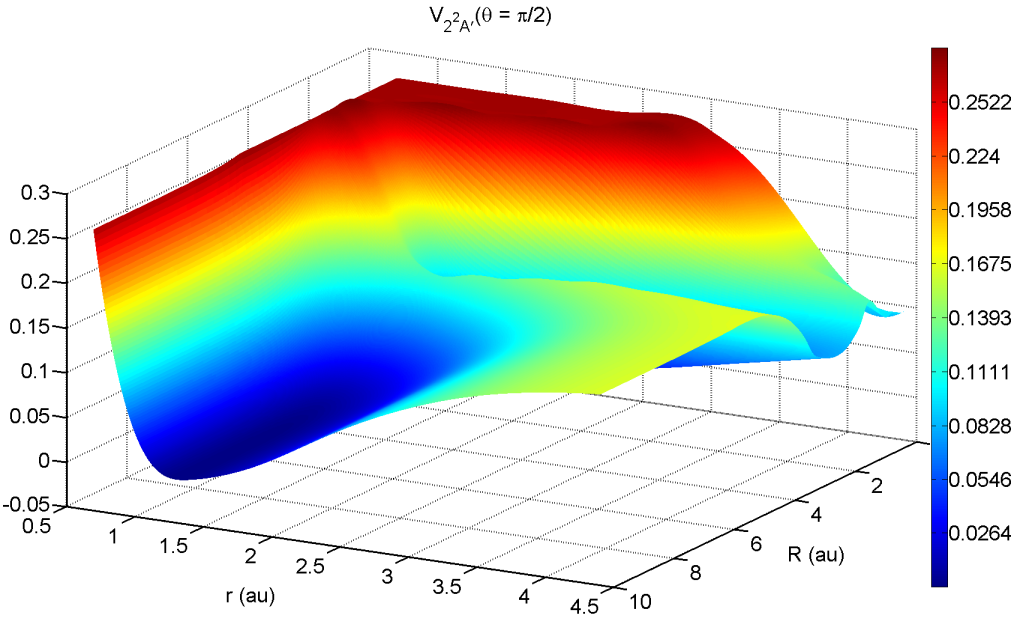

Figure 53. The 3D rendering of the adiabatic PES $V_{2^2A'}(\theta = \pi/2)$

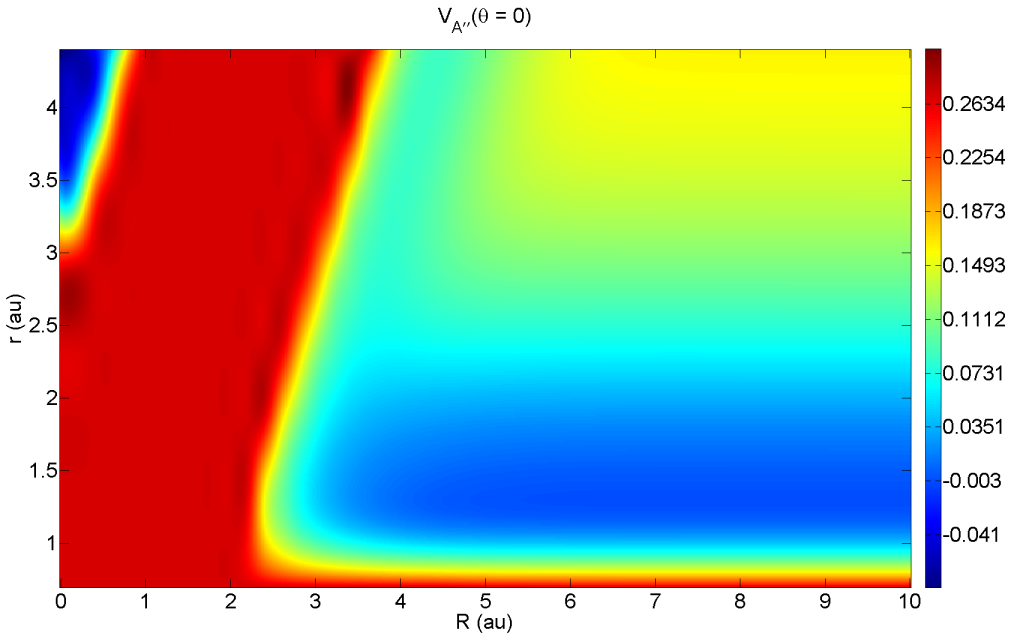

Figure 54. The 2D color rendering of the adiabatic PES $V_{A''}(\theta = 0)$

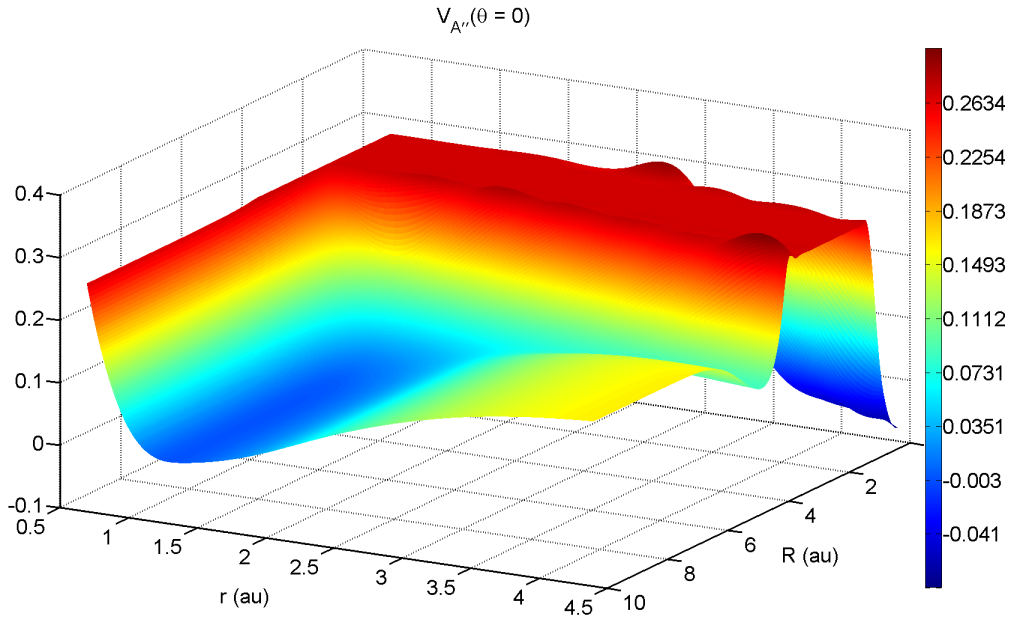

Figure 55. The 3D rendering of the adiabatic PES $V_{A''}(\theta = 0)$

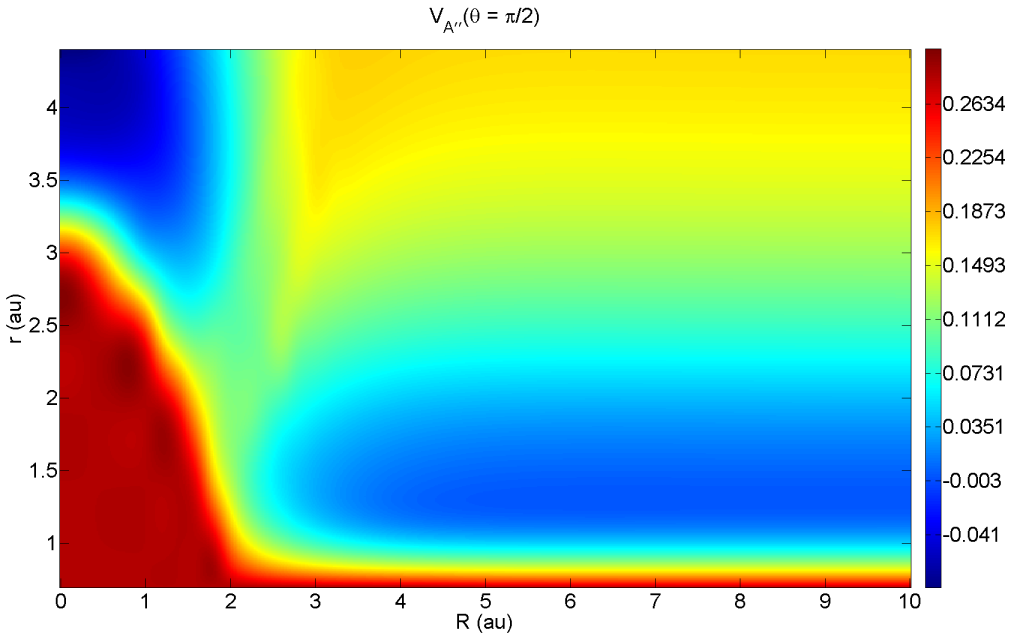

Figure 56. The 2D color rendering of the adiabatic PES $V_{A''}(\theta = \pi/2)$

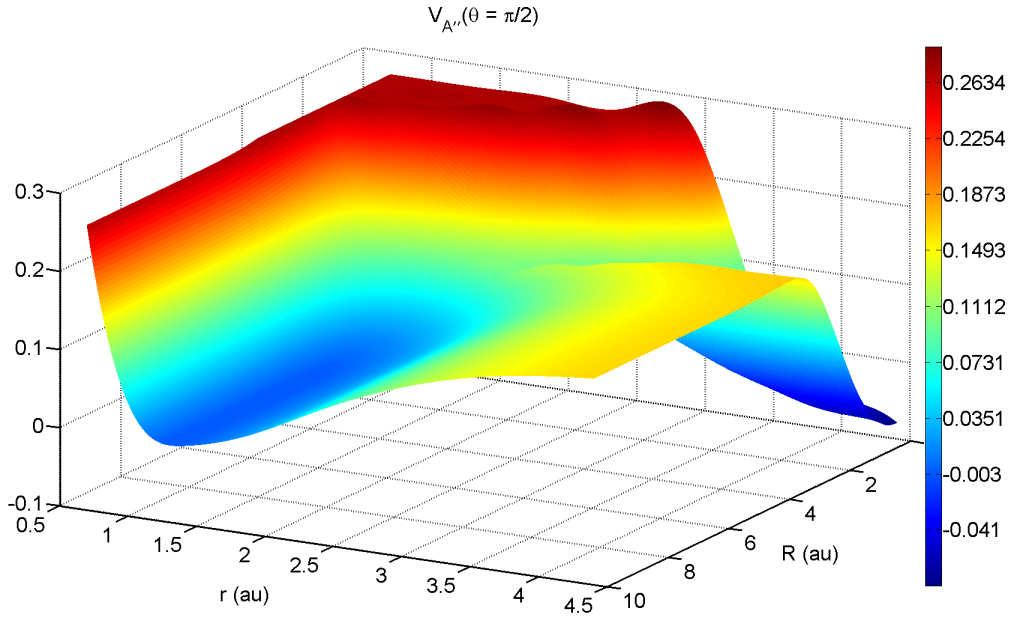

Figure 57. The 3D rendering of the adiabatic PES $V_{A''}(\theta = \pi/2)$

Appendix G The Derivative Coupling Surfaces of B + H_2

In this section the components of the derivative coupling vector field are displayed as a function of r and R for $\theta = \pi/20$. To illustrate the jagged features that can exist in DCTs no attempt is made to interpolate these surfaces.

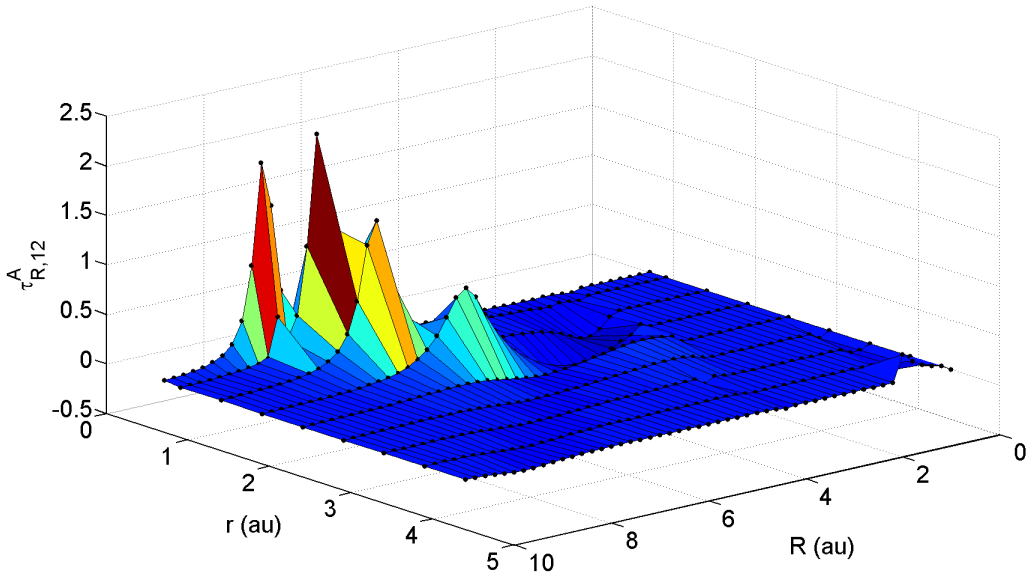

Figure 58. The derivative coupling surface for the component $\tau^A_{R,12}$ for $\theta = \pi/20$

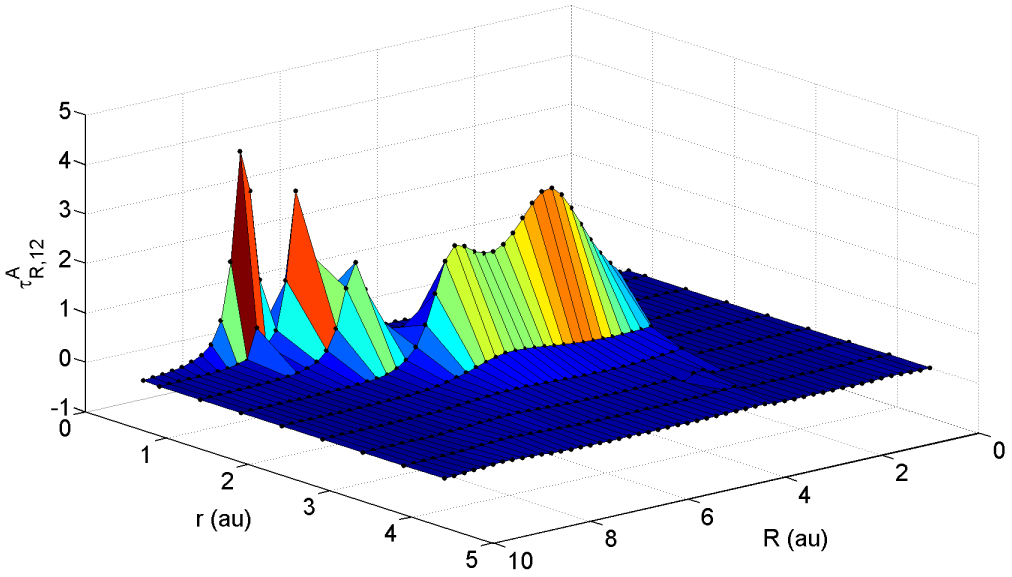

Figure 59. The derivative coupling surface for the component $\tau^A_{r,12}$ for $\theta = \pi/20$

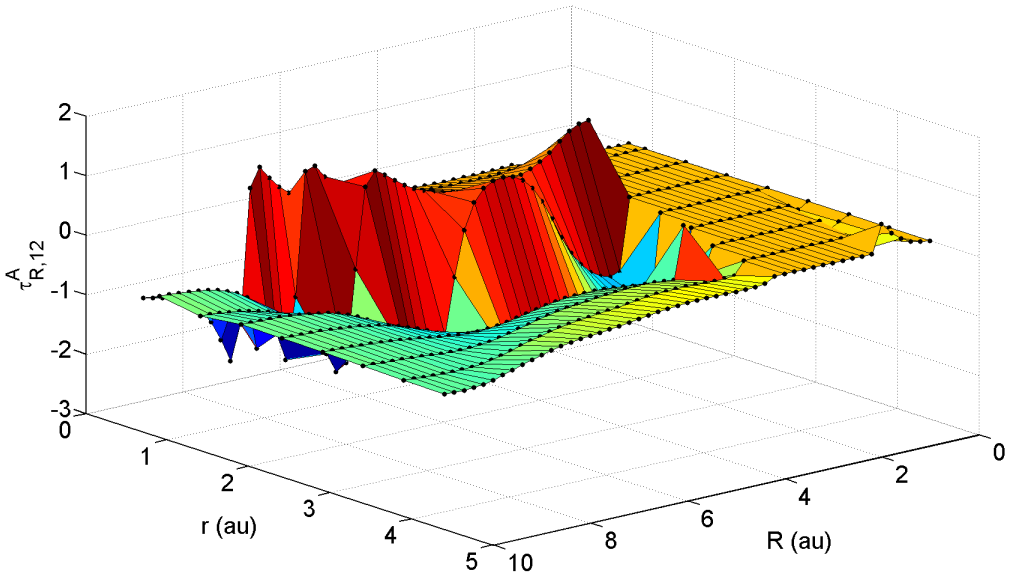

Figure 60. The derivative coupling surface for the component $\tau^A_{\theta,12}$ for $\theta = \pi/20$

Appendix H The Diabatic PESs of B + H_2

In this section the diabatic PESs of the B + H_2 system are presented for $\theta = \pi/4$. The PESs are presented as a function of r and R. Due to the symmetry derived boundary conditions, diabatic PESs for the configurations with C_{2v} symmetry ($\theta = \pi/2$) and $D_{\infty h}$ symmetry ($\theta = 0$) are identical to their adiabatic counterparts. The diabatic coupling surface V_{xz} is zero for these configurations as well. Furthermore, the single surface with A'' C_S symmetry does not mix with other surfaces. As a result the adiabatic $V_{A''}$ and diabatic V_{yy} PES are equal.

Each surface is rendered in a 2D color plot which captures the entire surface at-a-glance. Each 2D plot is accompanied by a 3D rendering to assist in visualizing the shape of the surface. The PESs were rendered on a grid 601 x 601 points using cubic spline interpolation. For energy values greater than 0.2707 au the PESs display wavy features caused by ringing from the cubic spline interpolation. The PES values were mapped to a color palette containing 200 values with bins ranging from the minimum value of the PES to the maximum value. The color scale of the 2D and 3D renderings are identical for a given PES orientation. The figures begin on the next page.

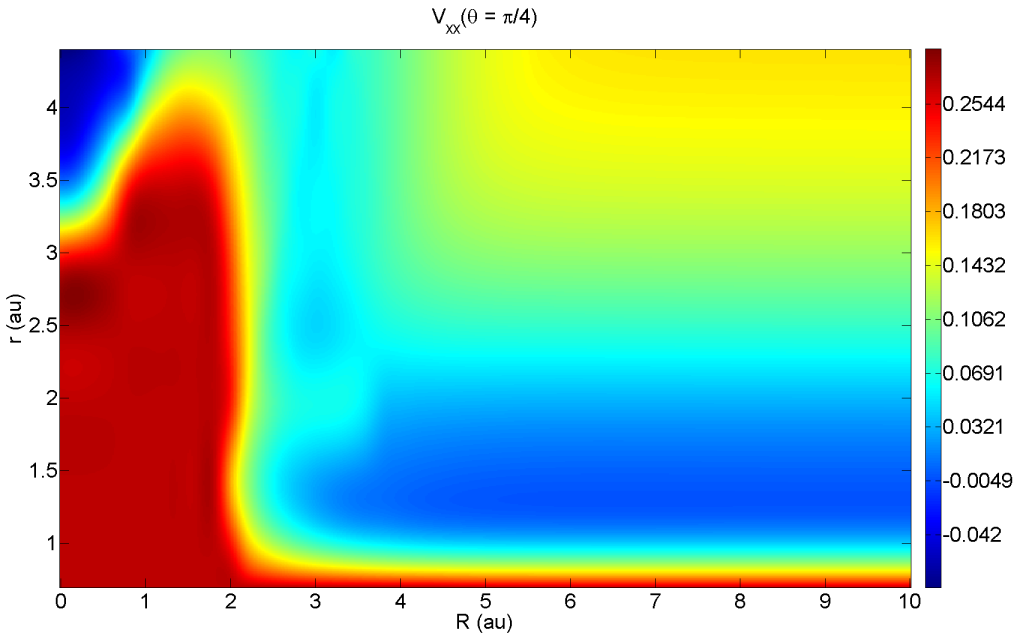

Figure 61. The 2D color rendering of the diabatic PES $V_{xx}(\theta = \pi/4)$

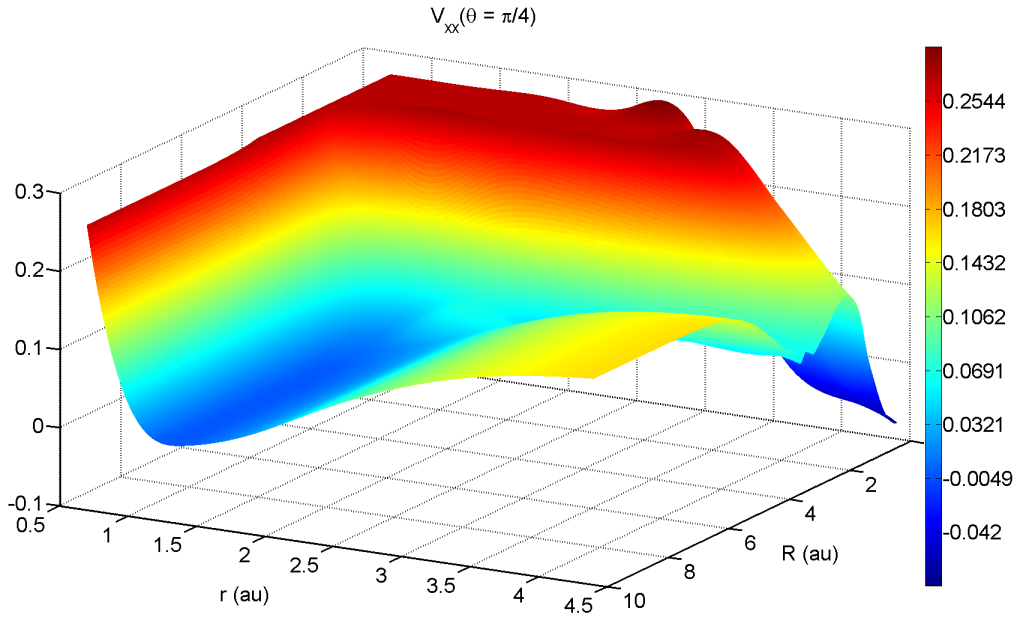

Figure 62. The 3D rendering of the diabatic PES $V_{xx}(\theta = \pi/4)$

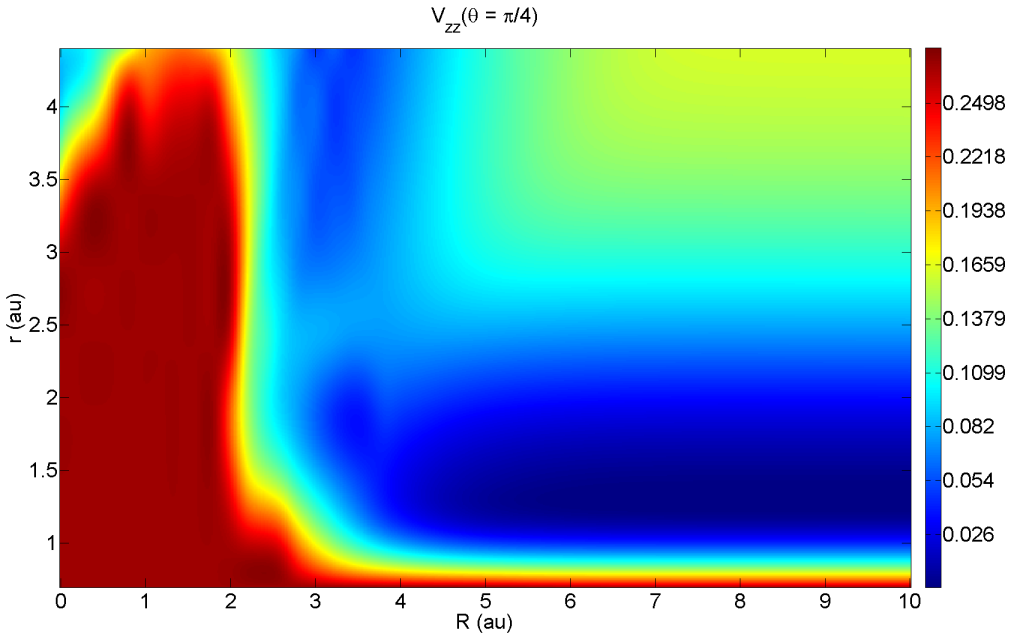

Figure 63. The 2D color rendering of the diabatic PES $V_{zz}(\theta = \pi/4)$

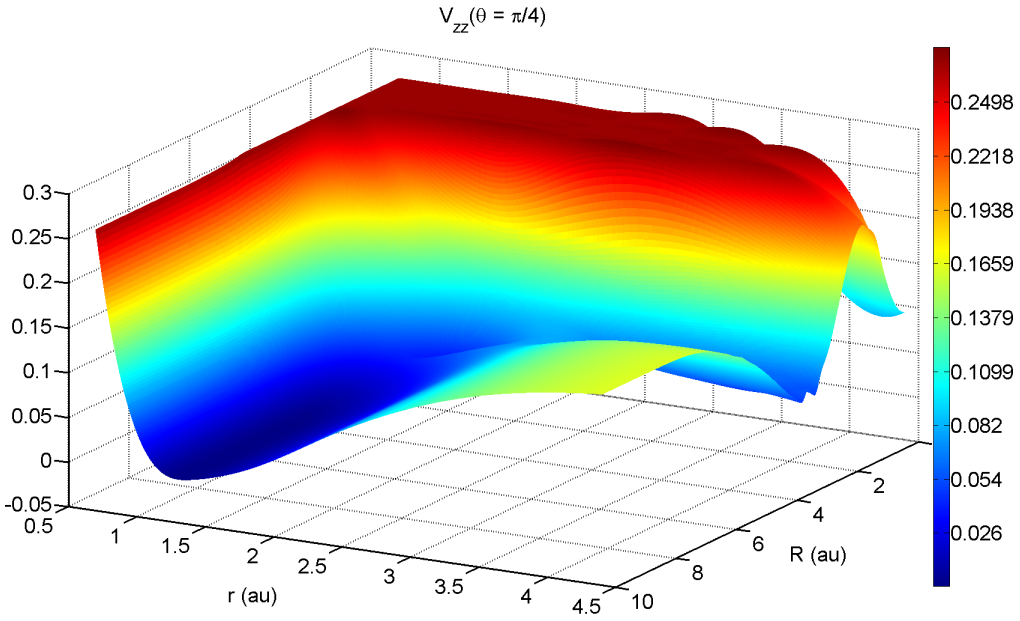

Figure 64. The 3D rendering of the diabatic PES $V_{zz}(\theta = \pi/4)$

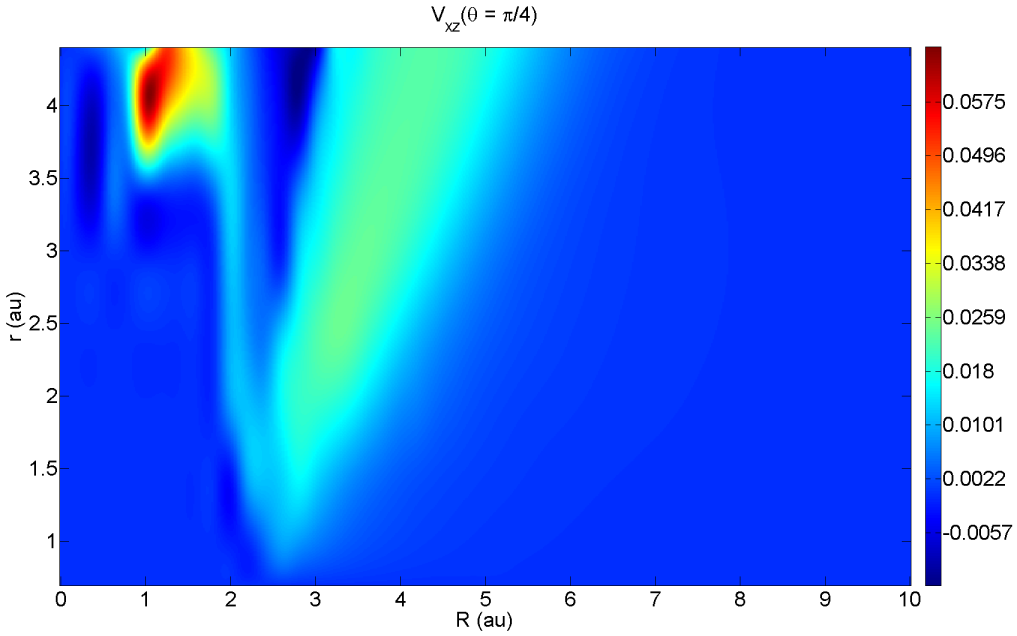

Figure 65. The 2D color rendering of the diabatic PES $V_{xz}(\theta = \pi/4)$

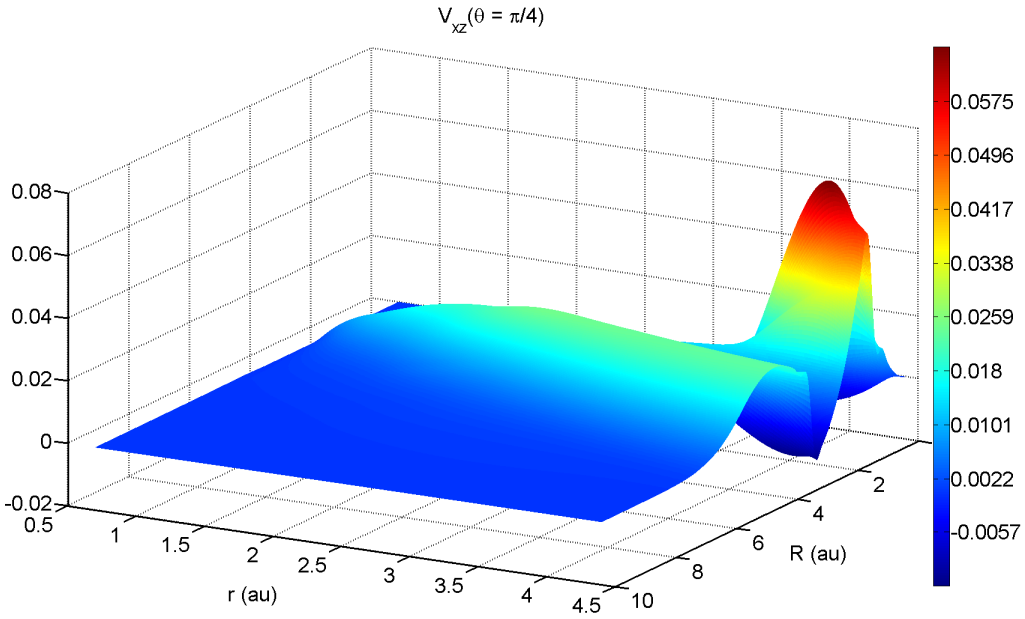

Figure 66. The 3D rendering of the diabatic PES $V_{xz}(\theta = \pi/4)$

Appendix I The Diabatic Effective PESs of B + H_2

In this section a selection of diabatic effective PESs of the B + H_2 system are presented. The PESs are presented as a function of r and R. Each surface is rendered in a 2D color plot which captures the entire surface at-a-glance. Each 2D plot is accompanied by a 3D rendering to assist in visualizing the shape of the surface. The PESs were rendered on a grid 601 x 601 points using cubic spline interpolation. For energy values greater than 0.2707 au the PESs display wavy features caused by ringing from the cubic spline interpolation. The PES values were mapped to a color palette containing 200 values with bins ranging from the minimum value of the PES to the maximum value. The color scale of the 2D and 3D renderings are identical for a given PES orientation. The figures begin on the next page.

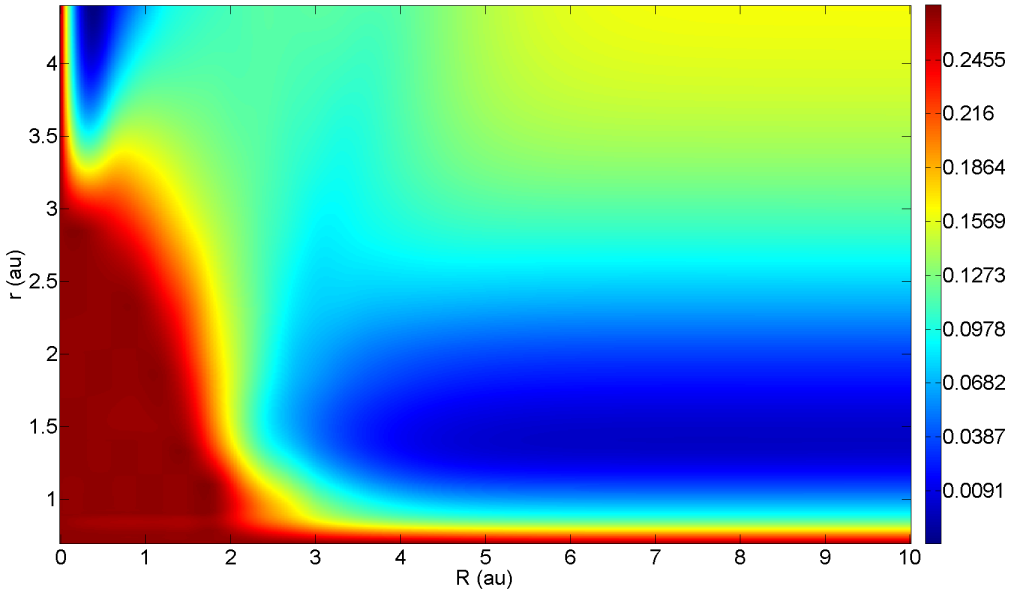

Figure 67. The 2D color rendering of the diabatic effective PES $\left\langle 0,0,\frac{1}{2},\frac{1}{2}\middle|V_{eff}^{D}\middle|0,0,\frac{1}{2},\frac{1}{2}\right\rangle$

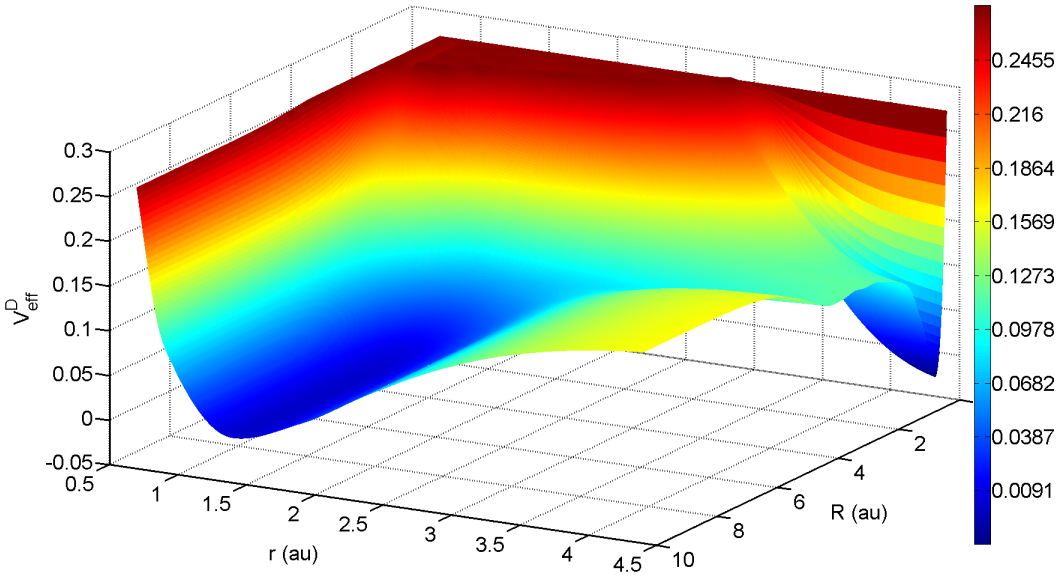

Figure 68. The 3D rendering of the diabatic effective PES $\left\langle 0,0,\frac{1}{2},\frac{1}{2}\middle|V_{eff}^{D}\middle|0,0,\frac{1}{2},\frac{1}{2}\right\rangle$

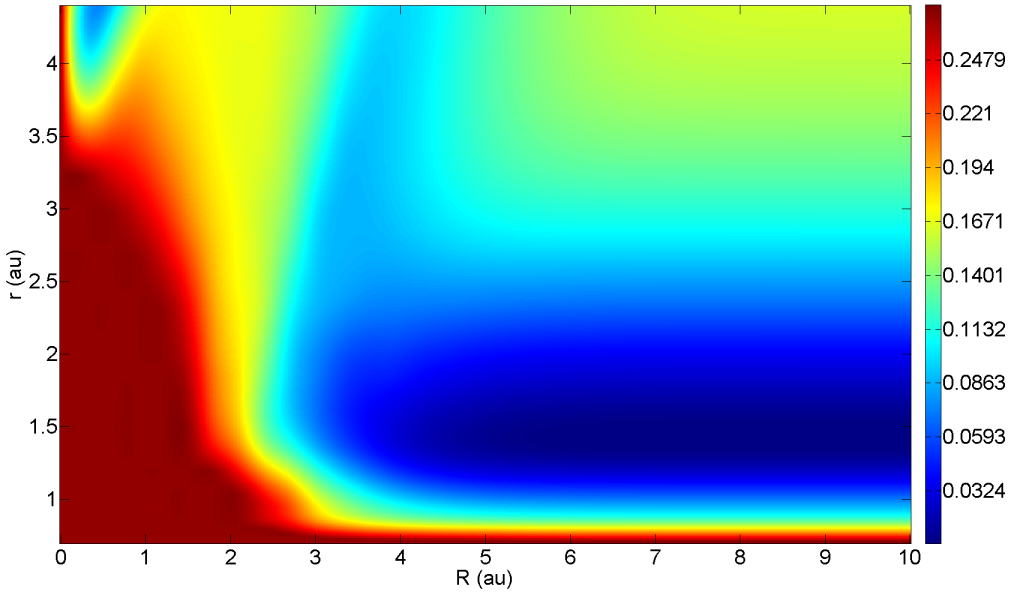

Figure 69. The 2D color rendering of the diabatic effective PES $\left\langle 4,1,\frac{3}{2},\frac{-1}{2}\middle|V_{eff}^{D}\middle|4,1,\frac{3}{2},\frac{-1}{2}\right\rangle$

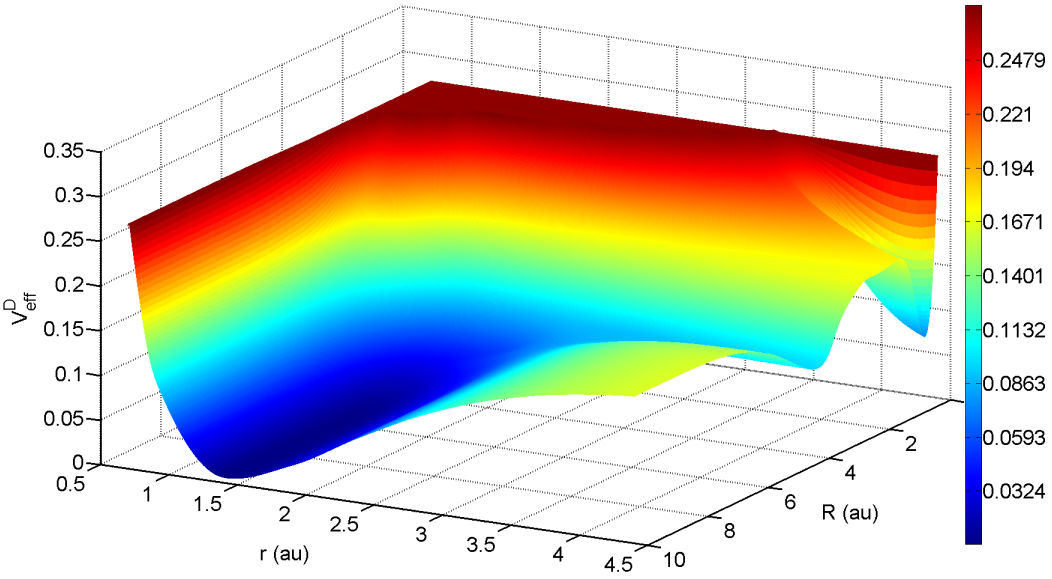

Figure 70. The 3D rendering of the diabatic effective PES $\left\langle 4,1,\frac{3}{2},\frac{-1}{2}\middle|V_{eff}^{D}\middle|4,1,\frac{3}{2},\frac{-1}{2}\right\rangle$

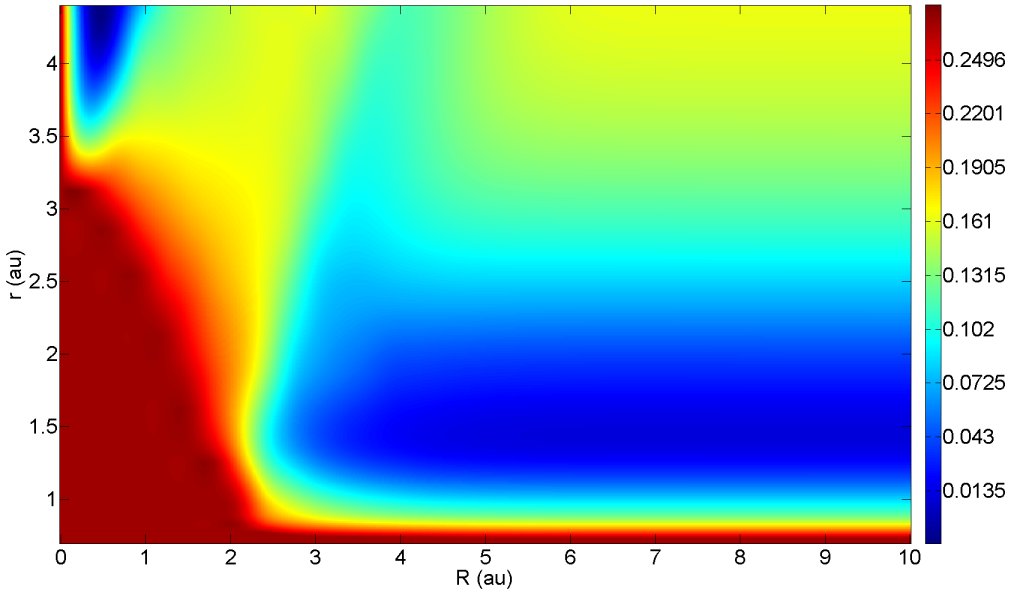

Figure 71. The 2D color rendering of the diabatic effective PES $\left\langle 6,-1,\frac{3}{2},\frac{3}{2}\middle|V_{eff}^{D}\middle|6,-1,\frac{3}{2},\frac{3}{2}\right\rangle$

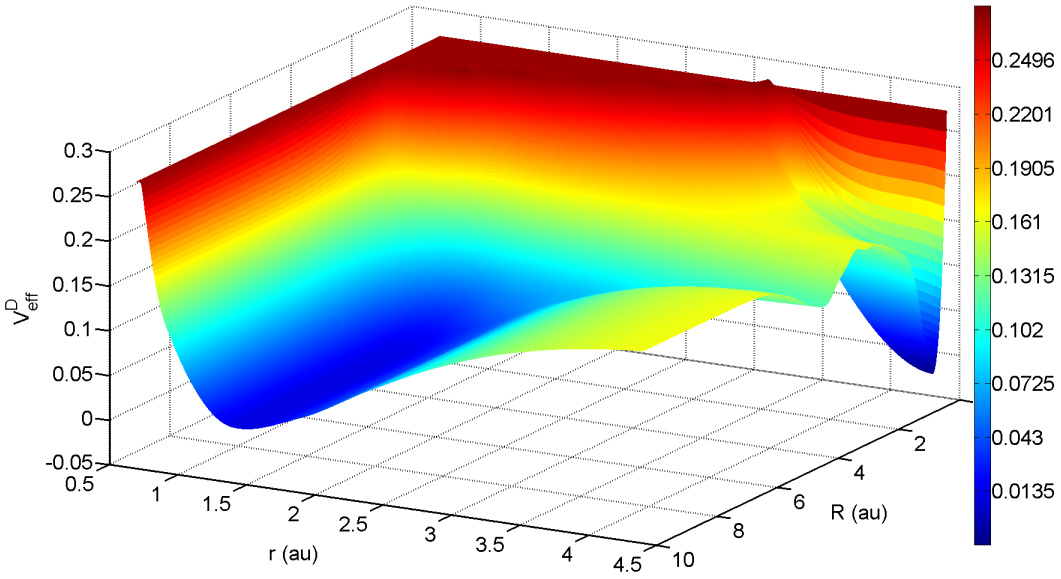

Figure 72. The 3D rendering of the diabatic effective PES $\left\langle 6,-1,\frac{3}{2},\frac{3}{2}\middle|V_{eff}^{D}\middle|6,-1,\frac{3}{2},\frac{3}{2}\right\rangle$

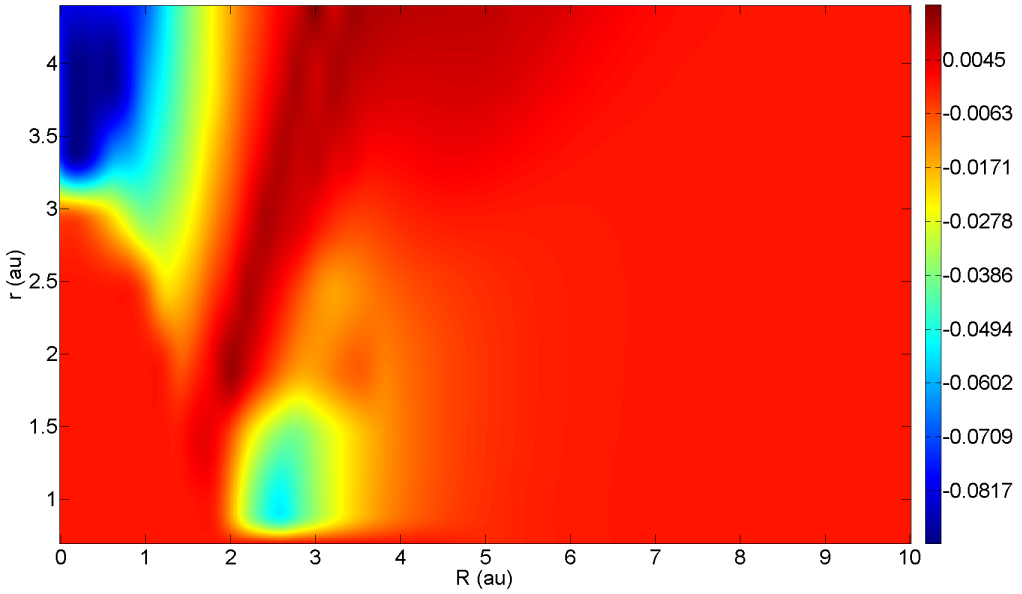

Figure 73. The 2D color rendering of the diabatic effective PES $\left\langle 0,0,\frac{1}{2},\frac{1}{2}\middle|V_{eff}^{D}\middle|0,0,\frac{3}{2},\frac{1}{2}\right\rangle$

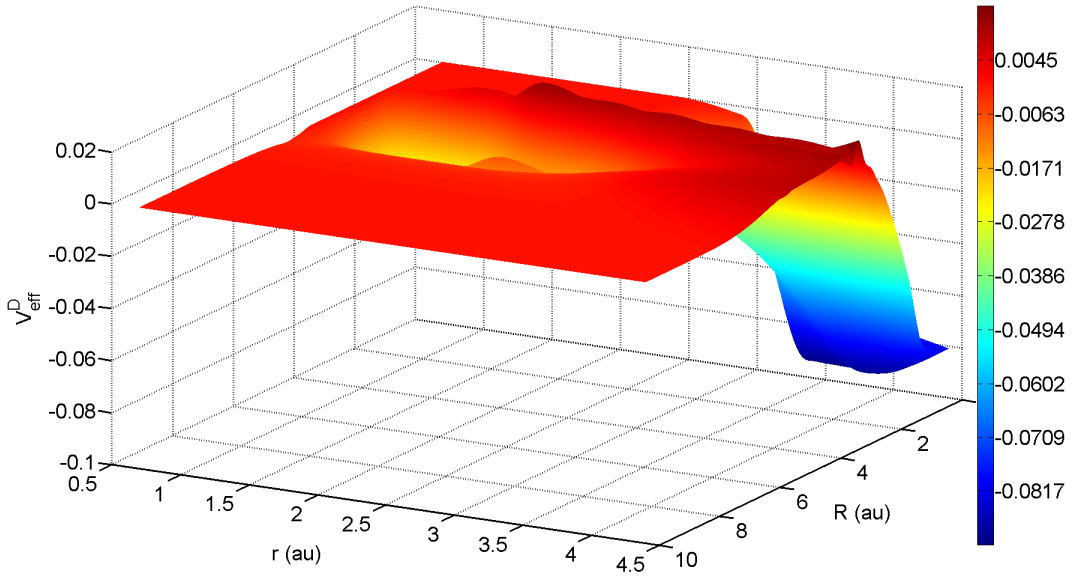

Figure 74. The 3D rendering of the diabatic effective PES $\left\langle 0,0,\frac{1}{2},\frac{1}{2}\middle|V_{eff}^{D}\middle|0,0,\frac{3}{2},\frac{1}{2}\right\rangle$

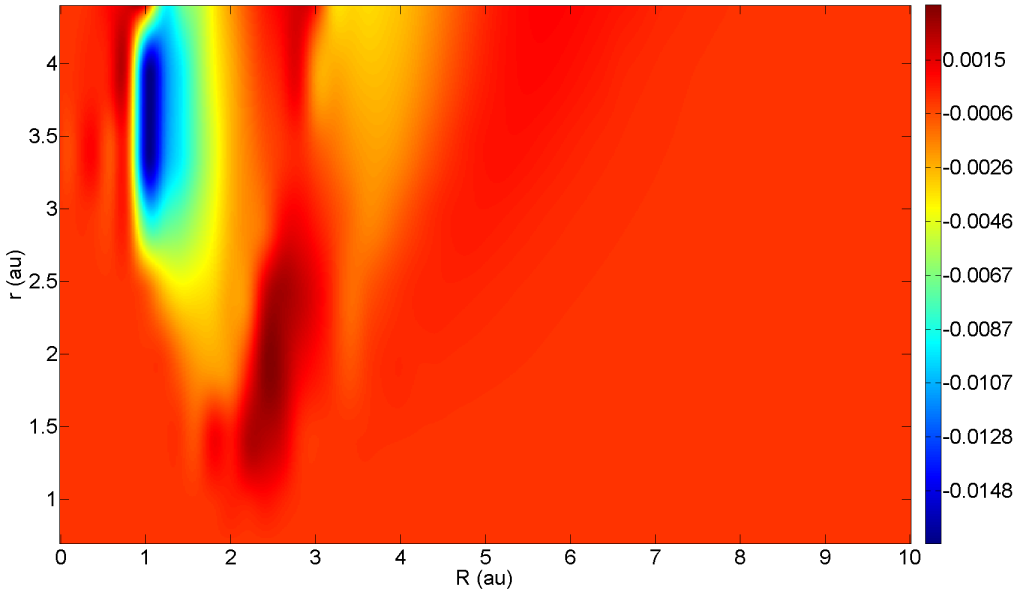

Figure 75. The 2D color rendering of the diabatic effective PES $\left\langle 0,0,\frac{1}{2},\frac{1}{2}\middle|V_{eff}^{D}\middle|4,1,\frac{3}{2},\frac{-1}{2}\right\rangle$

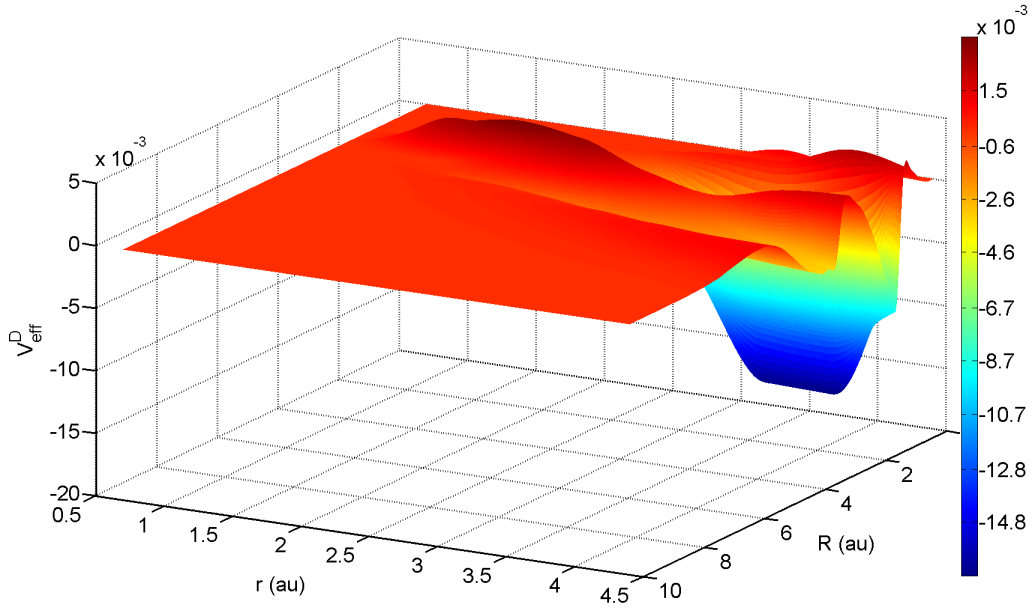

Figure 76. The 3D rendering of the diabatic effective PES $\left\langle 0,0,\frac{1}{2},\frac{1}{2}\middle|V_{eff}^{D}\middle|4,1,\frac{3}{2},\frac{-1}{2}\right\rangle$

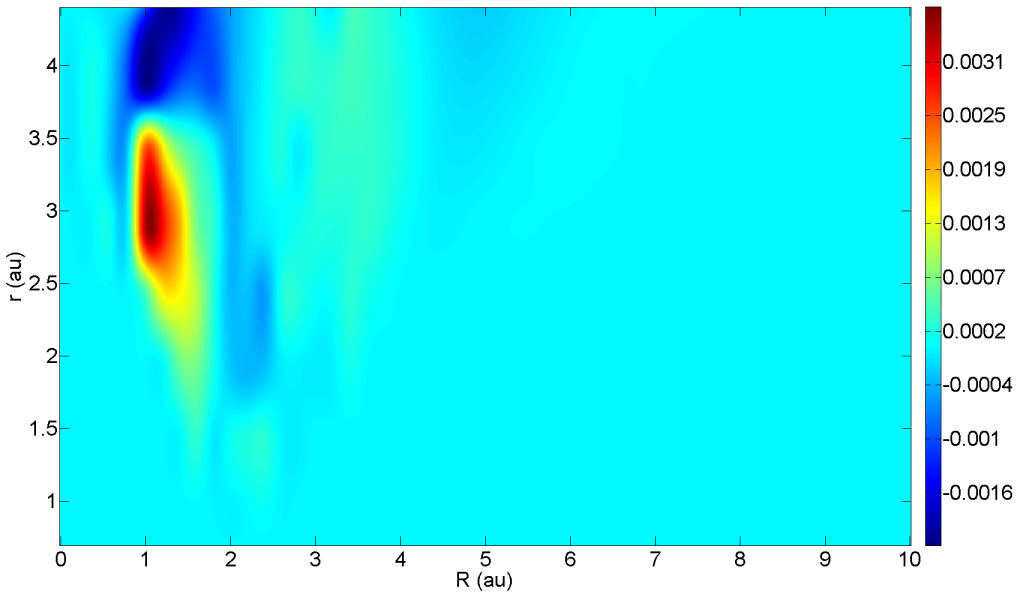

Figure 77. The 2D color rendering of the diabatic effective PES $\left\langle 0,0,\frac{1}{2},\frac{1}{2}\middle|V_{eff}^{D}\middle|6,-1,\frac{3}{2},\frac{3}{2}\right\rangle$

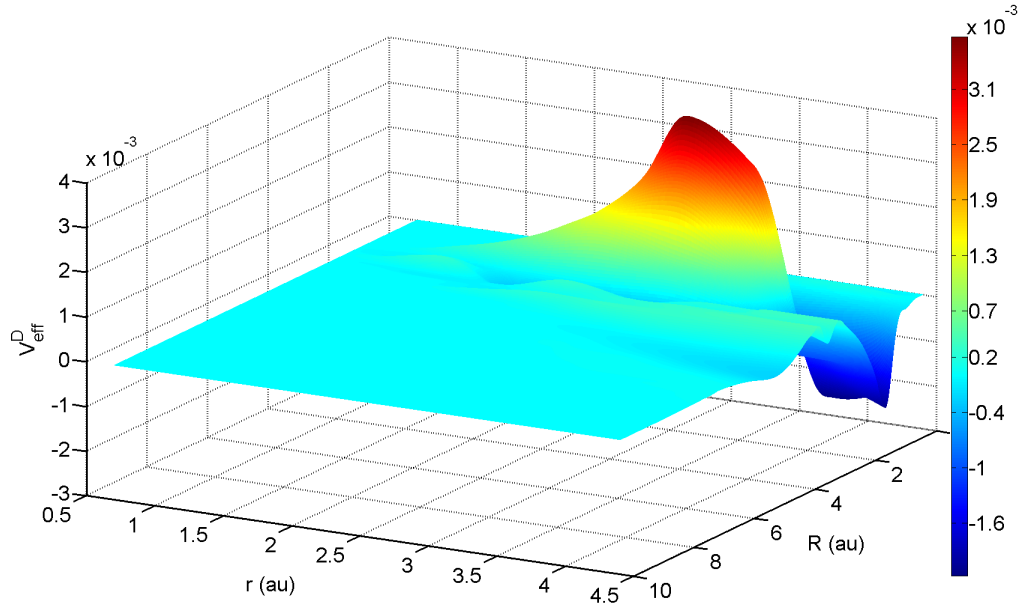

Figure 78. The 3D rendering of the diabatic effective PES $\left\langle 0,0,\frac{1}{2},\frac{1}{2}\middle|V_{eff}^{D}\middle|6,-1,\frac{3}{2},\frac{3}{2}\right\rangle$

Appendix J The Adiabatic Effective PESs of B + H_2

In this section a selection of adiabatic effective PESs of the B + H_2 system are presented. The PESs are presented as a function of r and R. Each surface is rendered in a 2D color plot which captures the entire surface at-a-glance. Each 2D plot is accompanied by a 3D rendering to assist in visualizing the shape of the surface. The PESs were rendered on a grid 601 x 601 points using cubic spline interpolation. For energy values greater than 0.2707 au the PESs display wavy features caused by ringing from the cubic spline interpolation. The PES values were mapped to a color palette containing 200 values with bins ranging from the minimum value of the PES to the maximum value. The color scale of the 2D and 3D renderings are identical for a given PES orientation. The figures begin on the next page.

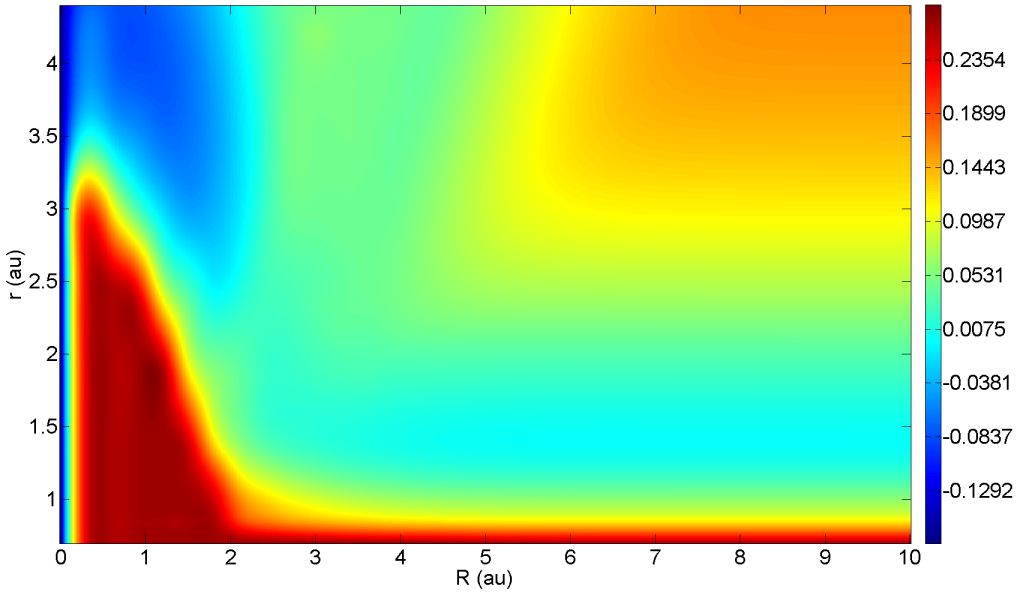

Figure 79. The 2D color rendering of the first adiabatic effective PES

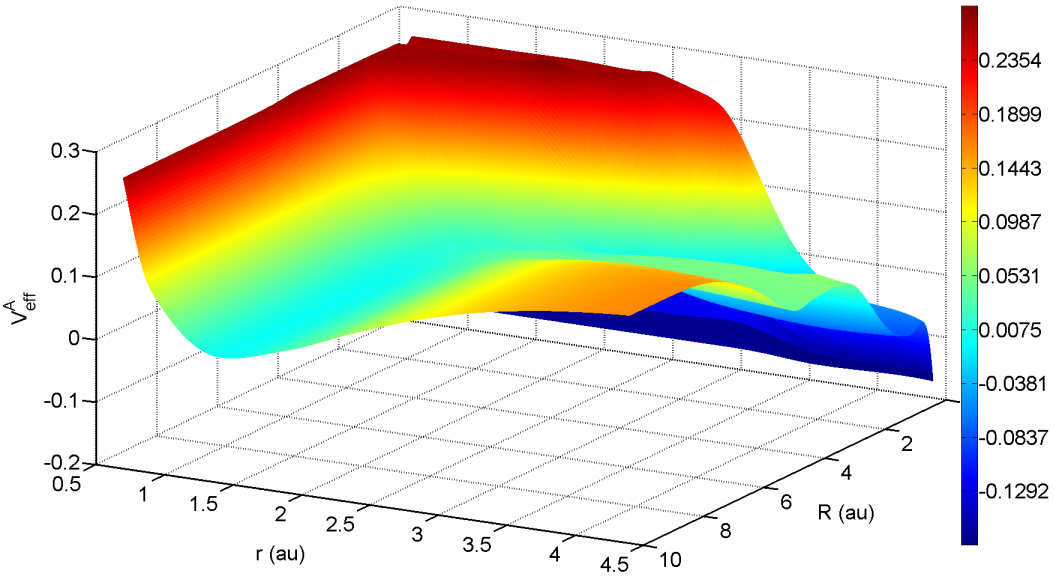

Figure 80. The 3D rendering of the first adiabatic effective PES

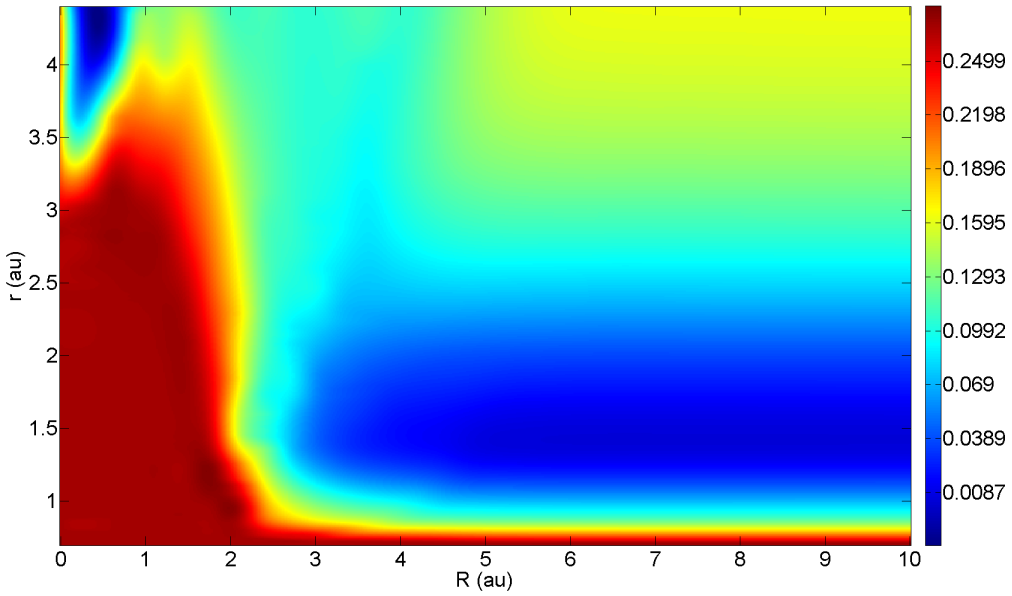

Figure 81. The 2D color rendering of the 10th adiabatic effective PES

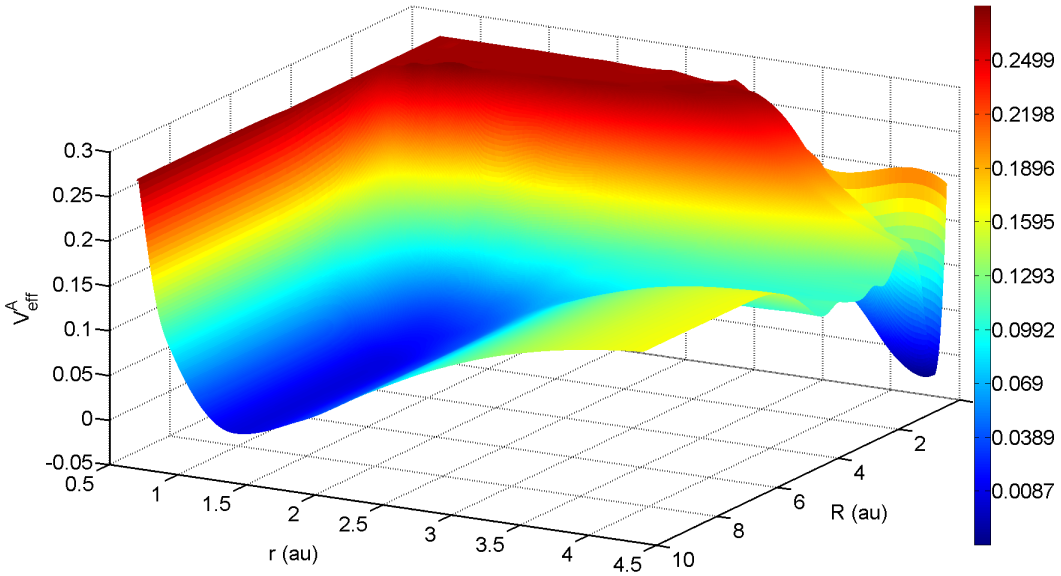

Figure 82. The 3D rendering of the 10th adiabatic effective PES

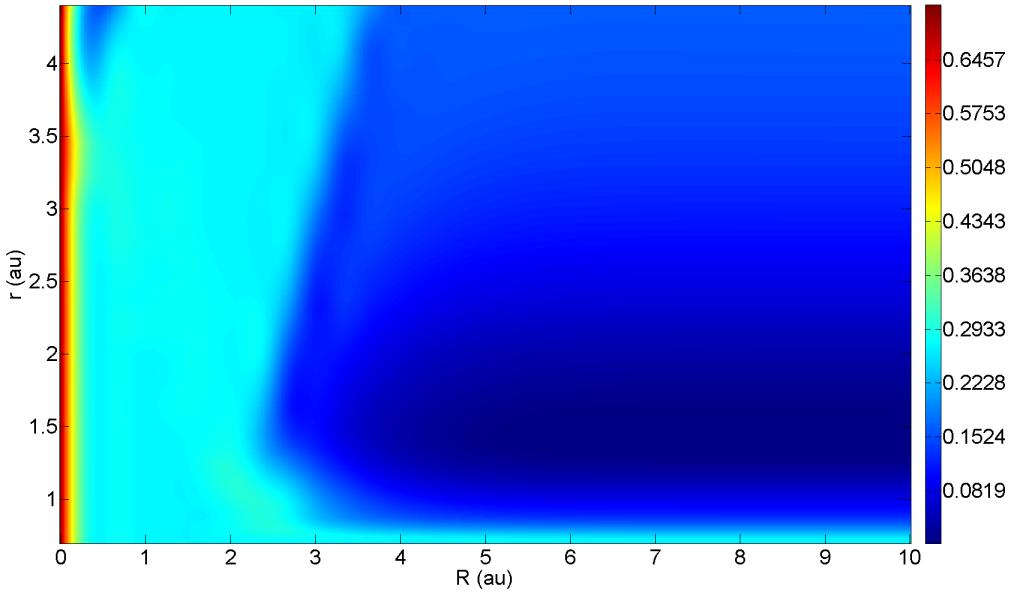

Figure 83. The 2D color rendering of the 20th adiabatic effective PES

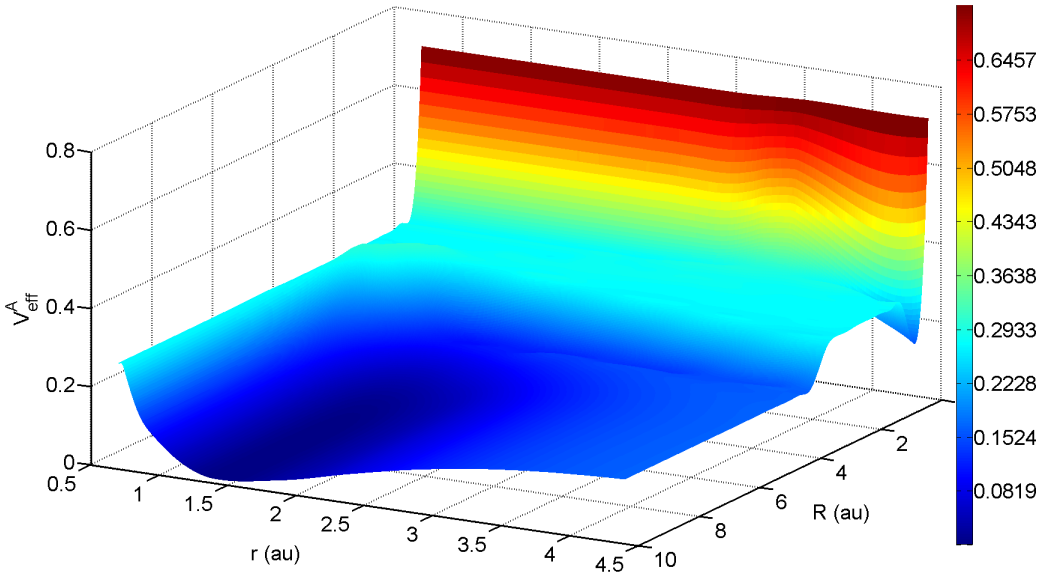

Figure 84. The 3D rendering of the 20th adiabatic effective PES

Bibliography

1. E. Schrödinger, Annalen der Physik **385** (13), 437-490 (1926).

2. M. Born and K. Huang, *Dynamical Theory of Crystal Lattices*. (Oxford University Press, 1954).

3. M. Born and J. R. Oppenheimer, Ann. Phys. (Leipzig) **84**, 457 (1927).

4. G. J. Halasz, A. Vibok, S. Suhai and M. Baer, The Journal of Chemical Physics **127** (24), 244101-244108 (2007).

5. D. R. Yarkony, in *Conical Intersections: Electronic Structure, Dynamics, & Spectroscopy*, edited by W. Domcke, D. R. Yarkony and H. Koppel (World Scientific, Singapore, 2004), Vol. 15, pp. 41-127.

6. W. Domcke, D. R. Yarkony and H. Koppel, in *Advanced Series in Physical Chemistry* (World Scientific, 2004).

7. D. R. Yarkony, J. Phys. Chem. A **105** (26), 6277-6293 (2001).

8. G. T. Phillips and G. P. Perram, Journal of Quantitative Spectroscopy and Radiative Transfer **109** (10), 1875-1885 (2008).

9. R. S. Pope, P. J. Wolf and G. P. Perram, Journal of Quantitative Spectroscopy and Radiative Transfer **64** (4), 363-377 (2000).

10. R. S. Pope, P. J. Wolf and G. P. Perram, Journal of Molecular Spectroscopy **223** (2), 205-213 (2004).

11. M. E. Fajardo, S. Tam, T. L. Thompson and M. E. Cordonnier, Chemical Physics **189** (2), 351-365 (1994).

12. E. Deumens, A. Diz, R. Longo and Y. Öhrn, Reviews of Modern Physics **66** (3), 917 (1994).

13. X.-G. Hu, T.-S. Ho, H. Rabitz and A. Askar, Physical Review E **61** (5), 5967 (2000).

14. T. Iordanov and S. Hammes-Schiffer, The Journal of Chemical Physics **118** (21), 9489-9496 (2003).

15. C. L. Lopreore and R. E. Wyatt, The Journal of Chemical Physics **116** (4), 1228-1238 (2002).

16. A. Soudackov, E. Hatcher and S. Hammes-Schiffer, The Journal of Chemical Physics **122** (1), 014505 (2005).

17. C. Swalina, M. V. Pak and S. Hammes-Schiffer, The Journal of Chemical Physics **123** (1), 014303 (2005).

18. R. E. Wyatt, C. L. Lopreore and G. Parlant, The Journal of Chemical Physics **114** (12), 5113-5116 (2001).

19. M. Barbatti, M. Ruckenbauer and H. Lischka, The Journal of Chemical Physics **122** (17), 174307 (2005).

20. A. Donoso, D. Kohen and C. C. Martens, The Journal of Chemical Physics **112** (17), 7345-7354 (2000).

21. J.-Y. Fang and S. Hammes-Schiffer, The Journal of Chemical Physics **107** (21), 8933-8939 (1997).

22. M. F. Herman and M. P. Moody, The Journal of Chemical Physics **122** (9), 094104 (2005).

23. A. W. Jasper and D. G. Truhlar, The Journal of Chemical Physics **122** (4), 044101 (2005).

24. A. Kondorskiy and H. Nakamura, The Journal of Chemical Physics **120** (19), 8937-8954 (2004).

25. C. Zhu, H. Kamisaka and H. Nakamura, The Journal of Chemical Physics **116** (8), 3234-3247 (2002).

26. M. H. Alexander, The Journal of Chemical Physics **99** (8), 6014-6026 (1993).

27. M. H. Alexander and M. Yang, The Journal of Chemical Physics **103** (18), 7956-7965 (1995).

28. P. J. Dagdigian and X. Yang, Faraday Discussions **108**, 287-307 (1997).

29. M. S. Gordon, V.-A. Glezakou and D. R. Yarkony, The Journal of Chemical Physics **108** (14), 5657-5659 (1998).

30. S. Matsika and D. R. Yarkony, J. Phys. Chem. A **106** (11), 2580-2591 (2002).

31. T. J. Tague and L. Andrews, J. Am. Chem. Soc. **116** (11), 4970-4976 (1994).

32. X. Yang and P. J. Dagdigian, Chemical Physics Letters **200** (3), 217-223 (1992).

33. X. Yang and P. J. Dagdigian, J. Phys. Chem. **97** (17), 4270-4276 (1993).

34. X. Yang, E. Hwang, M. H. Alexander and P. J. Dagdigian, The Journal of Chemical Physics **103** (18), 7966-7974 (1995).

35. X. Yang, E. Hwang and P. J. Dagdigian, The Journal of Chemical Physics **104** (20), 8165-8168 (1996).

36. T. A. Niday and D. E. Weeks, Chemical Physics Letters **308** (1-2), 106-114 (1999).

37. D. E. Weeks, T. A. Niday and S. H. Yang, The Journal of Chemical Physics **125** (16), 164301 (2006).

38. M. H. Alexander, S. Gregurick and P. J. Dagdigian, The Journal of Chemical Physics **101** (4), 2887-2902 (1994).

39. W. H. Breckenridge and H. Umemoto, Adv. Chem. Phys. **50** (1982).

40. R. S. Calfas and D. E. Weeks, Chemical Physics Letters **263** (1-2), 292-296 (1996).

41. M. J. MacLachlan and D. E. Weeks, J. Phys. Chem. A **102** (47), 9489-9493 (1998).

42. D. J. Tannor and D. E. Weeks, The Journal of Chemical Physics **98** (5), 3884-3893 (1993).

43. D. E. Weeks and D. J. Tannor, Chemical Physics Letters **207** (4-6), 301-308 (1993).

44. D. E. Weeks and D. J. Tannor, Chemical Physics Letters **224** (5-6), 451-458 (1994).

45. G. Chaban, M. S. Gordon and D. R. Yarkony, J. Phys. Chem. A **101** (43), 7953-7959 (1997).

46. D. R. Yarkony, in *Atomic, Molecular and Optical Physics Handbook*, edited by G. L. Drake (AIP, New York, 1996), pp. 357–377.

47. B. H. Lengsfield and D. R. Yarkony, in *Nonadiabatic Interactions Between Potential Energy Surfaces: Theory and Applications, in State-Selected and State to State Ion-Molecule Reaction Dynamics: Part 2 Theory*, edited by M. Baer and C.-Y. Ng (Wiley, New York, 1992), Vol. 82, pp. 1-71.

48. M. Baer, Physics Reports **358** (2), 75-142 (2002).

49. W. Lichten, Physical Review **131** (1), 229 (1963).

50. F. T. Smith, Physical Review **179** (1), 111 (1969).

51. A. Szabo and N. S. Ostlund, *Modern Quantum Chemistry: introduction to advanced electronic structure theory*. (Dover Publications Inc., 1996).

52. in *The American Heritage Dictionary of the English Language, Fourth Edition* (Houghton Mifflin Company, 2004).

53. T. Pacher, L. Cederbaum and H. Koppel, in *Advances in Chemical Physics*, edited by I. Prigogine and S. A. Rice (John WIley & Sons, Inc., New York, 1993), Vol. LXXXIV, pp. 293-391.

54. M. Baer and R. Englman, Chemical Physics Letters **335** (1-2), 85-88 (2001).

55. C. A. Mead and D. G. Truhlar, The Journal of Chemical Physics **77** (12), 6090-6098 (1982).

56. T. Pacher, C. A. Mead, L. S. Cederbaum and H. Koppel, The Journal of Chemical Physics **91** (11), 7057-7062 (1989).

57. H. Köppel, in *Conical Intersections: Electronic Structure, Dynamics, & Spectroscopy*, edited by W. Domcke, D. R. Yarkony and H. Koppel (World Scientific, Singapore, 2004), Vol. 15, pp. 175-204.

58. L. Cederbaum, in *Conical Intersections: Electronic Structure, Dynamics, & Spectroscopy*, edited by W. Domcke, D. R. Yarkony and H. Koppel (World Scientific, Singapore, 2004), Vol. 15, pp. 3-40.

59. A. J. Dobbyn and P. J. Knowles, Molecular Physics **91** (6), 1107 - 1124 (1997).

60. K. Ruedenberg and G. J. Atchity, The Journal of Chemical Physics **99** (5), 3799-3803 (1993).

61. A. Troisi and G. Orlandi, The Journal of Chemical Physics **118** (12), 5356-5363 (2003).

62. D. G. Truhlar, Journal of Computational Chemistry **28** (1), 73-86 (2007).

63. H. Nakamura and D. G. Truhlar, The Journal of Chemical Physics **115** (22), 10353-10372 (2001).

64. M. Baer, Chemical Physics Letters **35** (1), 112-118 (1975).

65. M. Baer, Mol. Phys. **40** (1980).

66. Z. H. Top and M. Baer, The Journal of Chemical Physics **66** (3), 1363-1371 (1977).

67. M. Baer, Chemical Physics Letters **349** (1-2), 84-88 (2001).

68. J. D. Jackson, *Classical Electrodynamics*, Third ed. (Wiley, 1998).

69. C. R. Evenhuis, X. Lin, D. H. Zhang, D. Yarkony and M. A. Collins, The Journal of Chemical Physics **123** (13), 134110-134112 (2005).

70. N. Matsunaga and D. R. Yarkony, Molecular Physics **93** (1), 79 - 84 (1998).

71. B. K. Kendrick, C. Alden Mead and D. G. Truhlar, Chemical Physics **277** (1), 31-41 (2002).

72. G. J. Halász, Á. Vibók and M. Baer, Chemical Physics Letters **413** (1-3), 226-230 (2005).

73. D. R. Yarkony, The Journal of Chemical Physics **105** (23), 10456-10461 (1996).

74. A. M. Mebel, A. Yahalom, R. Englman and M. Baer, The Journal of Chemical Physics **115** (8), 3673-3689 (2001).

75. D. R. Yarkony, J. Phys. Chem. A **102** (42), 8073-8077 (1998).

76. D. R. Yarkony, The Journal of Chemical Physics **110** (2), 701-705 (1999).

77. Z. Xu, M. Baer and A. J. C. Varandas, The Journal of Chemical Physics **112** (6), 2746-2751 (2000).

78. R. G. Sadygov and D. R. Yarkony, The Journal of Chemical Physics **109** (1), 20-25 (1998).

79. M.-L. Dubernet and J. M. Hutson, The Journal of Chemical Physics **101** (3), 1939-1958 (1994).

80. F. Rebentrost and W. A. L. Jr., The Journal of Chemical Physics **67** (7), 3367-3375 (1977).

81. C. Jouvet and J. A. Beswick, The Journal of Chemical Physics **86** (10), 5500-5508 (1987).

82. W. G. Harter, *Principles of Symmetry, Dynamics, and Spectroscopy*. (Wiley, New York, 1993).

83. R. N. Zare, *Angular Momentum: Understanding the Spatial Aspects in Chemistry and Physics*. (Wiley, New York, 1988).

84. F. Matzkies and U. Manthe, The Journal of Chemical Physics **112** (1), 130-136 (2000).

85. A. J. H. M. Meijer and E. M. Goldfield, The Journal of Chemical Physics **110** (2), 870-880 (1999).

86. R. T. Pack, The Journal of Chemical Physics **66** (4), 1557-1561 (1977).

87. G. A. Parker and R. T. Pack, The Journal of Chemical Physics **66** (7), 2850-2853 (1977).

88. S. M. Tarr, H. Rabitz, D. E. Fitz and R. A. Marcus, The Journal of Chemical Physics **66** (7), 2854-2859 (1977).

89. D. H. Zhang, M. Yang and S. Y. Lee, The Journal of Chemical Physics **117** (22), 10067-10072 (2002).

90. C. G. Gray, Canadian Journal of Physics **54** (1976).

91. T. A. Niday, Master's Thesis, Air Force Institute of Technology, 1999.

92. C. Leforestier, R. H. Bisseling, C. Cerjan, M. D. Feit, R. Friesner, A. Guldberg, A. Hammerich, G. Jolicard, W. Karrlein, H. D. Meyer, N. Lipkin, O. Roncero and R. Kosloff, Journal of Computational Physics **94** (1), 59-80 (1991).

93. J. Alvarellos and H. Metiu, The Journal of Chemical Physics **88** (8), 4957-4966 (1988).

94. J. R. Taylor, *Scattering Theory: the quantum theory of nonrelativistic collisions*. (Dover Publications Inc., 2006).

95. F. B. Duijneveldt, IBM Technical Research Report No RJ945 (1971).

96. J. T. H. Dunning, The Journal of Chemical Physics **90** (2), 1007-1023 (1989).

97. J. Senekowitsch, H.-J. Werner, P. Rosmus, E.-A. Reinsch and S. V. Oneil, The Journal of Chemical Physics **83** (9), 4661-4667 (1985).

98. L. Belcher, Master's Thesis, Air Force Institute of Technology, 2005.

99. D. M. Brink and G. R. Satchler, *Angular Momentum*. (Clarendon Press, Oxford, 1962).

100. M. H. Alexander, D. E. Manolopoulos, H. J. Werner and B. Follmeg, (1987), pp. a package of programs for the time independent quantum treatment of inelastic collisions and photodissociation.

101. P. Siegbahn and B. Liu, The Journal of Chemical Physics **68**, 1794 (1978).

102. D. G. Truhlar and C. J. Horowitz, The Journal of Chemical Physics **68**, 2466 (1978).

103. M. S. Child, *Atom-Molecule Collision Theory: A Guide for the Experimentalist*. (Plenum, New York, 1979).

104. M. S. Child, *Molecular Collision Theory*. (Dover, Mineola, NY, 1996).

105. E. Merzbacher, *Quantum Mechanics*, Third ed. (John Wiley and Sons, Inc., New York, 1998).

106. C. Cohen-Tannoudji, B. Diu and F. Laloe, *Quantum Mechanics*. (John Wiley and Sons, 1977).

Vita

Captain Matthew B. Garvin graduated from Brighton High School in Salt Lake City, Utah. After spending two years in the Amazon River Basin as a missionary he enrolled in the undergraduate physics program at Brigham Young University (BYU) in Provo, Utah. He graduated with a Bachelor of Science degree with University Honors in Physics in December 1999. He stayed at BYU for a Master of Science in Physics which was awarded in December 2001. In August 2003 he was awarded a Master of Science in Astronomy from the University of Virginia in Charlottesville, VA. He was commissioned through the Officer Training School in Maxwell, Alabama in August 2003.

His first assignment was at Kirtland AFB working as an optical imaging physicist in the Optics Division of the Directed Energy Directorate of Air Force Research Laboratory. In September 2005 he entered the Applied Physics program of the Department of Engineering Physics, Graduate School of Engineering and Management, Air Force Institute of Technology. Upon graduation he will serve at the Space Weather Center of Excellence, Space Vehicles Directorate, Air Force Research Laboratory located at Hanscom AFB.

REPORT DOCUMENTATION PAGE

Form Approved
OMB No. 074-0188

1. REPORT DATE *(DD-MM-YYYY)*	**2. REPORT TYPE**	**3. DATES COVERED** *(From – To)*
March 2009	Doctoral Dissertation	Sep 2006 – Jan 2009

4. TITLE AND SUBTITLE

The Effective Potential Energy Surfaces of the Nonadiabatic Collision $B\left(^2P_{j_a}\right) + H_2\left(^1\Sigma_g^+, v, j\right) \leftrightarrow B\left(^2P_{j_a'}\right) + H_2\left(^1\Sigma_g^+, v', j'\right)$

5a. CONTRACT NUMBER

5b. GRANT NUMBER

5c. PROGRAM ELEMENT NUMBER

6. AUTHOR(S)

Garvin, Matthew, B, Capt, USAF

5d. PROJECT NUMBER

5e. TASK NUMBER

5f. WORK UNIT NUMBER

7. PERFORMING ORGANIZATION NAMES(S) AND ADDRESS(S)

Air Force Institute of Technology
Graduate School of Engineering and Management (AFIT/EN)
2950 Hobson Way
WPAFB OH 45433-7765

8. PERFORMING ORGANIZATION REPORT NUMBER

AFIT/DS/ENP/09-J01

9. SPONSORING/MONITORING AGENCY NAME(S) AND ADDRESS(ES)

AFSOR (AFMC)
ATTN: Dr. Michael R. Berman
875 North Randolph Street, Suite 325, Room 3112
Arlington, Va., 22203-1768 DSN: 426-7781

10. SPONSOR/MONITOR'S ACRONYM(S)

11. SPONSOR/MONITOR'S REPORT NUMBER(S)

12. DISTRIBUTION/AVAILABILITY STATEMENT

APPROVED FOR PUBLIC RELEASE; DISTRIBUTION IS UNLIMITED

13. SUPPLEMENTARY NOTES

14. ABSTRACT

Effective potential energy surfaces (PESs) are calculated for the nonadiabatic collision $\left(^2P_{j_a}\right) + H_2\left(^1\Sigma_g^+, v, j\right) \leftrightarrow B\left(^2P_{j_a'}\right) + H_2\left(^1\Sigma_g^+, v', j'\right)$. This calculation employed 1 $^2A'$, 2 $^2A'$, and 1 $^2A''$ adiabatic PESs numerically calculated at the state-averaged multiconfigurational self-consistent field (SA-MCSCF)/configuration interaction (CI) level for several values of the H_2 bond length, H_2 orientation angle, and boron distance. The associated nonadiabatic coupling terms (NACTs) were calculated from the SA-MCSCF/CI wave functions using analytic gradient techniques. A line integral through the NACTs was then used to determine the adiabatic-to-diabatic mixing angle required to transform from the 1 $^2A'$ and 2 $^2A'$ adiabatic basis to a corresponding diabatic basis. When all nonadiabatic coupling terms between all electronic states are considered, the line integral is path independent. However, only NACTs between the 1 $^2A'$ and 2 $^2A'$ states were considered in these calculations, and the line integral was therefore path dependent. The path dependence of the line integral was used to characterize the error introduced by employing a truncated set of adiabatic states. A method for reducing the effect of this error through the use of symmetry derived boundary conditions was developed. The resulting diabatic PESs were combined with the total B + H_2 rotational kinetic energy and boron spin-orbit coupling to yield diabatic effective PESs. The diabatic effective PESs were diagonalized to yield adiabatic effective PESs.

15. SUBJECT TERMS

Potential energy surfaces for collisions (atoms and molecules); Surface crossings, nonadiabatic couplings (atoms and molecules); State-to-state scattering analyses (atoms and molecules); Electronic excitation and ionization of atoms including beam–foil excitation and ionization; Electron correlation calculations for atoms and molecules; Quantum chemistry; Nonadiabatic chemistry.

16. SECURITY CLASSIFICATION OF:			**17. LIMITATION OF ABSTRACT**	**18. NUMBER OF PAGES**	**19a. NAME OF RESPONSIBLE PERSON**
REPORT	**ABSTRACT**	**c. THIS PAGE**			Dr. David E. Weeks (ENP)
U	U	U	UU	176	**19b. TELEPHONE NUMBER** *(Include area code)* (937) 255-3636, ext. 4561 david.weeks@afit.edu

Standard Form 298 (Rev: 8-98)
Prescribed by ANSI Std. Z39-18